UC Riverside

UC Riverside Electronic Theses and Dissertations

Title

Electrical Transport and Thermal Expansion in van der Waals Materials: Graphene and Topological Insulator

Permalink

https://escholarship.org/uc/item/7qc2w9cw

Author

Jing, Lei

Publication Date

2013

Peer reviewed|Thesis/dissertation

eScholarship.org Powered by the California Digital Library
University of California

UNIVERSITY OF CALIFORNIA
RIVERSIDE

Electrical Transport and Thermal Expansion in van der Waals Materials: Graphene and Topological Insulator

A Dissertation submitted in partial satisfaction
of the requirements for the degree of

Doctor of Philosophy

in

Physics

by

Lei Jing

June 2013

Dissertation Committee:

Dr. Chun Ning (Jeanie) Lau, Chairperson
Dr. Shan-Wen Tsai
Dr. Jing Shi

Copyright by
Lei Jing
2013

The Dissertation of Lei Jing is approved:

Committee Chairperson

University of California, Riverside

ACKNOWLEDGEMENT

Foremost, I would like to express my most sincere gratitude to my advisor Professor Chun Ning (Jeanie) Lau for her continuous guidance and support throughout my PhD training. Jeanie is always a remarkable role model for me as a great scientist and mentor who fully dedicates to science. It is my greatest honor to be her student for the past five years and ever. I heartily appreciate her supervision to build my research interest and intuition. Her beautiful mind and knowledgeable physics insights inspired me to defeat those unexpected difficulties during the graduate school.

I also would like to sincerely thank the rest of my committee members: Prof. Jing Shi, Prof. Shan-Wen Tsai, Prof. Chris Dames and Prof. Marc Bockrath. I deeply appreciate them for the valuable discussions and advice about my research and my career development.

I acknowledge all the members from Lau's group: Dr. Feng Miao, Dr. Gang Liu, Dr. Jairo Velasco Jr., Dr. Wenzhong Bao, Dr. Hang Zhang, Zeng Zhao, Fenglin Wang, Yongjin Lee, Jhao-Wun Huang, Kevin Myhro, Yanmeng Shi, Nathaniel Gillgren, Petr Stepanov, Philip Kratz, Daivd Tran and Hoon Cho. We together built and maintained an active, friendly, supportive and productive group and all of us are devoted to make our group stand out in the graphene field.

Special thanks go to Dr. Jairo Velasco Jr. and Dr. Wenzhong Bao. Both of them led me to the road of nanofabrication and I am very grateful to have them as my senior colleagues and close friends. Jairo taught me the details of device fabrication and transport measurement techniques. It is a really treasured memory that he offered me great help on bilayer *pnp* project and we took shifts for device fabrication and measurement to keep our cryostats providing nice data 24/7. Wenzhong taught me his unique 'blade method' for graphene exfoliation, shadow mask fabrication and *in situ* thermal expansion imaging. In addition, Wenzhong used to drive me to Caltech to use their sophisticated SEM imaging every week until our campus equipped one. The memory is still fresh that we saw golden stars everywhere due to our blurred eyes when we got out from the Caltech facility after staring at computer screen for 8 hours straight. It is such a valuable experience for me to work together with them both. My graduate career would have been very different without their generous and unforgettable help.

I also would like to acknowledge Philip Kratz, Yongjin Lee and Fenglin Wang. Philip provided me nice graphene flakes for bilayer *pnp* project, Yongjin and I worked together on one-step dual-gated device and Fenglin spent a lot of time to help me for exfoliating suspended graphene and fabricating shadow masks. I cherish our friendship and the time in UCR 'orange' (clean) room together.

My Ph.D research involved lots of fruitful collaborations. Here, I would like to acknowledge our collaborators' efforts: Zhiyong Wang and Dr. Peng Wei from Prof. Jing

Shi's group generously supplied the Topological Insulator materials for us to conduct the supercurrent measurement; Dr. Wanyoung Jang from Prof. Chris Dames's group built the hot stage for our *in situ* SEM imaging; Prof. Marc Bockrath helped a lot to understand our bilayer transport data; Prof. Nikolai Kalugin from New Mexico Institute of Mining and Technology guided me to fabricate graphene-detector devices and performed all the measurements; Prof. Dmitry Smirnov from the National High Magnetic Field Laboratory in Tallahassee assisted me to operate their high-field cryostat during our visit.

I also thank UC Riverside staff members from the CNSE cleanroom, NMR & Optical Facilities center and Advanced Microscopy center: Dong Yan, Dexter Humphrey, Mark Heiden, Dan Borchardt and Krassimir Bozhilov for keeping these public facilities running smoothly. I deeply acknowledge Dr. Bayu Thedjoisworo and David Cheung for offering me a wonderful summer internship at Lam Research, SIG group. This precious opportunity opened my eyes to Silicon Valley and strengthened my faith to set the development of advanced semiconductor processing technique as my career goal.

Thanks to my dear friends Tao Lin/Vivian Ouyang, Dezheng Sun, Dong Gui and others, they filled my spare time with joy and I treasure our friendship for my lifetime. I feel very fortunate to meet my wife Lijuan Ji at Riverside. I can not thank her more for giving me faithful encouragement, love and support and sharing my happiness and frustration. Also, I am immensely indebted to my mother and father for their endless love and care through my life.

To my loving wife and my parents

ABSTRACT OF THE DISSERTATION

Electrical Transport and Thermal Expansion in van der Waals Materials:
Graphene and Topological Insulators

by

Lei Jing

Doctor of Philosophy, Graduate Program in Physics
University of California, Riverside, June 2013
Dr. Chun Ning (Jeanie) Lau, Chairperson

Novel two-dimensional materials with weak interlayer van der Waals interaction are fantastic platforms to study novel physical phenomena. This thesis describes our investigation of two different van der Waals materials: graphene and bismuth selenide with calcium doping ($Ca_xBi_{2-x}Se_3$, x as the doping level), the latter in the topological insulator family. Firstly, we characterize the electrical transport behaviors of high-quality substrate-supported bilayer graphene devices with suspended metal gates. The device exhibits a transport gap induced by external electric field with an on/off ratio of 20,000, which could be explained by variable range hoping between localized states or disordered charge puddles. At large magnetic fields, the device displays quantum Hall plateaus at fractional values of conductance quantum, which arises from equilibration of edge states

between differentially doped regions. Secondly, we present our study on the electronic transport of $Ca_xBi_{2-x}Se_3$ thin films, which are three-dimensional topological insulators and coupled to superconducting leads. In these novel Josephson transistors, we observe different characteristic features by energy dispersion spectrum (EDS) and Raman spectroscopy, and strong suppression of the critical current I_c. Thirdly, we explore the thermal expansion of suspended graphene. By *in-situ* scanning electron microscope (SEM), we measure the thickness-dependence of graphene's negative thermal expansion coefficient (TEC), which appears to be non-monotonic. We propose that the non-monotonic thickness dependence arises from a competition between the intrinsic TEC and the friction between the substrate and the graphene. Lastly, in collaboration with Dr. Nikolai Kalugin from New Mexico Tech, we explore the graphene's application as a quantum Hall effect infrared photodetector. This graphene-based detector can be operated at higher temperature (liquid nitrogen) and wider frequency than the prior implementations of quantum Hall detectors.

Contents

List of Figures

List of Tables

Chapter I Introduction of van der Waals materials: Graphene and Topological Insulators

"There is plenty of room at the bottom."

- Richard P. Feynman[1]

At 1959's American Physical Society Annual Meeting, Nobel Laureate Dr. Feynman gave a wonderful speech on the future of solid state physics. He forecasted the booming of micro- and nano-scale science and its tremendous impact on our life and society. Indeed, numerous new knowledge and technologies to manipulate and fabricate atomic-scale objects have been invented since the 1960s, leading to the exciting rise of micro- and nano-technology, for example the realization of very-large-scale integration technology (VLSI), and eventually the bloom of the entire semiconductor industry.

Thin-film technology is an important branch of nanotechnology, which includes material growth, characterization and simulation. For example, thin film materials are widely applied in semiconductor field effect transistor to confine charge carries into 2D planes. With the increasing interest in ultra-thin films, a truly two dimensional material - single layer carbon atoms arranged in honeycomb lattice, called 'graphene' – was firstly isolated from bulk graphite in a physics laboratory at University of Manchester[2]. The idea behind this genius experiment is breaking the van der Waals interaction between interlayer mechanically, thus enabling peeling off of single atom layers. Graphene soon attracted great attention throughout the world[2]: research papers are published or appear

online everyday and thousands of scientists from different disciplines investigate topics ranging from large-area film chemical synthesis[3,4,5,6], physics properties[7,8,9], engineering device construction[10-15] , to biological application[16,17].

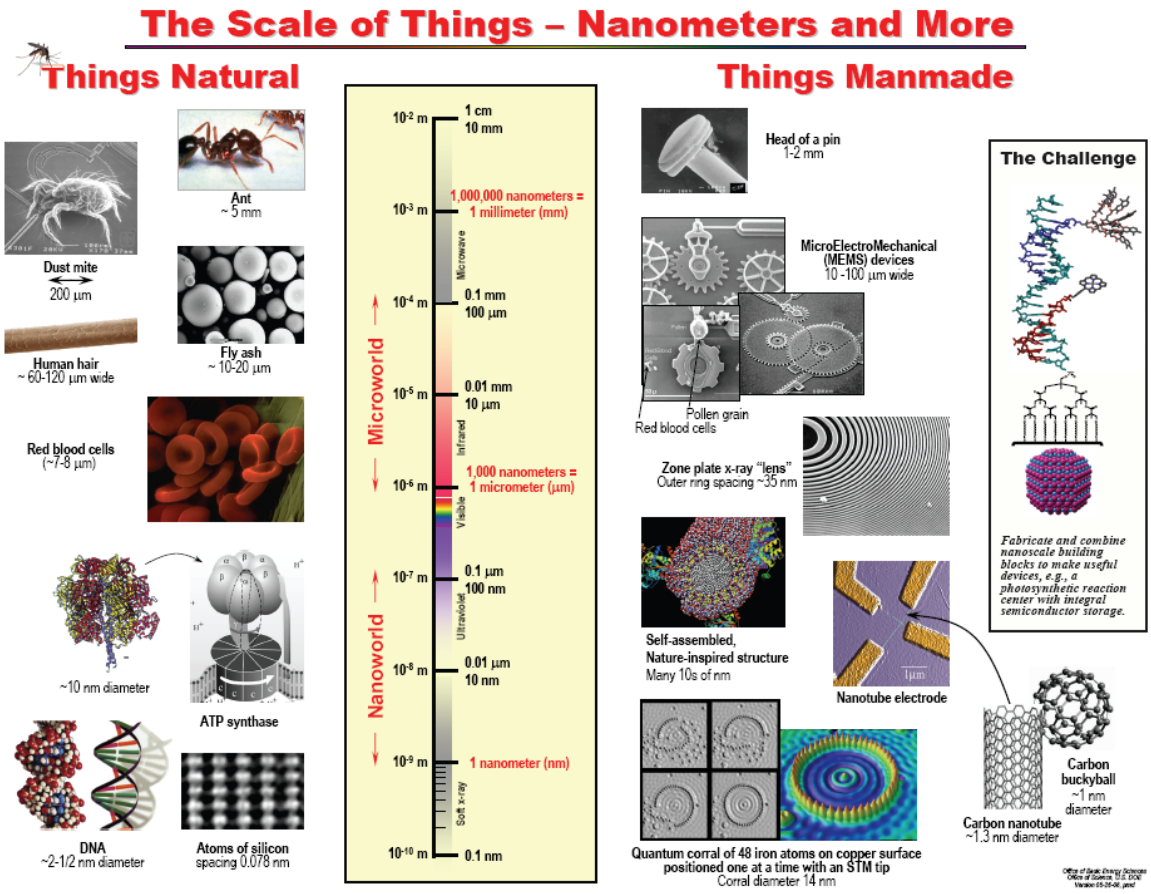

Fig. 1.1 Demonstration of the scales in Nanoscience and Nanotechnology. Copyright (2006), Office of Science, U.S. Department of Energy.

The rise of graphene led to a revival in the interest in the vast family of layered compounds and extraction or synthesis of single or few-layer atomic layers[4, 5,18]. These atomic layers are often called van der Waals materials[19]. One example is the three

dimensional topological insulators (3D TIs), such as Bi_2Se_3 and Bi_2Te_3[20]. 3D TIs are a type of bulk insulators while being conductive along their surfaces, the transport of which is protected by the time-reversal symmetry. Indeed, measurement by angle-resolved photoemission spectroscopy[45] (ARPES) confirmed that the band structure of bulk Bi_2Se_3 has a single Dirac cone, although its surface state hides in the bulk gap. Another appealing feature of 3D TIs is the possibility of realizing Majorana fermions[40, 41]. A theory[34] proposed by Fu and Kane describes that the surface of a topological insulator coupled with superconductor can support Majorana fermions, which would be important for the realization of quantum computation.

I-1. Two dimensional (2D) electron gas system: silicon and semiconductor heterostructure

Prior to graphene, researchers focused on two-dimensional electron gas (2DEG) to explore the 2D quantum phenomena. Generally, in a 2DEG or 2DHG (2D hole gas), charge carriers can move freely like gaseous atoms in the planar (*x*-*y*) dimensions, while their motions are restricted in the vertical direction by potential barriers or other confinement methods. Two classic systems have been studied extensively and applied for industry production: Si-MOSFETs (silicon metal-oxide-semiconductor field-effect transistors) and HEMTs (high-electron-mobility-transistors).

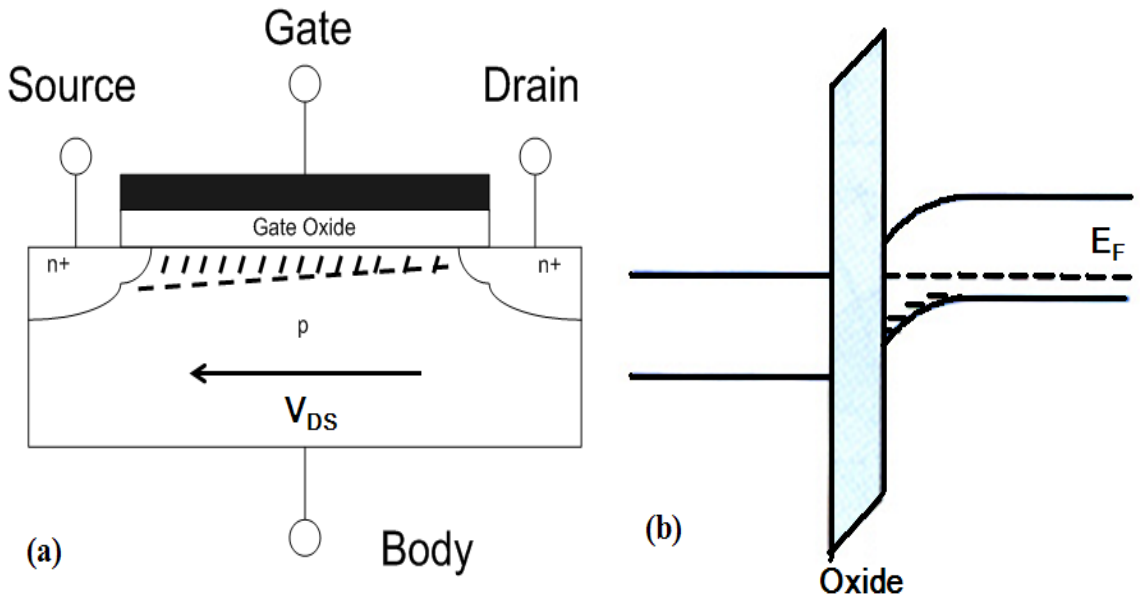

Fig. 1.2 Cross section of the n type Si-MOSFET and its triode-mode band diagram: (a) Cross section schematic diagram, where *n* and *p* denote electron and hole, respectively. (b) Band bending for triode-mode, conditions: $V_{GS} > V_{th}$ and $V_{DS} < (V_{GS} - V_{th})$, where V_{GS} is voltage difference between gate and source, V_{DS} is voltage difference between drain and source. E_F is the Fermi level in Silicon band structure.

Silicon (Si) is the fourteenth chemical element in the periodic table and it is the second most abundant element in the earth curst, which occupies 25.7% by weight[21]. It has been the most important semiconductor material in the electronics industry for more than half century, because of its advantages over other semiconductor materials: compatibility with mass production[22] (the Czochralski process), stable chemical and physical properties, existence of natural oxide (SiO_2), *etc*. Si-MOSFETs confine mobile electrons into a plane by applying external gate voltage V_g to induce an accumulation or inversion layer between the interface of gate oxide (ox) and the bulk, which is depicted as the shadow

regime in Fig. 1.2(a). Therefore, the average area charge density of this 2DEG can be written as

$$n_s = \frac{\epsilon_{ox}}{e d_{ox}} (V_g - V_{th}) \qquad (1)$$

, where e is one electron charge, ϵ_{ox} is dielectric constant of gate oxide, d_{ox} is the thickness of gate oxide and V_{th} is the threshold voltage for the device. 2D physics, such as quantum Hall effect, are first studied and observed on these devices.

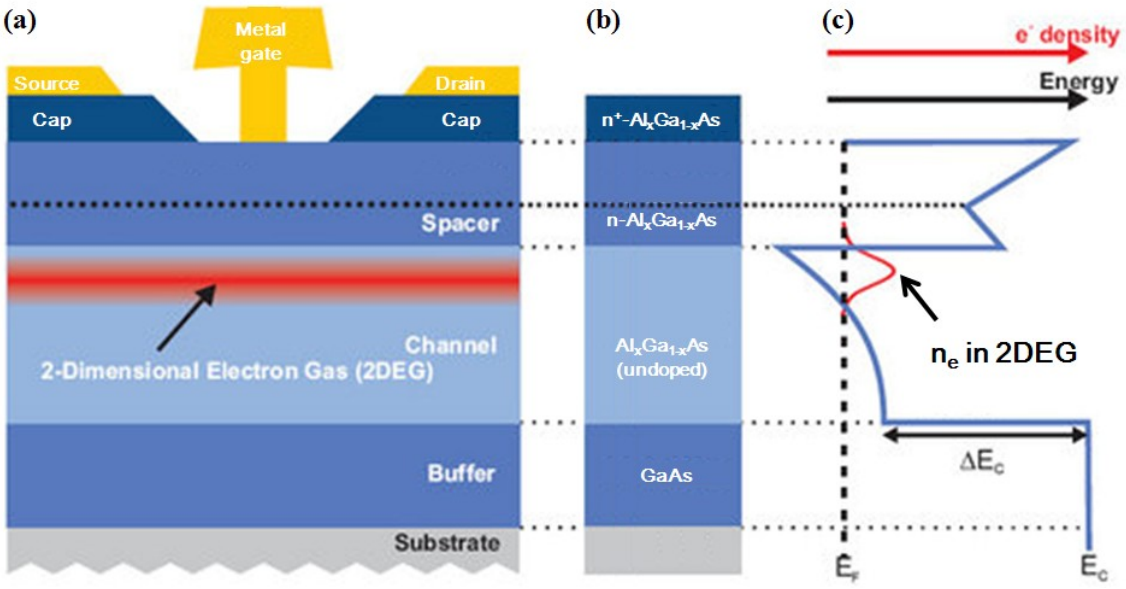

Fig. 1.3 Cross section of typical AlGaAs-GaAs HEMT illustrating its component structure and band diagram: (a) Cross section of $Al_xGa_{1-x}As$-GaAs HEMT schematic diagram; (b) Structural components in different layers; (c) Band structure of the interfaces between n-$Al_xGa_{1-x}As$ and intrinsic $Al_xGa_{1-x}As$ and GaAs, where e denotes electron, n_e is electron density, E_F is the Fermi level of HEMT structure, E_c is the edge of conduction band and ΔE_c is the gap between the conduction band edges from two different semiconductor materials.

The invention of HEMTs is largely based on the research and development of modern growth technologies for semiconductor heterostructure, such as molecular beam epitaxy (MBE). In this technology, one atomic layer can be deposited at a time, creating atomically sharp interfaces between different materials (heterostructures) with band gap mismatches, such as GaAs- $Ga_{1-x}Al_xAs$ (as shown in Fig. 1.3) or Si-$Si_{1-x}Ge_x$. The best samples have extremely high mobility, up to 30,000,000 $cm^2/(V \cdot s)$[24], which allows the observation of various quantum phenomena.

I-2. Dimensionality of carbon

Carbon is present in all known life forms and is one of the essential elements in the organic matter. In addition, there are 3 common 3D carbon materials: graphite, diamond and amorphous carbon.

Diamond is formed from atomic carbon at very high pressure, with all sp^3 bonds. Therefore, diamond is an insulator and it crystallizes into a tetrahedron structure (as shown in Fig. 1.4(a)). In contrast, graphite is a semi-metal, with much higher electrical conductivity than diamond. Fig. 1.4(b) presents the schematic drawn of crystalline graphite. It is a layered material, in which the carbon sheets are stacked into α- (Bernal) or β- (rhombohedral) order by weak van der Waals force. The stacking order of graphite can be altered under certain mechanical or thermal conditions[25]. Natural graphite is widely used as components of batteries, lubricants, *etc*. Since the isolation of graphene in

2004, graphite (highly oriented pyrolytic graphite (HOPG) and/or Kish graphite) has been one of the major source materials from which graphene is extracted. The amorphous carbon (as shown in Fig. 1.4(c)), unlike diamond and graphite, does not have any regular crystalline structure. It is the raw material for the ink industry, the rubber industry, *etc*.

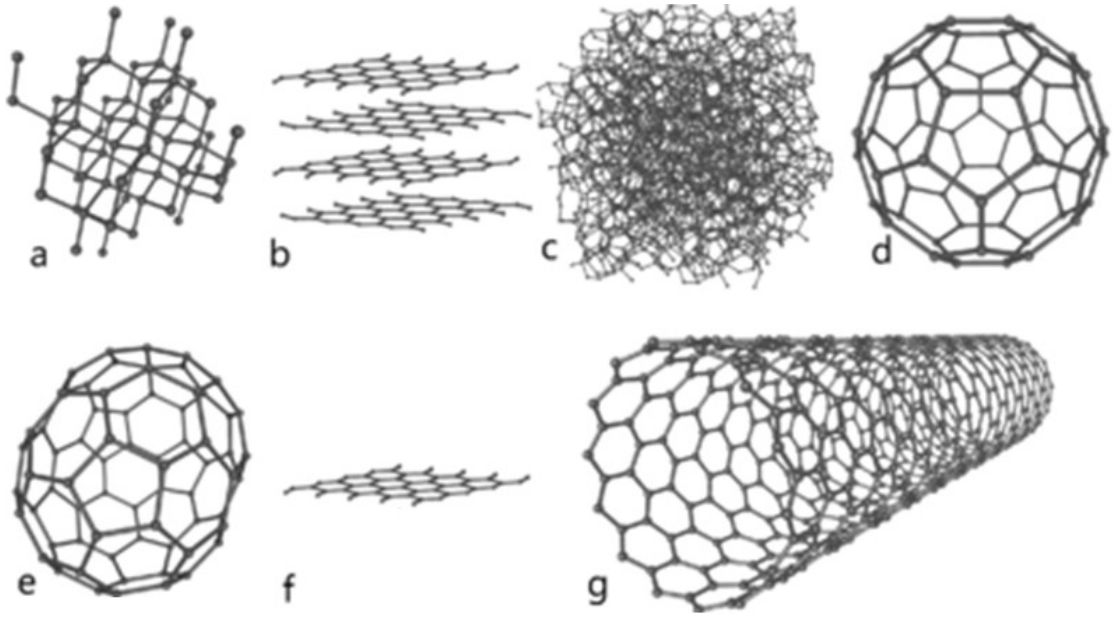

Fig. 1.4 Some allotropes of carbon: (a) Diamond; (b) Graphite; (c) Amorphous carbon; (d–e) Fullerenes (C_{60}, C_{70}); (f) Graphene; (g) Carbon nanotube. Adopted and modified from http://en.wikipedia.org/wiki/File:Eight_Allotropes_of_Carbon.png

The two-dimensional (2D) structure of carbon is graphene, which is an atomic sp^2-hybridized layer arranged in a honeycomb network. In Fig. 1.3(f), each atom forms 3 σ-bonds with its nearest neighbors. These in-plane covalent bonds are almost as strong as those sp^3 bonds in diamond, thus providing graphene with diamond-like robustness and thermal properties[20]. The extra valence electron of each carbon atom contributes to the

electrical conductivity and constitutes the half-filled π-bonds in the basal direction. These π-bonds are essential for describing the low-energy physics of graphene, typically calculated using the tight-binding model[26], which will be discussed in the following chapter.

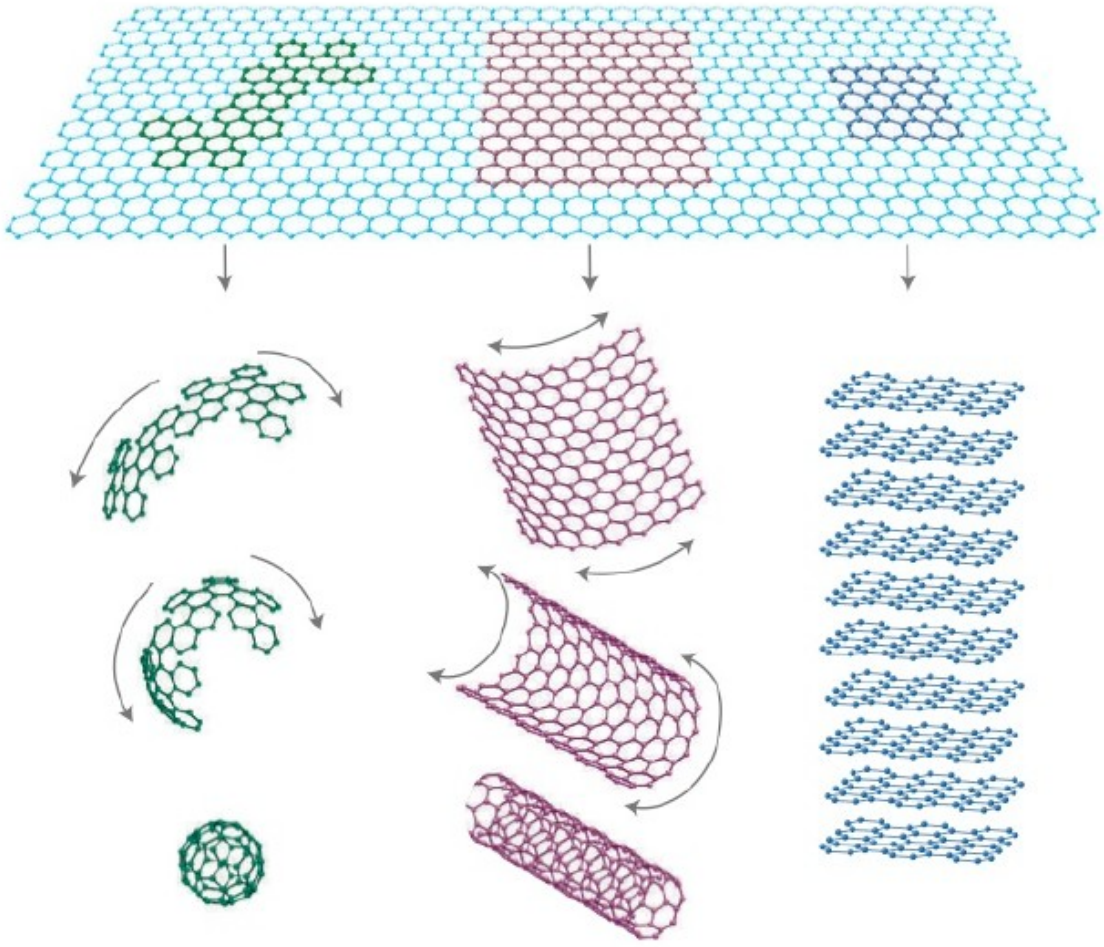

Fig. 1.5 Graphene allotropes in different dimensionalities. Reprint with permission from A. Geim and K. Novoselov, *Nature Materials* 6 (3), 183–191 (2007). Copyright (2007) Nature Publishing Group.

Zero-dimensional (0D) carbon molecule: fullerene and one-dimensional (1D) carbon nanotube (CNT) were brought to scientific community by Richard Smalley and his coworkers[27] at 1985 and Sunio Iijima[28] at 1991, respectively. Both of them have unexpected physical and chemical properties, making them popular topics of material science in the past two decades. In addition, they have great application potentials in nanotechnology, engineering, biosensor, *etc*. Fig. 1.5 demonstrates the origin-forming relationships between different dimensional carbon allotropes. Fullerene molecule can be formed from a piece of graphene sheet with appropriate shape; CNT can be rolled from a piece of graphene and many graphene layers stack together to form graphite. Therefore, graphite, carbon nanotube and fullerene are sometimes referred to as 'graphene allotropes'[29].

I-3. Topological Insulators

The discovery and understanding of new material is one of the major interests for materials scientists, including physicists, chemists and related researchers. Topological insulators (TIs) are a new class of materials that have a bulk band gap as the usual insulators, but their surfaces or edges host gapless electronic states due to the protection by particle number conservation and time reversal symmetry[30]. Surface conduction in TIs is characterized by chiral, spin-polarized counter-propagating states. Backscattering between these conductive channels is forbidden, resulting in topologically protected ballistic transport.

The dimensionality of TIs varies from the 2D semiconductor compound quantum well[31, 32] to the 3D films, like Bi_2Se_3 and Bi_2Te_3[33~35]. These systems are novel 2DEG platforms for the investigation of quantum spin Hall effect, which can be realized by the combination of strong spin-orbit coupling and the time-reversal symmetry[36,37]. In 2007, 2D HgTe quantum well[31, 32] devices provided the first demonstration of quantum spin Hall effect, which was theoretically predicted[38] two decades ago. A quantized conductance plateau $\sim 2e^2/h$ was observed without any external magnetic field, indicating the sign of quantum spin Hall and edge channels' ballistic transport. More convincingly, the quantized plateau disappeared when the time-reversal symmetry was broken by small magnetic field penetrating through the sample.

The first member in 3D TIs family, $Bi_{1-x}Sb_x$, was discovered with the topological surface states[46] by ARPES measurement in 2008. More candidates, such as Bi_2Se_3[45], Bi_2Te_3[47] and Sb_2Te_3, were found in succession. 3D TIs have the advantage that their synthesis method[42] is easier than that for 2D TI quantum well structure. However, the Fermi level in some of these materials is located in either the conduction or valence bands due to spontaneously generated defects. In order to observe the surface state within the bulk gap, extra doping[43] or gating is needed.

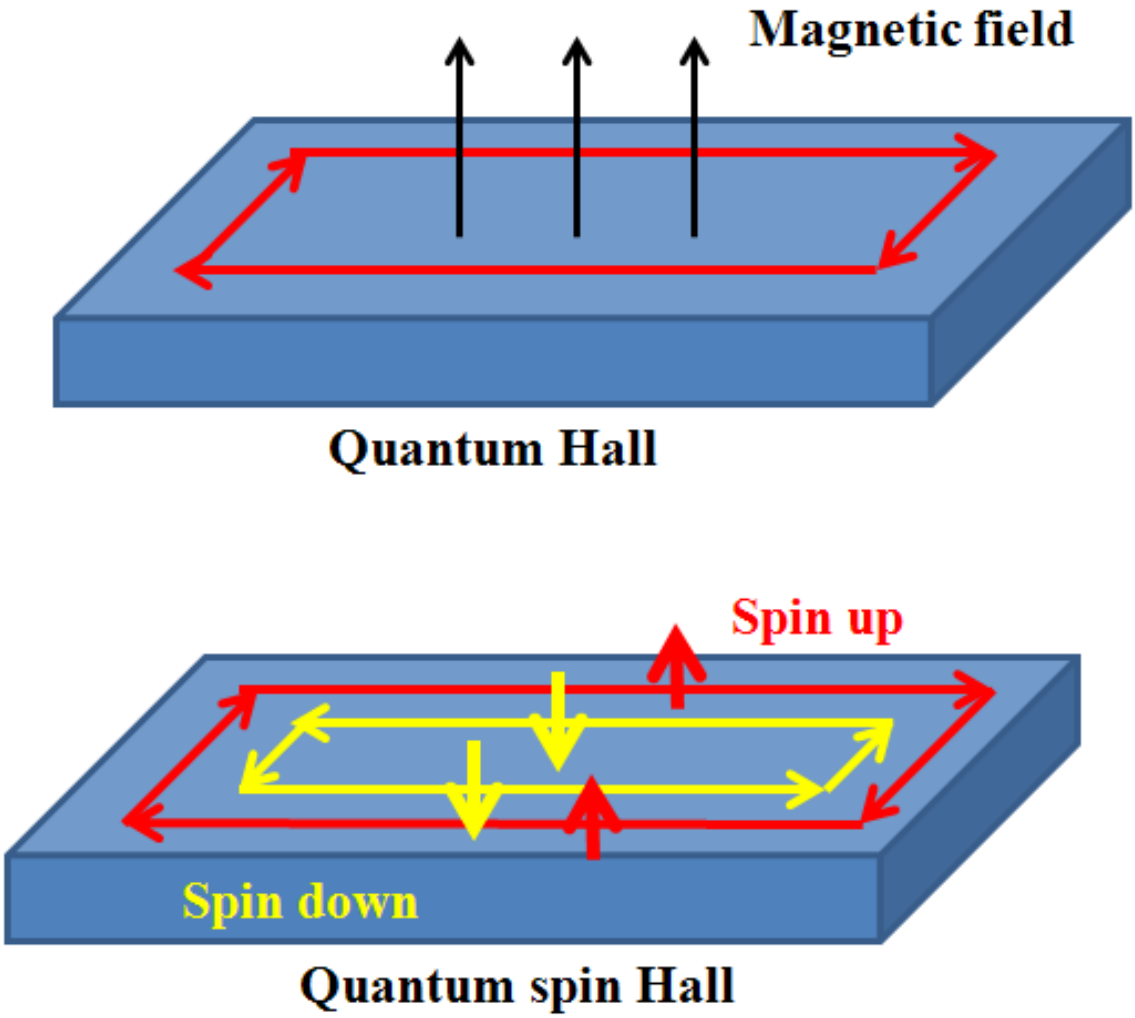

Fig. 1.6 Schematics illustrating the quantum Hall and quantum spin Hall effects: Upper image: quantum Hall effect in the presence of external magnetic field, with conducting channels of a single chirality; Lower image: quantum spin Hall requires no magnetic field, with counter-propagating edge states for spin-up and spin-down carriers' transport.

In addition, 3D TIs are fascinating platforms for realizing many phenomena that were previously predicted in theory, such as magnetic monopoles and magneto-electric effect[39].

Our data presented in Chapter V demonstrate the supercurrent in superconductor-TI-superconductor Josephson junctions.

I-4. Thesis outline

This thesis details my scientific adventure as a Ph.D student at Dr. Lau's group and it will proceed as following. Chapter II focuses on the theoretical models of graphene and presents the tight bonding calculation for single layer/bilayer graphene. These basic backgrounds are the starting point for understanding the experimental data in graphene. We also discuss quantum Hall effect and Raman spectroscopy, which are two important experimental methods to characterize single- and few-layer graphene. Chapter III describes the basic experimental procedures of nano-device fabrication, with an emphasis on high quality substrate-supported graphene device with suspended metal gate. Chapter IV presents electrical transport studies of bilayer graphene *pnp* devices[44]. We observe a transport gap in bilayer graphene induced by applied electrical field, and edge state equilibration in the bilayer graphene *p-n-p* junction. Chapter V concentrates on the electronic transport in topological insulator thin films coupled to superconducting leads. We characterize Bi_2Se_3 doped with calcium, and observe a weak suppression of the critical current I_c in these novel Josephson transistors. In chapter VI, we study the thermal expansion of suspended graphene between 300 K and 470 K as a function of film thickness, and find an unusual non-monotonic dependence on thickness. Such a curious behavior is not completely understood, but speculated to arise from a competition

between intrinsic thermal expansion and friction between graphene and the substrate, both of which are thickness dependent. Chapter VII presents our work on graphene-based QHE photodetector. In the end, chapter VIII provides a brief summary of this thesis and the outlook for future work.

Conclusions

In this chapter, we briefly reviewed the history of 2DEG system, graphene and TIs. These novel materials enabled us to observe a number of many-body physics phenomena. From an application standpoint, graphene and TIs are promising candidates for next generation semiconductor technology, because these novel low-dimensional platforms meet the need for smaller and faster devices as possible replacements for silicon for the semiconductor industry.

References:

1) R.P. Feynman, R.P, *Journal of Microelectromechanical Systems* **1**, 60–66 (1992) Reprint of the talk in 1959.

2) A.K. Geim, *Rev. Mod. Phys.* **83**, 851 (2011)

3) C. Berger, Z. Song, T. Li, X. Li, A. Y. Ogbazghi, R. Feng, Z. Dai, A. N. Marchenkov, E. H. Conrad, P. N. First, W. A. de Heer, *J. Phys. Chem. B* **108**, 19912 (2004)

4) X.S. Li, W.W. Cai, J.H. An, S. Kim, J. Nah, D.X. Yang, R. Piner, A. Velamakanni, I. Jung, E. Tutuc, S.K. Banerjee, L. Colombo, R. S. Ruoff, *Science* **324** (5932): 1312–1314 (2009)

5) S. Bae, H. Kim, Y. Lee, X. Xu, J. Park, Y. Zheng, J. Balakrishnan, T. Lei, H. Ri Kim, Y. Song, Y. Kim, K. Kim, B. Özyilmaz, J-H. Ahn, B.H. Hong, S. Iijima, Sumio. *Nature Nanotechnology* **5 (8)**, 574–8 (2010).

6) J. Coraux, C. Busse, and T. Michely, *Nano Letters* **8 (2)**, 565–570 (2008).

7) A. C. Ferrari, J. C. Meyer, V. Scardaci, C. Casiraghi, M. Lazzeri, F. Mauri, S. Piscanec, D. Jiang, K. S. Novoselov, S. Roth, A. K. Geim, *Phys. Rev. Lett.* **97**, 187401 (2006)

8) K. S. Novoselov, A. K. Geim, S. V. Morozov, D. Jiang, M. I. Katsnelson, I. V. Grigorieva, S. V. Dubonos and A. A. Firsov, *Nature* **438 (7065)**, 197-200 (2005).

9) Y. B. Zhang, Y. W. Tan, H. L. Stormer and P. Kim, *Nature* **438 (7065)**, 201-204 (2005).

10) G. Eda, M. Chhowalla, *Nano Letters* **9 (2)**, 814–818 (2009).

11) T. Ohta, A. Bostwick, T. Seyller, K. Horn, and E. Rotenberg, *Science* **313 (5789)**, 951 (2006).

12) Y. Zhang, T. Tang, C. Girit, Z. Hao, M. Martin, A. Zettl, M. Crommie, Y. Shen, and F. Wang, *Nature* **459 (7248)**, 820–823, (2009).

13) S. Kim, J. Nah, I. Jo, D. Shahrjerdi, L. Colombo, Z. Yao, E. Tutuc, and S. Banerjee, *Applied Physics Letters* **94**, 062107 (2009).

14) K. Bolotin, K. Sikes, Z. Jiang, M. Klima, G. Fudenberg, J. Hone, P. Kim, and H. Stormer, *Solid State Communications* **146 (9-10)**, 351–355 (2008)

15) G. Liu, J. Velasco, W. Z. Bao, C. N. Lau, *Applied Physics Letters* **92**, 203103 (2008)

16) M.S. Xu, D. Fujita, N. Hanagata, *Small* **5 (23)**, 2638–49 (2009)

17) S. He, B. Song, D. Li, C. Zhu, W. Qi, Y. Wen, L. Wang, S Song, H. Fang, C. Fan, *Advanced Functional Materials* **20 (3)**, 453 (2010).

18) K. S. Novoselov, D. Jiang, F. Schedin, T. J. Booth, V. V. Khotkevich, S. V. Morozov, A. K. Geim, *PNAS* **102**, 10451 (2005).

19) *Function Accelerated nanoMaterial Engineering* (FAME), research theme: http://www.src.org/program/starnet/fame/

20) D. Teweldebrhan, V. Goyal, and A. A. Balandin, *Nano Lett* **10** (4), 1209-1218 (2010)

21) Data from http://en.wikipedia.org/wiki/Abundance_of_elements_in_Earth's_crust

22) Jan Czochralski and his method, Oficyna Wydawnicza ATUT, Wrocław–Kcynia, (2003)

23) K. v. Klitzing, G. Dorda, and M. Pepper, *Physical Review Letters* **45**, 494–497 (1980)

24) A. Kumar, G. A. Csáthy, M. J. Manfra, L. N. Pfeiffer, and K. W. West, *Physical Review Letters* **105**, 246808 (2010)

25) IUPAC, Compendium of Chemical Terminology, 2nd edition. (1997)

26) A. H. Castro Neto, F. Guinea, N.M.R. Peres, K.S. Novoselov, A.K. Geim, *Rev. Mod. Phys.* **81**, 109 (2009)

27) H.W. Kroto, J.R. Heath, S.C. O'Brien, R.F. Curl, R.E. Smalley, *Nature* **318 (6042)**, 162–163 (1985)

28) Sumio Iijima, *Nature* **354 (6348)**, 56-58 (1991)

29) A. Geim and K. Novoselov, *Nature Materials* **6 (3)**, 183–191 (2007)

30) M.Z. Hasan and C.L. Kane, *Rev. Mod. Phys.* **82**, 3045 (2010)

31) B. A. Bernevig, T. L. Hughes, and S. C. Zhang, *Science* **314**, 1757-1761 (2006).

32) M. Konig, S. Wiedmann, C. Brune, A. Roth, H. Buhmann, L. W. Molenkamp, X.-L. Qi, and S.-C. Zhang, *Science* **318**, 766-770 (2007).

33) F. Wilczek, *Nature Physics* **5** (9), 614-618 (2009).

34) L. Fu and C. L. Kane, *Phys. Rev. Lett.* **100**, 096407 (2008)

35) James G. Analytis, Jiun-Haw Chu, Yulin Chen, Felipe Corredor, Ross D. McDonald, Z. X. Shen, and Ian R. Fisher, *Phys. Rev. B* **81**, 205407 (2010)

36) X. L. Qi and S. C. Zhang, *Physics Today* **63** (1), 33-38 (2010).

37) D. Hsieh, Y. Xia, D. Qian, L. Wray, J. H. Dil, F. Meier, J. Osterwalder, L. Patthey, J. G. Checkelsky, N. P. Ong, A. V. Fedorov, H. Lin, A. Bansil, D. Grauer, Y. S. Hor, R. J. Cava, M. Z. Hasan, *Nature* **460 (7259)**, 1101–1105 (2009).

38) O.A. Pankratov, S.V. Pakhomov, B.A. Volkov, *Solid State Communications* **61 (2)**, 93–96 (1986)

39) G. Zhang, H. Qin, J. Teng, J. Guo, Q. Guo, X. Dai, Z. Fang, K. Wu, *Appl. Phys. Lett.* **95**, 053114 (2009)

40) Y. Zhang, K. He, C. Chang, C. Song, L. Wang, X. Chen, J. Jia, Z. Fang, X. Dai, W. Shan, S. Shen, Q. Niu, X. Qi, S.C. Zhang, X. Ma and Q. Xue, *Nature Physics* **6** (8), 584-588 (2010)

41) Y. S. Hor, A. Richardella, P. Roushan, Y. Xia, J. G. Checkelsky, A. Yazdani, M. Z. Hasan, N. P. Ong, and R. J. Cava, *Phys. Rev. B* **79**, 195208 (2009)

42) S. Cho , N. P. Butch , J. Paglione, M. S. Fuhrer, *Nano Lett* **11** (5), 1925-1927 (2011)

43) Z. Wang, T. Lin, P. Wei, X. Liu, R. Dumas, K. Liu, J. Shi, *Applied Physics Letter* **97**, 042112 (2010)

44) L. Jing, J. Velasco Jr., P. Kratz, G. Liu, W. Bao, M. Bockrath, C. N. Lau, *Nano Lett.***10**, 4000 (2010)

45) Y. Xia, D. Qian, D. Hsieh, L. Wray, A. Pal, H Lin, A. Bansil, D. Grauer, TY. S. Hor, R. J. Cava, and M. Z. Hasan, *Nature Phys.* **5(6)**, 398-402 (2009)

46) D. Hsieh, D. Qian, L. Wray, Y. Xia, Y. S. Hor, R. J. Cava, M. Z. Hasan, *Nature* **452**, 970 (2008)

47) Y. L. Chen, J. G. Analytis, J.-H. Chu, Z. K. Liu, S.-K. Mo, X. L. Qi, H. J. Zhang, D. H. Lu, X. Dai, Z. Fang, S. C. Zhang, I. R. Fisher, Z. Hussain and Z.-X. Shen, *Science* **325**, 178(2009)

Chapter II. Theoretical background of Graphene

To date, single- and few-layer graphene constitute some of the most popular topics in condensed matter research[1, 2]. This chapter describes the basic background knowledge of these materials, including their lattice structures, energy band spectrum, Raman phonon-electron interaction and quantum Hall effect. The tight-binding model that includes only nearest-neighbor hopping is used for band structure calculation of single layer graphene and bilayer graphene. This approximation considers single-particle picture without electron-electron interaction, and is very useful for understanding graphene transport at low energy regime[1]. In addition, we discuss quantum Hall effect and Raman spectroscopy, which are two important experimental methods to characterize single- and few-layer graphene. Both of them can provide layer information of graphene sheets and provide insights into low-dimensional physics in these novel 2DEGs systems.

II-1. Monolayer graphene lattice structure and tight binding approximation

The hexagonal lattice structure of a single layer graphene in real space is presented in Fig. 2.1(a). The whole sheet is arranged in a sp^2 carbon honeycomb network. The nearest neighboring atoms A (in red) and B (in blue) are linked together by strong covalent bonds with the carbon-carbon lattice constant $a_{c-c} \approx 0.142$ nm. These covalent bonds are called σ-atomic bonds, and consist of hybridized sp_x and sp_y orbitals. The fourth valence

electron of each carbon atom contributes to form the π bonds via sp_z orbital. The unit cell of graphene consists of two adjacent carbon atoms, with the real space vectors

$$a_1 = \frac{a_{c-c}}{2}(3, \sqrt{3}) , \qquad a_2 = \frac{a_{c-c}}{2}(3, -\sqrt{3}) \qquad (1)$$

So the reciprocal-lattice in the momentum space (k-space) is calculated by

$$a_i \cdot b_j = 2\pi \, \delta_{ij}, \qquad i, j = 1,2 \qquad (2)$$

where δ_{ij} is the Kronecker delta symbol, δ_{ij} is 1 if $i = j$ and 0 if $i \neq j$. We obtain the reciprocal vectors b_1 and b_2:

$$b_1 = \frac{2\pi}{3a_{c-c}}(1, \sqrt{3}) , \qquad b_2 = \frac{2\pi}{3a_{c-c}}(1, -\sqrt{3}) \qquad (3)$$

as shown in Fig. 2.1(b) with purple pointers. In addition, Fig. 2.1(b) illustrates the first Brillouin zone (1st BZ, the shaded gray portion) of graphene in k-space and the information of all highly symmetric points Γ (BZ center), M (edge center), K (BZ corner) and K′ (BZ corner).

Two special points K and K′, called the Dirac points, are of particular interest for condensed matter physicists:

$$K = (\frac{2\pi}{3a_{c-c}}, \frac{2\pi}{3\sqrt{3}a_{c-c}}) , \qquad K' = (\frac{2\pi}{3a_{c-c}}, -\frac{2\pi}{3\sqrt{3}a_{c-c}}) \qquad (4)$$

Because the π bonds are largely responsible for the electronic properties of graphene, we consider their contributions and the nearest-neighbor hopping term in the tight binding approximation.

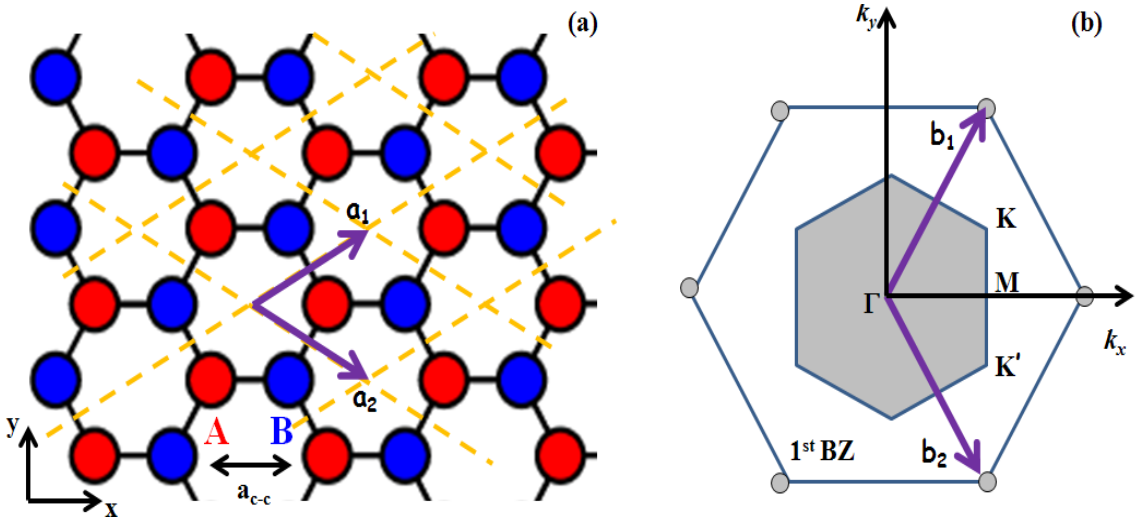

Fig. 2.1 Monolayer graphene network (a) and its reciprocal-lattice with Brillouin zone (b).

To calculate the charge energy dispersion relation of monolayer graphene, we need to establish the Hamiltonian. Based on the Wannier expression, it can be represented as

$$\hat{H} = \sum_{i,\sigma} \mu_i (a^*_{i,\sigma} a_{i,\sigma} + b^*_{i,\sigma} b_{i,\sigma}) - t_{i,j} \sum_{<i,j>,\sigma} a^*_{i,\sigma} b_{j,\sigma} \quad (5)$$

where i and j stand for nearest-neighbor carbon atoms, a and b denote sublattice A and B, $a_{i,\sigma}$ is the annihilation operator of A lattice with spin ($\sigma = \uparrow, \downarrow$), while $a^*_{i,\sigma}$ is their creation operator (a similar rule for $b^*_{i,\sigma}$ and $b_{i,\sigma}$), and μ_i is the on-site energy of each lattice, $t_{i,j}$ is the hopping energy between the nearest neighbors and its value $t_{i,j} = t \approx 3.0$ eV for graphene.

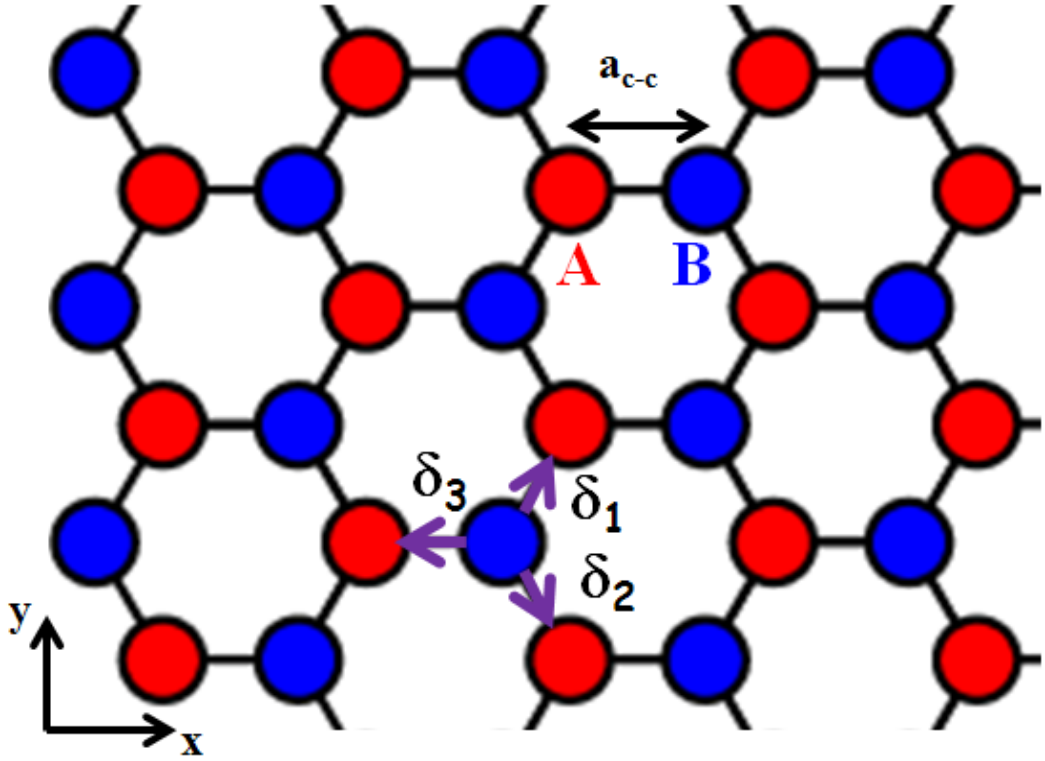

Fig. 2.2 Visualization of tight binding model with first-nearest neighbor hopping: the hopping between sublattices, δ_i, i=1,2,3 denote the nearest-neighbor vectors.

Next we will calculate the transfer integral matrix $H_{i,j}$ and overlap integral matrix $S_{i,j}$ based on the linear combination of Bloch function Φ_i

$$H_{i,j}(\vec{k}) = \langle \Phi_i | H | \Phi_j \rangle, \quad S_{i,j}(\vec{k}) = \langle \Phi_i | \Phi_j \rangle \qquad (i,j = 1,2,,,,n) \qquad (5)$$

$$\Phi_i(\vec{k},\vec{r}) = \frac{1}{\sqrt{N}} \sum_{j=1}^{N} e^{i\vec{k}\cdot R_{i,j}} \varphi_i(\vec{r} - R_{i,j})) \qquad (i = 1,2,,,,n) \qquad (6)$$

where $R_{i,j}$ denotes the position of the ith orbital in the jth unit cell and φ_i specifies the atomic wavefunction at site i. Therefore, the eigenvalue of $E_i(\vec{k})$, which means the energy dispersion relation, is given by the secular equation

$$\det[H - E_i S] = 0 \qquad (7)$$

Hence

$$E_i(\vec{\mathrm{k}}) = \frac{\langle \Phi_\mathrm{i} | \mathrm{H} | \Phi_\mathrm{i} \rangle}{\langle \Phi_\mathrm{i} | \Phi_\mathrm{i} \rangle} = \frac{H_{i,i}(\vec{\mathrm{k}})}{S_{i,i}(\vec{\mathrm{k}})} \qquad (8)$$

Fig. 2.2 shows the nearest neighbor vectors in real space

$$\delta_1 = \frac{a_{c-c}}{2}(1, \sqrt{3}), \qquad \delta_2 = \frac{a_{c-c}}{2}(1, -\sqrt{3}), \quad \delta_3 = -a_{c-c}(1, 0) \qquad (9)$$

Regarding each unit cell owns two non-equivalent sublattices A and B, the diagonal terms H_{AA} and H_{BB} are given as

$$H_{AA} = H_{BB} = \frac{1}{N}\sum_{i,j=1}^{N} e^{i\vec{k}\cdot(R_i - R_j)} \langle \varphi_A(\vec{r} - R_j) | H | \varphi_A(\vec{r} - R_i) \rangle$$

$$= \frac{1}{N}\sum_{i=j}^{N} \varepsilon_{2p} = \varepsilon_{2p} \qquad (i, j = 1, 2, , , , N) \qquad (10)$$

where ε_{2p} is the orbital *2p* level energy and it contributes most to the diagonal terms H_{AA} and H_{BB} as the formation of π-bond. In addition, the off-diagonal elements H_{AB} and H_{BA} represent the hopping terms, which are described as

$$H_{AB} = \frac{1}{\mathrm{N}}\sum_{\mathrm{i,j}}^{\mathrm{N}} e^{i\vec{k}\cdot(R_i - R_j)} \langle \varphi_\mathrm{A}(\vec{\mathrm{r}} - \mathrm{R_j}) | \mathrm{H} | \varphi_\mathrm{B}(\vec{\mathrm{r}} - \mathrm{R_i}) \rangle$$

$$= \frac{1}{N}\sum_{i,j=1,2,3}^{N} e^{i\vec{k}\cdot(R_i - \delta_j)} \langle \varphi_A(\vec{r} - \delta_j) | H | \varphi_B(\vec{r} - R_i) \rangle = t\left(e^{i\vec{k}\cdot\delta_1} + e^{i\vec{k}\cdot\delta_2} + e^{i\vec{k}\cdot\delta_3}\right)$$

$$= t\left(e^{-iak_x} + 2e^{\frac{iak_x}{2}} cos\left(\frac{\sqrt{3}}{2}ak_y\right)\right)$$

$$= t \cdot f(k) \qquad (11)$$

where $t \approx 3.0$ eV is the nearest hopping energy. Because the constructed Hamiltonian is Hermitian, it is easy to prove the other off-diagonal term $H_{BA} = H^*_{BA} = tf(k)^*$ from the

matrix property. Due to the integrity of function set, we obtain overlap matrix S_{AA} = $S_{BB}=1$, the detailed process is

$$S_{AA}(\vec{k}) = \langle \Phi_A | \Phi_A \rangle$$

$$= \frac{1}{N}\sum_{i,j}^{N} e^{i\vec{k}\cdot(R_{Ai}-R_{Aj})}\langle \varphi_A(\vec{r}-R_{Aj})|\varphi_A(\vec{r}-R_{Ai})\rangle =$$

$$= \frac{1}{N}\sum_{i=1}^{N} \langle \varphi_A(\vec{r}-R_{Ai})|\varphi_A(\vec{r}-R_{Ai})\rangle = 1 = S_{BB}(\vec{k})$$

and $S_{BA} = S^{*}_{AB}=s_0 f(k)^{*}$ via Hermitian matrix property, s_0 is a constant which demonstrates adjacent orbital sites that are not orthogonal. Hence equation (8~11) transforms into a 2x2 matrix:

$$H = \begin{pmatrix} \varepsilon_{2p} & tf(k) \\ tf(k)* & \varepsilon_{2p} \end{pmatrix}, \quad S = \begin{pmatrix} 1 & s_0 f(k) \\ s_0 f(k)* & 1 \end{pmatrix} \qquad (12)$$

Then substitute equation (12) into the speculation equation (7) and the eigenenergy $E(k)$ can be written in function $f(k)$ and momentum vector k

$$E_{\pm}(\vec{k}) = \frac{\varepsilon_{2p} \pm t|f(k)|}{1 \mp s_0|f(k)|} \quad and \quad f(k) = e^{-iak_x} + 2e^{\frac{iak_x}{2}} cos\left(\frac{\sqrt{3}}{2}ak_y\right) \qquad (13)$$

where the plus and minus sign denote the conduction and valence bands, respectively.

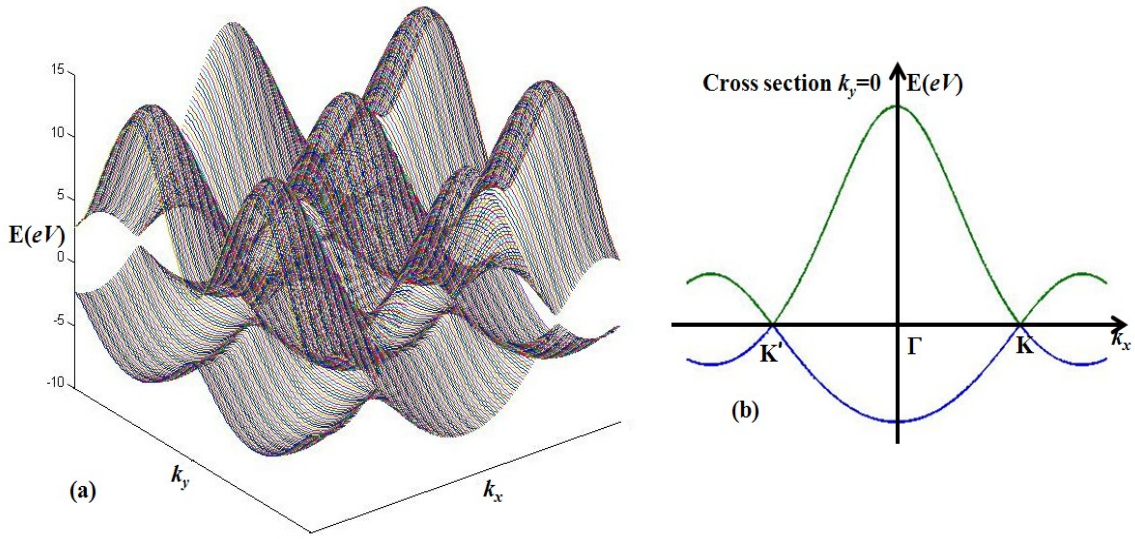

Fig. 2.3 Monolayer graphene energy dispersion relation from equation (13) (a) 3D image (b) Cross section at k_y=0.

Fig. 2.3(a) and (b) plot the energy dispersion relation of single layer graphene and its cross section at k_y=0. The parameters to calculate this band structure as depicted in equation (13) are set as t= 3.033 eV, ε_{2p}=0 and s_0=0.129[5]. We note that the conduction band, also referred as anti-bonding π^*-band, touches the valence band (π-band) at the corner K (K') point. Therefore, single layer graphene is a gapless semiconductor. We expand $f(k)$ in equation (13) to the first order, as $k\hbar = \hbar K+Q$

$$f(k) = e^{-\frac{iaQ_x}{\hbar}} + 2e^{\frac{iaQ_x}{2\hbar}} cos\left(\frac{aQ_y}{4\hbar}\right) \qquad (14)$$

$$= (1 - iaQ_x/\hbar) + 2\left(1 + i\frac{aQ_x}{2\hbar}\right)\left(-\frac{1}{2} - \frac{aQ_y}{4\hbar}\right) = -\frac{ia}{2\hbar}(Q_x + iQ_y)$$

Thus at the low energy regime, the dispersion relation approximately equals to

$$E_{\pm}(Q) \approx \pm v_F|Q| + O[(Q/K)^2] \qquad (15)$$

where Fermi velocity v_F is given as $v_F = \frac{3ta}{2} \sim 10^6 m/s$ [6]. The striking feature of Fig. 2.3(b) is the linear relation between the energy dispersion and its momentum Q around the Dirac point, as seen in Eq. (15), which is also the reason why graphene is called 'Dirac' material. The electrons or holes in monolayer graphene are massless, and cannot be described by Schrödinger equation, but by Dirac-like prescription (equation 16) of relativistic particles with pseudospin $\vec{\sigma}$ [1].

$$H = v_F p\vec{\sigma} \cdot \hat{n} \qquad (16)$$

II-2. Bilayer and trilayer graphene structure

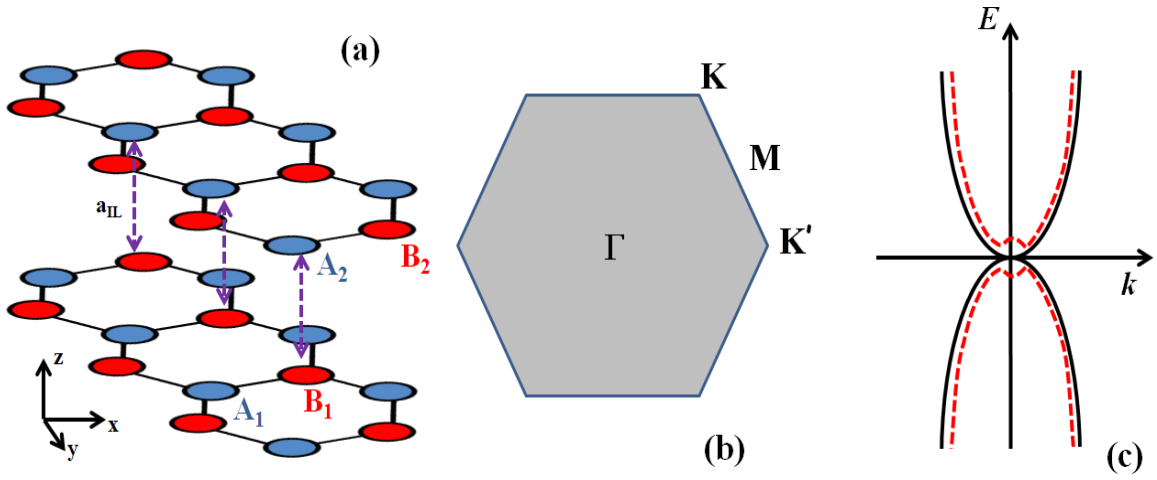

Fig. 2.4 Lattice of bilayer graphene, its Brillouin zone and schematic band structure (a) Bilayer graphene lattice structure in real space. (b) Its first Brillouin zone in the reciprocal momentum space with different highly symmetric points: Γ (BZ center), M (the center of edges), and K (K′) at BZ edge corners. (c) Schematic image of bilayer graphene low energy band dispersion by nearest neighbor coupling tight binding model, the red dash line considers external electric field while the black solid line does not.

The lattice structure of bilayer graphene is shown in Fig. 2.4(a) and each unit cell contains four atoms, two from each layer, marked as atoms A_1, B_1, A_2 and B_2. B atoms (B_1) of the lower layer are located directly underneath the upper layer A atoms (A_2), and this structure is called as Bernal (AB) stacking. In addition, we can apply the tight binding approximation to evaluate the energy dispersion relation of the bilayer graphene around the Dirac point.

To simplify the calculation, only the nearest neighbor hopping is considered, which includes the in-plane coupling between A_1 and B_1 atoms, A_2 and B_2 atoms, and the interlayer hopping between A_1 and B_2 atoms. The degeneracy of bilayer graphene band dispersion is 4=2x2 which counts the layer symmetry (top layer and bottom layer) and valley symmetry (Dirac cones K and K′), hence there are four parabolic bands at each of the two Dirac cones K and K′. The conduction bands and valence bands touch each other at Dirac point (k=0) in the absence of external electric field condition. We assume the onsite energy D of all sites atoms is independent of layer/valley symmetry and set to zero, D=0. The Hamiltonian[7, 8] of bilayer graphene near Brillouin zone can be described by a 4x4 matrix for each of these highly symmetry Dirac cones K and K′ respectively,

$$H_K = \begin{pmatrix} -D & v_F k & 0 & 3\gamma_3 a k^* \\ v_F k^* & -D & \gamma_1 & 0 \\ 0 & \gamma_1 & -D & v_F k \\ 3\gamma_3 a k & 0 & v_F k^* & -D \end{pmatrix}, \qquad (18)$$

where $k = k_x + ik_y$ is the complex momentum, v_F is the Femi velocity, $\gamma_1$is the hopping energy between atom A_2 and atom B_1, γ_3 is the hopping energy between atom A_1 and

atom B_2, and we can easily obtain $H_{K'} = H_K^*$ due to their Hermitian matrix property. If we consider that onsite energy is much smaller than in-plane hopping energy and ignore second nearest interlayer hopping γ_3=0, the eigenenergies derived from equation (18) and the secular equation det[H-ES]=0 are

$$E^2{}_{\pm} = D^2 + v_F^2 k^2 + {\gamma_1}^2/2 \pm \sqrt{4D^2 v_F^2 k^2 + {\gamma_1}^4/4} \qquad (19)$$

If the layer symmetry, or sublattices A_2 and B_1, is broken due to external perturbations $D \neq 0$, say by doping or gating one of these two layers, a gap appears between conduction and valence band. The physical reason is that the perturbation changes the onsite energy of effective Hamiltonians H_K, $H_{K'}$ from zero to finite values E_+ and E_-, and they have a displacement[10] $\Delta \approx \frac{2\gamma_1 D}{\sqrt{{\gamma_1}^2+4D^2}}$, which is the created band gap as shown in the red dash line of Fig. 2.4(c). Hence the breaking of interlayer symmetry results in the opening of an energy gap, which has been extensively studied theoretically and experimentally[7-12, 15, 16].

In addition to single-layer and bilayer graphene, trilayer graphene (TLG) also attracted much interest from the graphene community[13-15]. There are two stacking orders: Bernal (ABA-TLG) and Rhombohedral (ABC-TLG) trilayer graphene, as depicted in Fig. 2.5. In TLG, each unit cell contains six atoms, two from each layer, marked as atoms A_1, B_1, A_2, B_2, A_3 and B_3. The AB stacking of the first two layers in TLG is the same as that in the bilayer graphene. The third layer of the ABA-TLG (A_3-B_3 plane) has the same stacking order as the A_1-B_1 plane, while the third layer of the ABC-TLG shifts to align atom A_3 with atom B_1 and atom $B_3$with atom A_2. Raman spectroscopy is effective at distinguishing these stacking orders, which will be discussed in the next section.

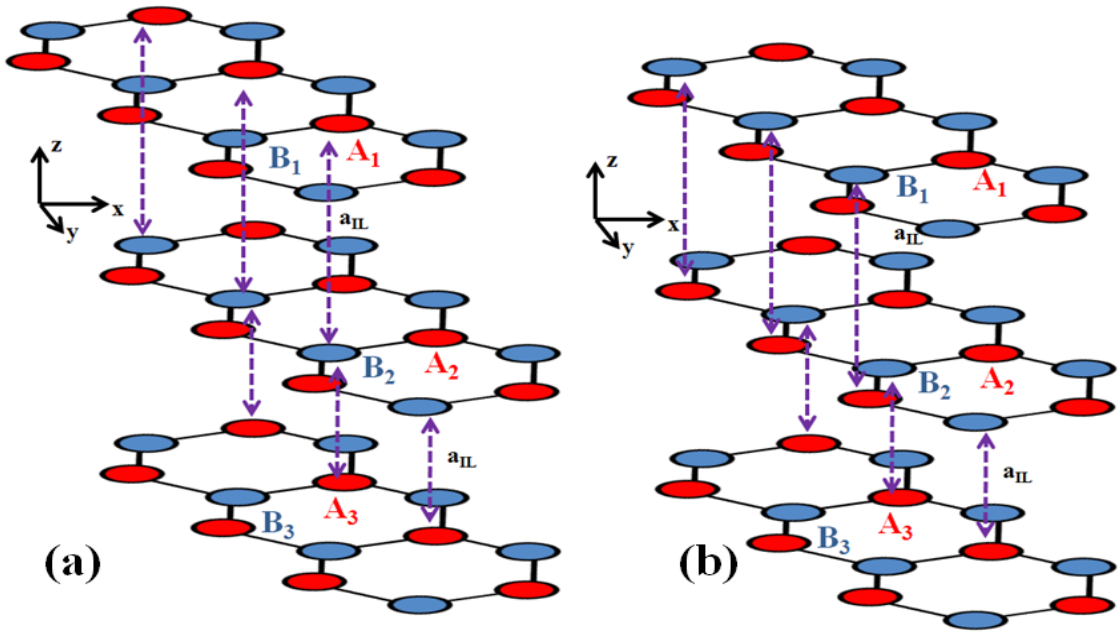

Fig. 2.5 Different lattice stacking of trilayer graphene in real space: (a) Bernal (ABA) stacking trilayer graphene. (b) Rhombohedral (ABC) trilayer graphene.

The difference in the electrical properties of ABA-TLG and ABC-TLG is quite intriguing. ABA-TLG is predicted[16] to be a conductor with a band-gap overlap in a perpendicular electric field, while ABC-TLG behaves as a semiconductor with a band gap under the field. Thus TLG provides a versatile platform to study both fundamental physics and electronic applications.

II-3. Graphene layer stacking order and its Raman characterization

When additional layers are stacked on a monolayer graphene, its properties are changed due to the extra hopping between different sites. The intra-layer carbon-carbon lattice

length is still $a_{C\text{-}C} \approx 0.142$ nm, while the interlayer distance is $a_{IL} \approx 0.335$ nm[1]. The interlayer displacement is twice longer than the in-plane atoms' distance, hence the Van der Waals forces between layers is much weaker[17].

To identify the number of layers in a given sheet, many metrology tools can be utilized, such as optical microscope[1], atomic force microscope (AFM)[17], transmission electron microscopy (TEM)[4], Raman[3] and infrared spectroscope[19]. Comparing with other detection methods, Raman spectroscopy provides a reasonable compromise among yield accuracy, throughput speed, sampling size and non-invasiveness. Thus we use Raman spectroscopy to identify the number of layers, and the stacking orders for trilayer graphene, by examining the spectrum's intensity and shape.

II-3.1. Basic introduction to Raman spectroscopy

Raman spectroscopy[20] is a mature method to probe specimen crystallographic orientations, elemental composition and vibration modes. This technique has been extensively used in materials research, with the advantages that sample preparation is easy and non-destructive and requires no contact, and the output is fast. Its principle is based on the Raman effect[21], which describes the scattering between the incident monochromatic light and the molecular bond or electron cloud of the sample. During the scattering process, absorption or emission of phonon occurs if an atom is displaced from its original equilibrium state, which also results in a shift in the emitted photon energy.

Such Raman shifts could unveil the vibration, rotation or other low-frequency modes of the specimen.

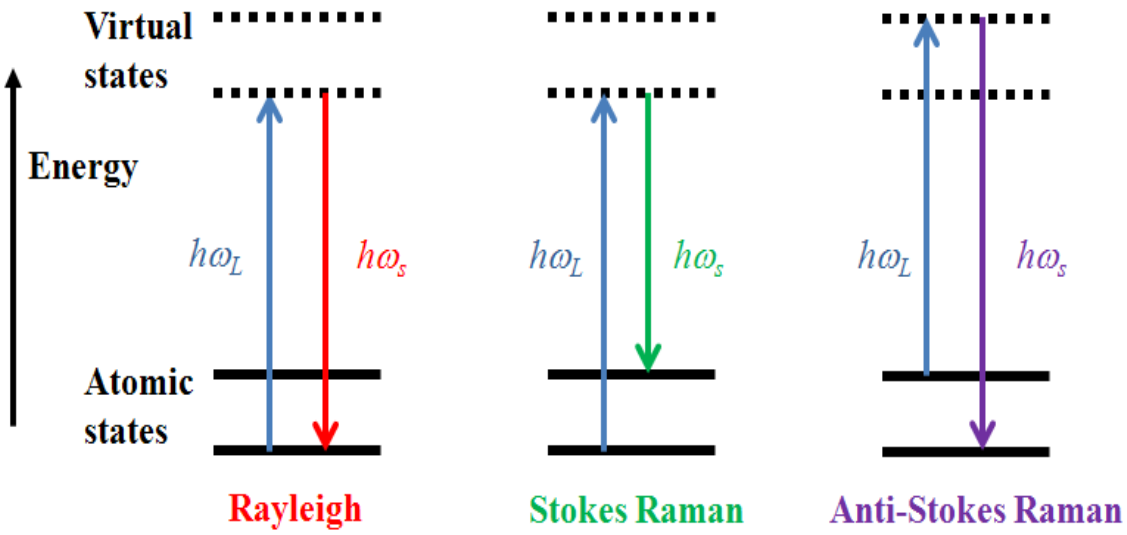

Fig. 2.6 The illustration of elastic scattering and non-elastic scattering: incident laser with frequency ω_L excites a scattered photon (frequency = ω_s) from the atomic equilibrium state to a virtual state and results in three types of scattering: Rayleigh (non-elastic, $\omega_L = \omega_s$), Stokes Raman (elastic, $\omega_L > \omega_s$) and Anti-Stokes Raman (elastic, $\omega_L < \omega_s$).

In elastic scattering (also called as Rayleigh scattering), an incident photon with energy $h\omega_L$ interacts with the atom, which is excited to a virtual state and returns to the same ground state while emitting a photon with energy $h\omega_L$. There is no energy exchange during this process, therefore elastic scattering does not cause Raman shift. On the other hand, the non-elastic scattering (Stokes and Anti-Stokes Raman scattering) results in emission of photons with altered energy as the atom relaxes from the virtual state to a final state that has different vibration modes from the initial state. Thus, Raman scattering

involves energy transfer from the incident light to the lattice, $h\omega_s = h\omega_L \pm h\omega_p$, where $h\omega_p$ is the energy of the created/annihilated phonons. In Stokes (anti-Stokes) scattering, a phonon is emitted (absorbed), so the scattered photon frequency ω_s is lower (higher) than ω_L.

A Raman spectrum plots the Raman scattering intensity as a function of Raman shift. Raman shift is usually in the unit of wavenumber (cm^{-1}) and is identified as the difference in wavenumber between the incident and scattered photons. Incident photons typically have wavenumber ~10^5 cm^{-1} (on the order of 100 nm in wavelength), but the molecular or atomic lattice constant is less than 1nm, which means the wavenumber of reciprocal-lattice is on the order of $10^7 cm^{-1}$. Therefore, the captured Raman scattering signal is always located in the center of Brillouin zone or near zero momentum point in the phonon energy dispersion relation. The Raman intensity is the accumulation of all the non-elastic scattering optical phonons.

II-3.2. Raman response of mono-, bi-, and tri-layer graphene

Our Raman spectrometer is Dilor XY model equipped with a 532 nm (green) laser. The number of layers in a graphene sheet can be identified from the shape of graphene-specific Raman peaks D, G, *2*D and the intensity ratio of *I(G)/I(2D)*[22]. Typical Raman spectrum of pristine single layer graphene and bilayer graphene are shown in Fig. 2.7.

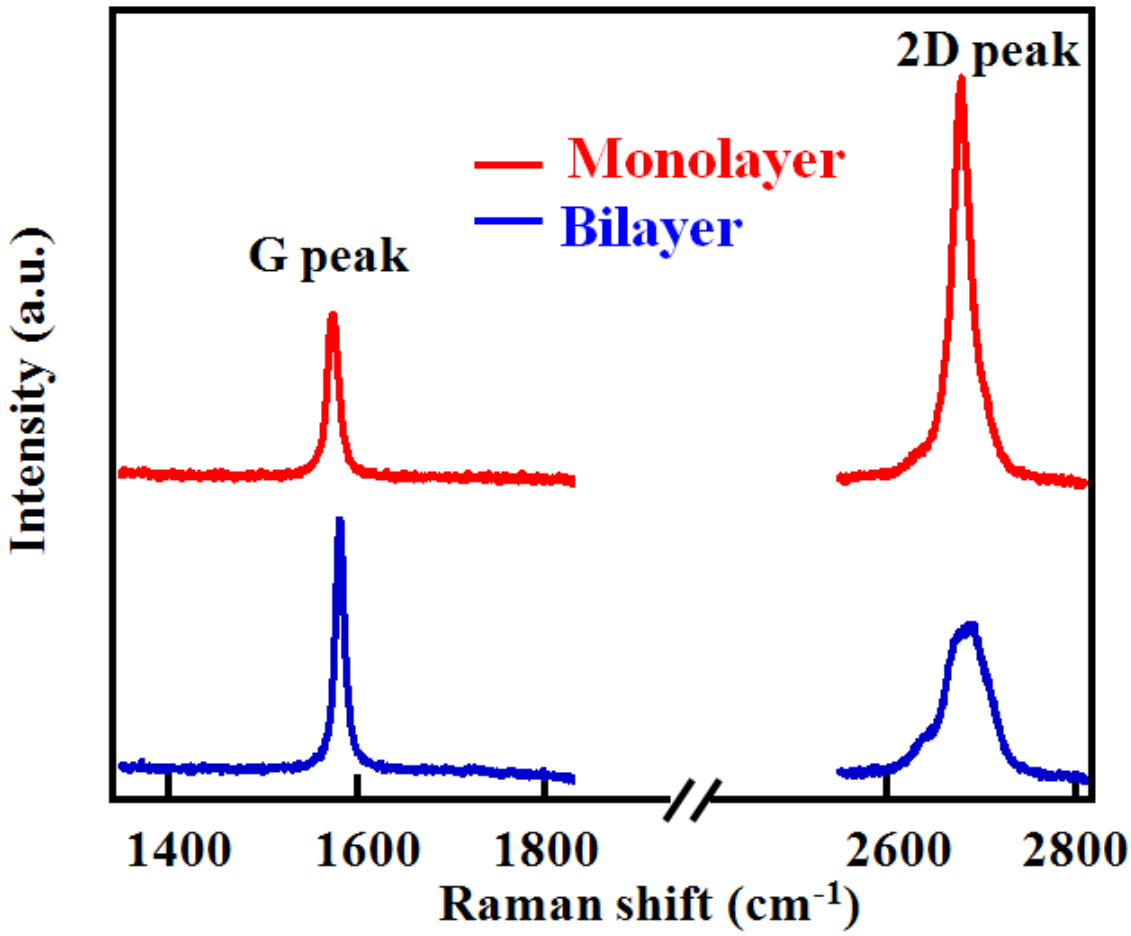

Fig. 2.7 Raman spectrum of mono- and bi-layer graphene: the laser wavelength is 532 nm.

The most prominent peaks are located at ~1575 cm^{-1} (G peak) and ~2650 cm^{-1} (2D peak). The point group of single layer graphene is D_{6h} and its G peak is related to the first order Raman scattering process with E_{2g} symmetry near Brillouin zone center Γ. One charge carrier, like a hole, is excited to the conduction band by the incident laser photon (as depicted in Fig. 2.8(a)) and this process, which reveals materials' in-plane vibration mode, is non-elastic. Then this electron releases a G-band phonon, returns to the initial state around momentum $k=0$ point and emits a photon by recombining with another hole.

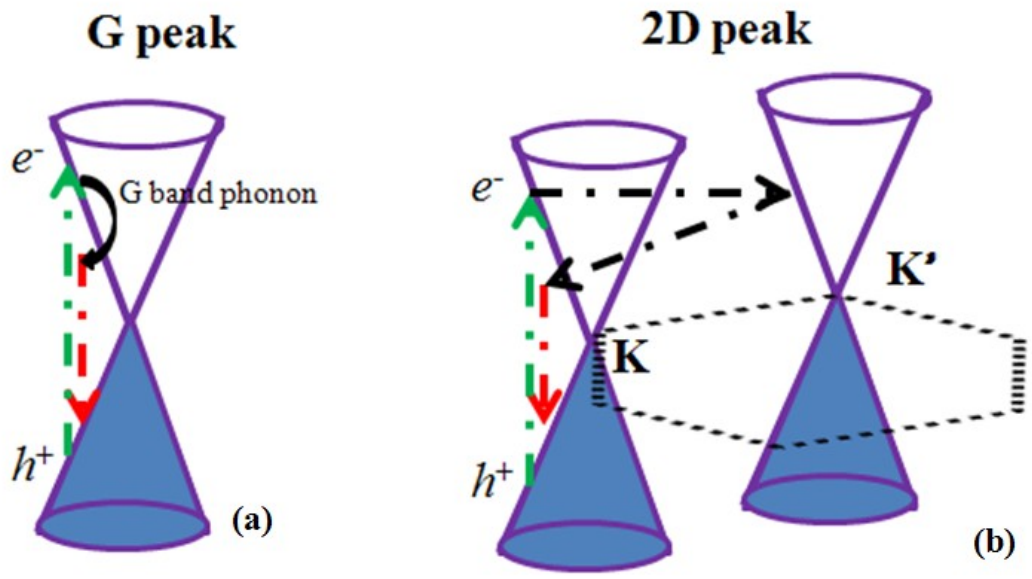

Fig. 2.8 Schematic Raman transitions for G peak and 2D peak in single layer graphene: (a) First-order G-band process, where e^- is electron and h^+ is hole. (b) The intervalley double-resonance (DR) process for 2D peak. The solid purple line draws the Dirac cone of single layer graphene, blue shaded region is valence band, and K and K' are two non-equivalent Dirac point in the same reciprocal lattice.

On the other hand, the 2D peak involves a two phonon double-resonance process, as shown in Fig. 2.8(b). An electron with wavenumber k at the Dirac cone K absorbs the energy of an incident photon and is excited to the conduction band. Then this electron is non-elastically scattered by a phonon with wavenumber p to a new state with wave-number $p+k$ at the non-equivalent Dirac cone K′. Finally, this $p+k$ electron is non-elastically scattered back to the K valley by a second phonon p' and emits a photon by recombining with another hole at k state. So this whole process involves two steps of non-elastic intervalley scattering[23]. The 2D peak of monolayer graphene is very sharp and

can be fitted by a single Lorentzian function; its intensity is twice that of the G peak, which is unique for the linear energy dispersion.

Bilayer graphene belongs to the D_{3d} group at the center of Brillouin zone. The G peak intensity increases with the extra layer and the 2D peak starts to broaden with comparable intensity to the G peak. More double-resonance (DR) processes, contributing to 2D peak, are possible because bilayer graphene has four energy bands at the non-equivalent Dirac cones K and K′. Given the phonon symmetry and light absorption selection rules[24, 25], four DR processes with different phonon-emitting frequencies occur as non-elastic intervalley scatterings. Thus the 2D peak of bilayer graphene can be fitted by four Lorentzians with different peak frequencies[24].

Following the logic of bilayer graphene 2D peak, the 2D peak of trilayer graphene can be fitted by six Lorentzians with different resonance frequencies[27]. Fig. 2.9 shows that the peak of ABA-TLG is more symmetric than that of the ABC-TLG, which has a prominent shoulder. Therefore the shape of 2D peak can be used to identify the stacking order of TLG. The ratio *I(G)/I(2D)* increases with increasing layer numbers, so it can be used as a metric to identify the layer number in a graphene thin film[22]. Typically for Raman spectrum with 532 nm laser, *I(G)/I(2D)* for single layer graphene is <0.5, for bilayer is about 1.3, for trilayer graphene ~ 1.5, and increases to ~3 for HOPG.

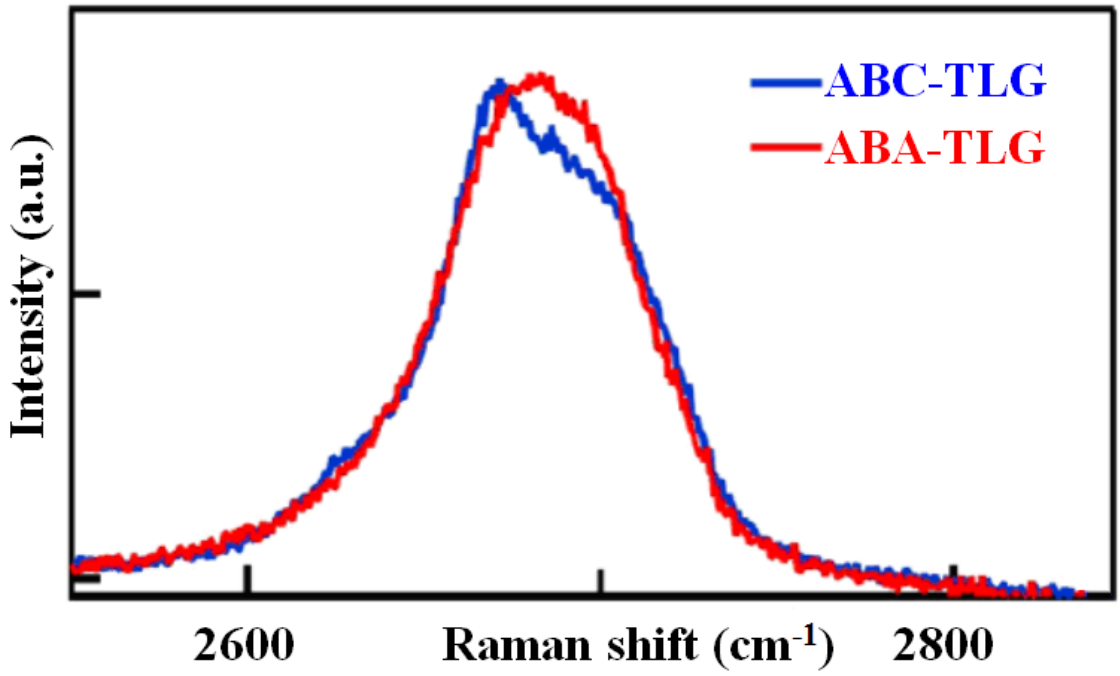

Fig. 2.9 Raman spectrum of ABA- and ABC- trilayer graphene: the laser wavelength is 532 nm.

II-4. Quantum Hall effect (QHE)

The Hall effect[28], which can be used to determine the density and type of charge carriers, is observed in the conductor with an electrical current flow and an applied magnetic field in an orthogonal direction. A standard Hall-bar device (as shown in Fig. 2.10) has six terminals: source (S) and drain (D) to inject current flow I in the x-direction, and the other four terminals T_1~T_4 to detect the voltage drop across various electrodes. An external magnetic field B is applied in the z-direction.

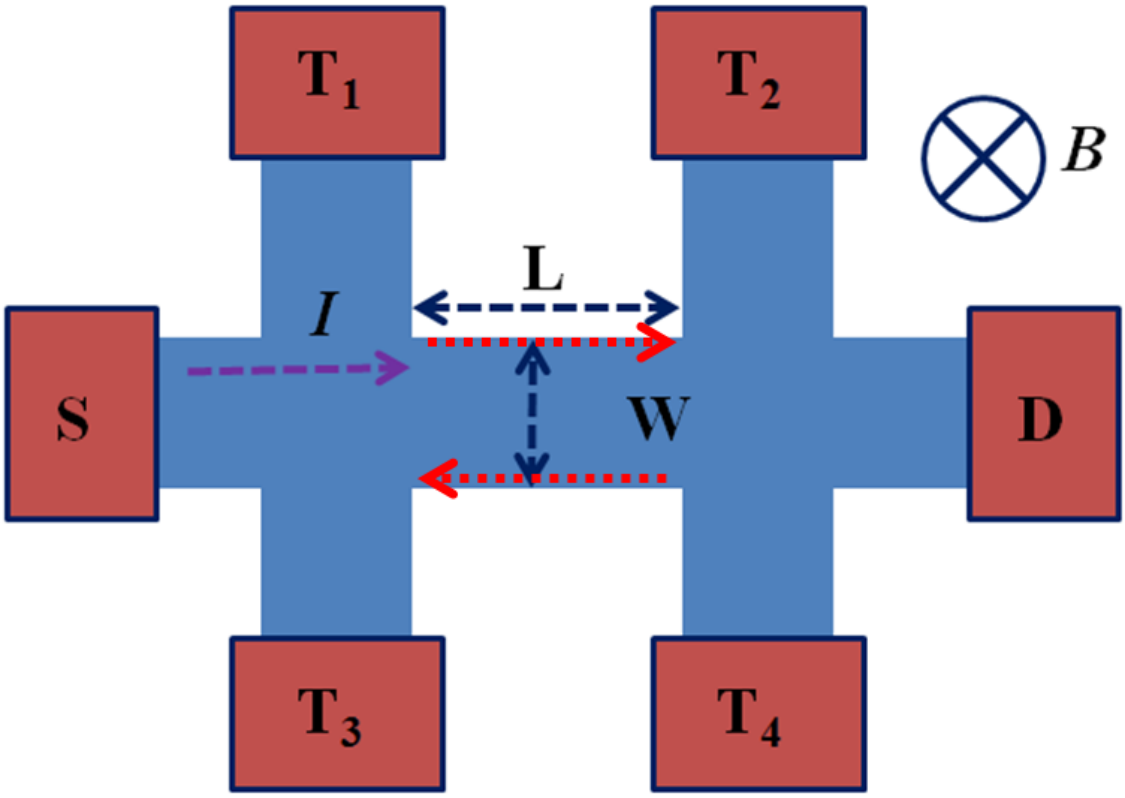

Fig. 2.10 Schematic image of Hall-bar geometry device under magnetic field B. Red arrows denote electron edge transport in quantum Hall regime.

There are two types of voltage drops: longitudinal $V_{xx}=V_1-V_2$ or V_3-V_4, and transverse $V_{xy}=V_1-V_3$ or V_2-V_4. The width and length of the sample are marked as W and L in Fig. 2.10, respectively. Hence the longitudinal resistivity ρ_{xx} and Hall resistivity ρ_{xy} are defined as

$$\rho_{xx} = \frac{V_{xx}}{I}\frac{W}{L}, \quad \rho_{xy} = \frac{V_{xy}}{I} \qquad (21)$$

where W/L is the aspect ratio of the sample. Then we can derive its conductivity σ and charge carrier density n_e,

$$\text{longitudinal conductivity} \quad \sigma_{xx} = \frac{\rho_{xx}}{{\rho_{xx}}^2 + {\rho_{xy}}^2},$$

$$\text{Hall conductivity } \sigma_{xy} = \frac{\rho_{xy}}{{\rho_{xx}}^2 + {\rho_{xy}}^2}$$

$$\text{Charge density } n_e = \frac{1}{e(d\rho_{xy}/dB)} \qquad (22)$$

Observation of the quantum Hall phenomena requires very high mobility samples and sufficiently strong B-fields. Dr. Klaus von Klitzing firstly observed the integer quantum Hall effect[29] on the inversion layer of Si-MOSFETs in 1980. The Hall resistivity of a 2D Si-MOSFET device is quantized at $\rho_{xy} = h/Ne^2$, where *N* is an integer; at each plateau, the longitudinal resistance decreases to zero. Therefore the Hall conductivity σ_{xy} follows $\sigma_{xy} = \frac{\rho_{xy}}{{\rho_{xx}}^2+{\rho_{xy}}^2} = 1/\rho_{xy} = Ne^2/h$. The underlying physical picture is as follows. The electrons in the 2DEGs adopt cyclotron motion under perpendicular magnetic field *B*, and these orbits are quantized into discrete energy levels. The Hamiltonian in this system is

$$H = \frac{1}{2m}\left(\vec{p} + \frac{e\vec{A}}{c}\right)^2 + eEx \qquad (23)$$

where *m* is the effective mass of electrons, $\vec{p}$ is electron's momentum vector, *c* is the speed of light, *E* is the built-in electric field in the sample along the current flow direction (*x* direction) and $\vec{A}$ is the magnetic vector potential. We choose Landau gauge $\vec{A} = (-By, 0, 0)$ for the convenience of calculation. Thus, we can derive the eigenvalue E_N of Hamiltonian (Eq. 23) in Schrödinger equation

$$E_N = \left(N + \frac{1}{2}\right)\hbar\omega_c + V(y)$$

where $\omega_c = eB/m$ is cyclotron frequency, $\hbar$ is Plank's constant. E_N is defined as the energy of the *N*th Landau levels (LLs), and *N* is an integer denoting the LL index. *V(y)* is the confining potential under system's boundary condition. At a fixed charge density, the degeneracy of LL increases with increasing magnetic field, therefore each LL can accommodate more electrons, and the number of filled LLs is reduced (Fig. 2.10(a)).

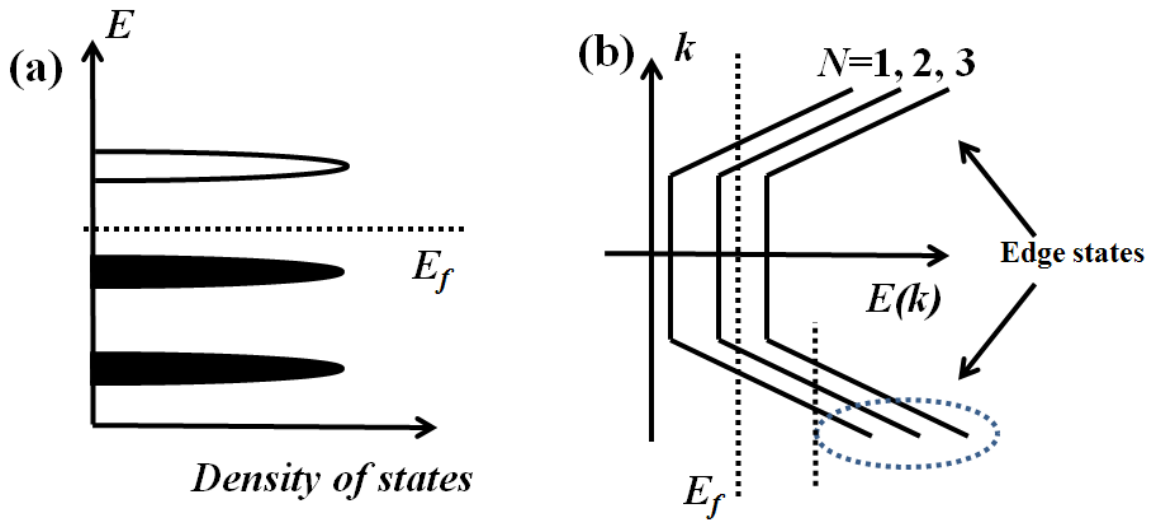

Fig. 2.11 Schematic images of Landau levels and edge states in quantum Hall (QH) regime. (a) 2D density of states (DOS) *vs.* energy *E* in applied magnetic field, E_f is Fermi energy. (b) Dispersion relation *E(k) vs. k* of a bulk rectangular sample in QH regime. Assume its *x*-direction is uniform and *y*-direction is restricted by a confining potential *V(y)*. Note that the wavenumber *k* is proportional to *y*-axis coordinate. The edges states are topologically separated by applied magnetic field.

Based on the Landauer-Büttiker formula[36], at filling factor υ= (*nh*)/(*Be*) (*e* is the electron charge, *h* is Planck's constant, *n* is the charge density), there exist υ edge channels (Fig. 2.11(b)) which are corresponding to a quantized Hall voltage $V_{xy} = Ih/g\upsilon e^2$, where *g* is the degeneracy of the system. The electrons in the edge states in quantum Hall regime

(shown as red arrows in Fig. 2.10) travel in opposite directions of parallel edges. Backscattering is strongly suppressed in the sample when the sample's width W is much larger than the magnetic length of electrons $l_B=\sqrt{\frac{h}{eB}}$ [30]. The absence of backscattering in the quantum Hall regime results a vanishing longitudinal resistivity and dissipationless transport. More detailed discussions about QHE are available in recent comprehensive reviews/ articles[30-32].

II-4.1. Integer QHE in single- and bi-layer graphene

The integer QHE (IQHE) can be observed in and used to identify single layer graphene (SLG) and bilayer graphene (BLG). Quantum Hall conductance of SLG is quantized at half-integer values

$$\sigma_{xy} = 4(N + \tfrac{1}{2})e^2/h,$$

where N is an integer and the factor of 4 arises from valley and spin degeneracy of single layer graphene, e is electron charge and h is Plank's constant. The half-integer shift arises from the coupling between the pseudospin and the orbital movement[33] of Dirac fermions in SLG, which also results from a π-shift as Berry's phase[34, 35]. Fig. 2.12 shows one of the first experimental[34] measurements of the SLG's quantum Hall transport. The energy of Landau levels in SLG is $E_N^{SLG} = \pm v_F\sqrt{2ehBN}$, where v_F is the Fermi velocity, B is the magnetic field and $\pm$ denotes electrons and holes, respectively. Under high magnetic

field B=14 T (Fig. 2.12), the lowest Landau level E_0 at charge neutrality point is shared by electrons and holes.

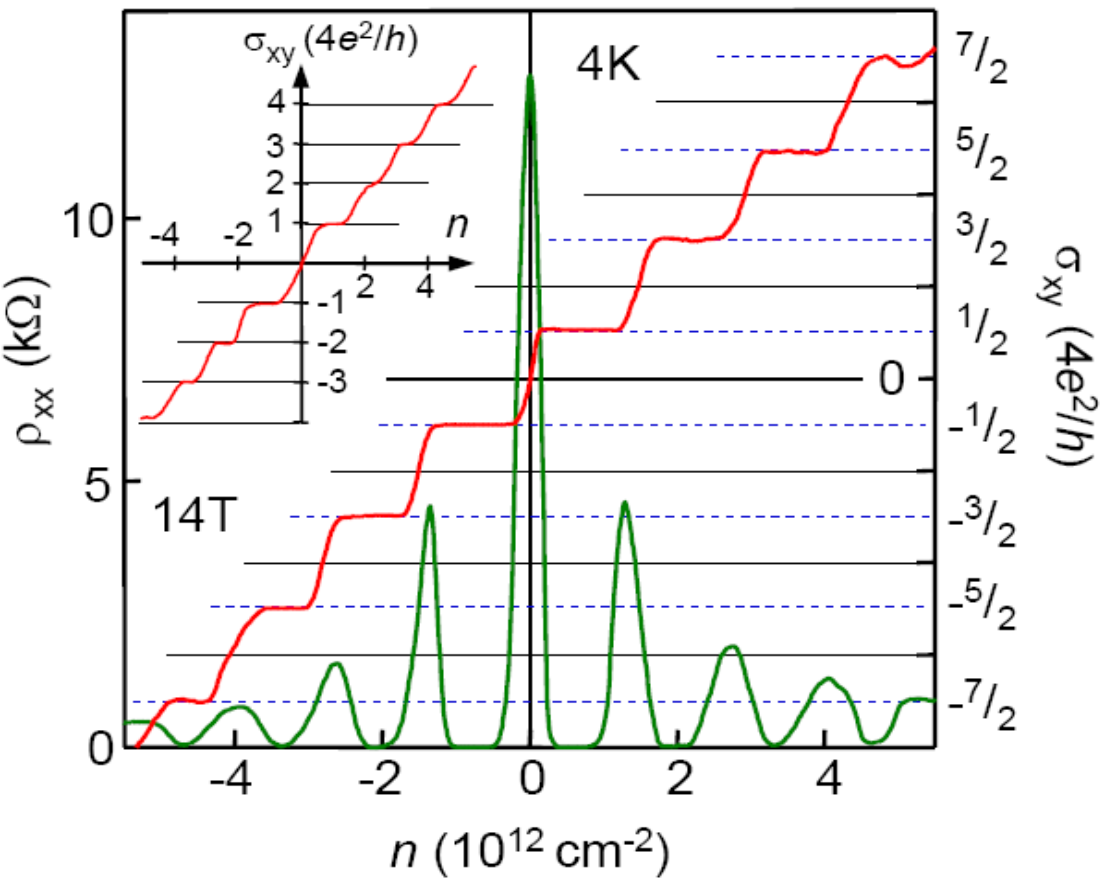

Fig. 2.12 Integer quantum Hall effect of single layer graphene and bilayer graphene (inset), where n is graphene's charge density, and applied magnetic field is 14 T**, Reprint with permission from K. S. Novoselov, A. K. Geim, S. V. Morozov, D. Jiang, M. I. Katsnelson, I. V. Grigorieva, S. V. Dubonos, A. A. Firsov, Nature, 438, 197 (2005). Copyright (2005) © Nature Publishing Group**

The quantum Hall feature of pristine BLG follows integer series $\sigma_{xy} = 4N\frac{e^2}{h}, N = \cdots -3, -2, -1, 1, 2, 3 \cdots$, as shown in Fig. 2.12 inset. The missing zero plateau at zero energy

is due to eight-fold degeneracy (valley, spin and orbital) of bilayer graphene, which results in an $8e^2/h$ conductance step between the first quantum Hall plateaus N=$\pm$1. The energy of Landau levels of BLG is $E_N^{BLG} = \pm\frac{heB}{m^*}\sqrt{N(N-1)}$, where m^*~$0.02 - 0.04m_e$ is the effective mass of charge carrier in BLG and m_e is electron's rest mass, B is magnetic field and $\pm$ denotes electrons and holes, respectively. When the layer symmetry of BLG is broken by external electric field, a plateau at $0e^2/h$ (*i.e.* insulating plateau at the charge neutrality point) can be observed. In chapter IV, we will discuss our quantum Hall transport measurement and band-gap opening in bilayer graphene.

References:

1) A. H. Castro Neto, F. Guinea, N.M.R. Peres, K.S. Novoselov, A.K. Geim, *Rev. Mod. Phys*. **81**, 109 (2009)

2) A.K. Geim, *Rev. Mod. Phys.* **83**, 851 (2011)

3) A. C. Ferrari, J. C. Meyer, V. Scardaci, C. Casiraghi, M. Lazzeri, F. Mauri, S. Piscanec, D. Jiang, K. S. Novoselov, S. Roth, A. K. Geim, *Phys. Rev. Lett.* **97**, 187401 (2006)

4) A.K.Geim, K.S. Novoselov, *Nature Materials* **6**, 183-191 (2007)

5) E. McCann, arXiv:1205.4849v1 (2012)

6) P. R. Wallace, *Physical Review* **71** (9), 622-634 (1947)

7) E. McCann, *Phys. Rev. B* **74**, 161403R (2006)

8) M. Koshino, T. Ando, *Phys. Rev. B* **73**, 245403 (2006)

9) Y. Barlas, R. Cote, J. Lambert, A.H. MacDonald, *Phys. Rev. Lett.* **104**, 096802 (2010)

10) E. V. Castro, K. S. Novoselov, S. V. Morozov, N. M. R. Peres, J. Dos Santos, J. Nilsson, F. Guinea, A. K. Geim and A. H. Castro Neto, *Phys. Rev. Lett.* **99**, 216802 (2007)

11) L. Jing, J. Velasco Jr., P. Kratz, G. Liu, W. Bao, M. Bockrath, C. N. Lau, *Nano Lett.***10**, 4000 (2010)

12) J. B. Oostinga, H.B. Heersche, X. Liu, A.F. Morpurgo, L.M. K. Vandersypen, *Nature Materials* **7**, 151 (2007)

13) W. Bao, L. Jing, J. Velasco Jr., Y. Lee, G. Liu, D. Tran, B. Standley, M. Aykol, S. Cronin, D. Smirnov, M. Koshino, E. McCann, M. Bockrath, C.N. Lau, *Nature Physics* **7**, 948-952 (2011)

14) L. Zhang, Y. Zhang, J. Camacho, M. Khodas and I. A. Zaliznyak, *Nature Physics* **7**

(12), 953-957 (2011)

15) F. Zhang, J. Jung, G. A. Fiete, Q. A. Niu and A. H. MacDonald, *Phys. Rev. Lett.* **106** (15), 156801 (2011)

16) M. Aoki, H. Amawashi, *Solid State Communication* **142**, 123 (2007)

17) K. S. Novoselov, D. Jiang, F. Schedin, T. J. Booth, V. V. Khotkevich, S. V. Morozov, A. K. Geim, *PNAS* **102**, 10451 (2005)

18) J. E. Lennard-Jones, *Proceedings of the Physical Society* **43 (5)**, 461, (1931)

19) Kazu Suenaga, Masanori Koshino, *Nature* **468**, 1088–1090 (2010)

20) Gardiner, D.J. *Springer-Verlag*. **ISBN 978-0-387-50254-0**. (1989)

21) C.V. Raman, and K.S. Krishnan, *Nature* **121**, 501 (1928)

22) D. Graf, F. Molitor, K. Ensslin, C. Stampfer, A. Jungen, C. Hierold, L. Wirtz, *Nano Lett.* **7,** 238 (2007)

23) Mildred S. Dresselhaus, Gene Dresselhaus, Ado Jorio, Group Theory: Application to the Physics of Condensed Matter, Springer, Berlin, 2008

24) L.G. Cançado, A. Reina, J. Kong, M.S. Dresselhaus, *Phys. Rev. B* **77,** 245408 (2008)

25) A. Grüneis, R. Saito, Ge.G. Samsonidze, T. Kimura, M.A. Pimenta, A. Jorio, A.G. Souza Filho, G. Dresselhaus, M.S. Dresselhaus, *Phys. Rev. B* **67**, 165402 (2003)

26) L.M. Malard, M.H.D. Guimarães, D.L. Mafra, M.S.C. Mazzoni, A. Jorio, *Phys. Rev. B* **79**, 125426 (2009)

27) M.A. Pimenta, G. Dresselhaus, M.S. Dresselhaus, L.G. Cançado, A. Jorio, R. Saito, *Phys. Chem. Chem. Phys.* **9**, 1276-1291 (2007)

28) Edwin Hall, *American Journal of Mathematics*, **2 (3)**, 287–292 (1879)

29) K. v. Klitzing, G. Dorda, and M. Pepper, *Physical Review Letters* **45**, 494–497 (1980)

30) S. Datta, *Electronic Transport in Mesoscopic Systems*, (Cambridge University Press, 1995)

31) S. Girvin and R. Prange, *the Quantum Hall Effect*, 2nd ed (Springer- Verlag, New York, 1990)

32) D. J. Griffiths, *Introduction to Quantum Mechanics*, 1st ed. (Addison Wesley, 2004)

33) G.P. Mikitik, Y. Sharlai, *Physical Review Letters* **82**, 2147 (1999)

34) K. S. Novoselov, A. K. Geim, S. V. Morozov, D. Jiang, M. I. Katsnelson, I. V. Grigorieva, S. V. Dubonos, A. A. Firsov, *Nature* **438**, 197 (2005)

35) Y. Zhang, J. Tan, H.L. Stormer, P. Kim, *Nature* **438**, 201 (2005)

36) M. Büttiker, *Physical Review B* **38** (14), 9375 (1988)

Chapter III. Fabrication and characterization of bilayer graphene *pnp* device

Bilayer graphene has drawn much attention due to its unique bands structure[1, 2]. The conduction band of bilayer graphene touches the valance band at the Dirac point, while the breaking of the interlayer symmetry will drag the touching bands apart. This makes bilayer graphene a two-dimensional semiconductor with tunable bandgap[3,4]. Its charge carriers behave as massive Dirac fermions in the language of Schrödinger equation combined with Dirac equation, giving rise to numerous novel properties, such as excitonic condensation[5], novel integer and fractional quantum Hall features[6,7]. In this chapter, we will discuss the fabrication procedures and experimental setups for suspended dual-gate bilayer graphene device, as well as our characterization results at room temperature for such kind of device.

III-1. Graphene and substrate preparation

The starting point of the entire device-fabrication process is the wafer preparation. We utilize commercial 4-inch highly *p*-doped silicon (0.001~0.005 ohm-cm) wafer from University Wafer or Silicon Quest. The silicon wafer is 500 μm thick, with one side highly polished and covered by thermally grown 300nm-thick SiO_2 as the dielectric layer, which is critical for graphene detection and observation under optical microscope[8].

The 4-inch wafer is diced into 4.8 mm*4.8 mm squares as shown in Fig. 3.1(a) and 3.1(b). We peel off the diced small pieces from the 4-inch wafer and clean them ultrasonically in acetone solution for twenty minutes to remove the protective layer of photolithography resist. The wafers are then rinsed in isopropyl alcohol (IPA) for 30 seconds and gently dried using compressed nitrogen gas. To remove the organic residue absorbed on the substrate, we dip the wafers into the Piranha solution[6] (a mixture of 98% H_2SO_4 and 30% H_2O_2, volume ratio 3:1~7:1) for five minutes. Afterwards, we rinse the wafers in DI water (20 minutes total). We attempted 10-minute immersion in Piranha solution, but found gate leakage in 90 % of the wafers, most likely due to the thinner/weakened SiO_2 layer.

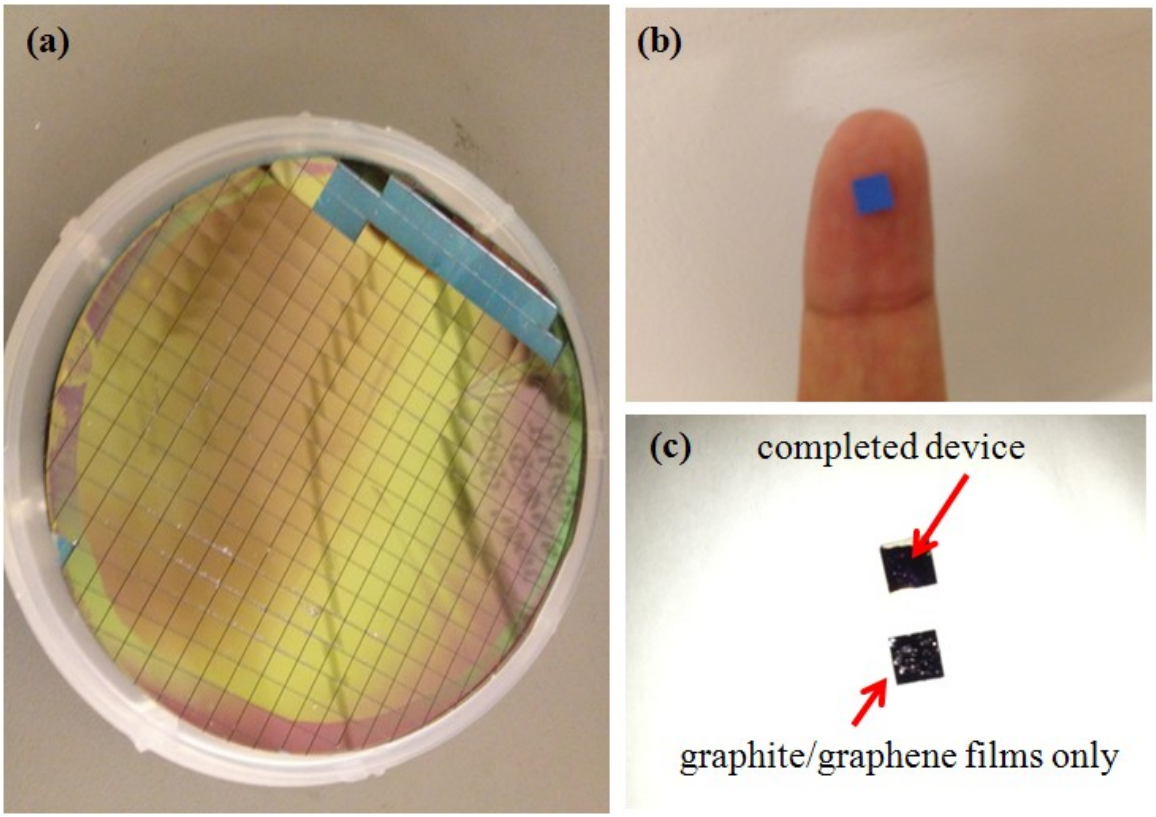

Fig. 3.1 Pictures of different types of wafer: (a) Photo of diced 4inch wafer with protective resist. (b) Photo of a 4.8 mm*4.8 mm wafer after cleaning process. (c) Photo of two single wafers: the upper one with a completed device and the lower one is only deposited with graphene/graphite materials.

We isolate graphene films from bulk graphite onto the Si/SiO_2 substrate immediately after the cleaning process. Fig. 3.1(c) presents the images of two wafers with completed transistor device or only graphene materials, respectively. Our group employs two exfoliation methods: scotch-tape[9] and blade-scratch[10] techniques. Generally speaking, blade-scratch method can yield graphene film of larger size (1~200 μm) than scotch-tape method (1~10 μm). For this bilayer graphene *pnp* device study, the graphene films are obtained by the scotch-tape method, as demonstrated below (Fig. 3.2).

a. Place one small piece of Kish graphite (or HOPG graphite) onto the sticky side of a piece of regular scotch tape;

b. Fold the tape to cover the graphite area, and separate the folded tape to exfoliate the bulk graphite thinner onto both sides; Repeat 5 to 10 times

c. Put the wafers on the "graphite covered" area of the tape;

d. Using tweezers, press the tape and wafer together tightly and squeeze out the induced air bubbles, then peel off the tape gently;

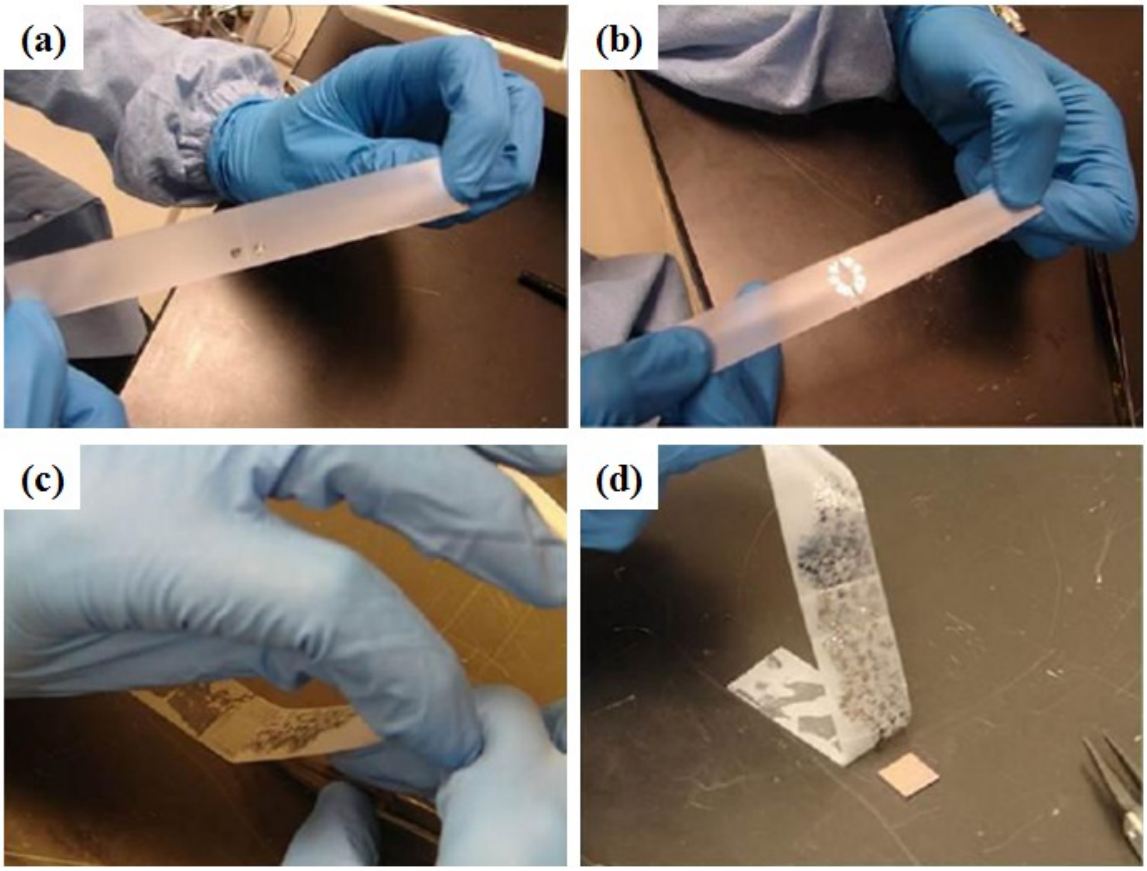

Fig. 3.2 Demonstration of the scotch-tape graphene exfoliation method, adopted from Youtube[11] public online video.

Graphene sheets obtained by this method are randomly scattered over the wafer. So the next step is to search for desirable graphene sheets and identify the number of layers. The fastest detection method is optical contrast through microscope with 500~1000 magnification. Fig. 3.3(a) shows an optical image of graphene, obtained by the blade-scratch method, with different number of layers under 600 times magnification. Fig. 3.3(b) depicts layer information of graphene – relative green channel shift *I(flake)* of image RGB value as function of layer number[12]. Its formula is defined as

$$I(flake) = \frac{G(substrate) - G(flake)}{G(substrate)} \qquad (1)$$

where *G(substrate)* is the substrate's absolute green channel value and *G(flake)* is the flake's absolute green channel value. Data from over 40 flakes are shown in Fig. 3.3(b), demonstrating that *I(flake)* can be used to identify different layers. More accurate measurement of layer numbers can be provided by quantum Hall measurements[1] and Raman spectroscopy[13].

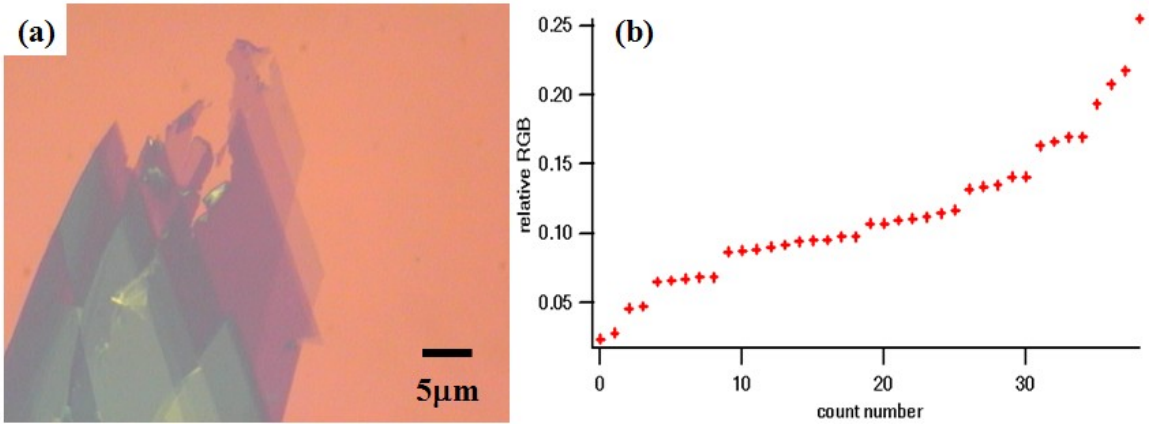

Fig. 3.3 Image of layered graphene and its relative contrast value: (a) Optical image of a typical blade-scratched graphene at magnification 600X. Scale bar: 5 μm. (b) Relative RGB green channel shift value of graphene sheets with various thicknesses vs. sample counts. Data are taken from ~40 samples.

III-2. Dual gated graphene device fabrication by multi-level lithography

The fabrication of dual gated graphene device requires two types of electron beam lithography: standard lithography and multi-level lithography. In this section, we describe the procedures of fabricating alignment marks as the example of standard lithography.

Then we will describe the multi-level lithography process for fabrication of dual gated devices.

III-2.1. Standard electron beam lithography

After locating the graphene film, we firstly fabricate alignment marks around graphene to define its two-dimensional coordinate for the subsequent nanofabrication process via electron beam lithography (EBL, Leo 1550). The e-beam resist bilayer, LOR 1A (lift-off resist 100 nm, from Microchem) /950 PMMA A4 (200 nm, from Microchem), is spun by a spin coater on the Si/SiO2 wafer at 4000 rpm for 45 seconds. The wafer is baked on hot plate at 170°C for 20 minutes after each coating. We drop little dots of silver paint around the target area for the reference under EBL system, then proceed to write the alignment marks using EBL. The LOR and PMMA layers need to be developed separately due to their different selectivity. The exposed PMMA is firstly developed in MIBK solution for 60 seconds, followed by IPA solution rinsing for 60 seconds and blow dry by compressed nitrogen gas (N_2). The underneath LOR1A layer is developed in MF319 solution for 17~25 seconds, following with DI water rinsing 60 seconds and N_2 blow dry. After e-beam writing, we deposit titanium (80 nm) or titanium/gold (10 nm/80 nm) bilayer to complete the alignment marks. Titanium acts as the adhesive layer, and gold has better contrast under scanning electron microscopy (SEM). Both LOR and PMMA can be lifted off by PG Remover. Acetone solution only dissolves PMMA but not LOR. Therefore, undeveloped resists are lifted off in PG remover at 55 °C for 2~5 hours, leaving the

designed metal marks on substrate. The processes described above are illustrated in Fig. 3.4(a)~(d)

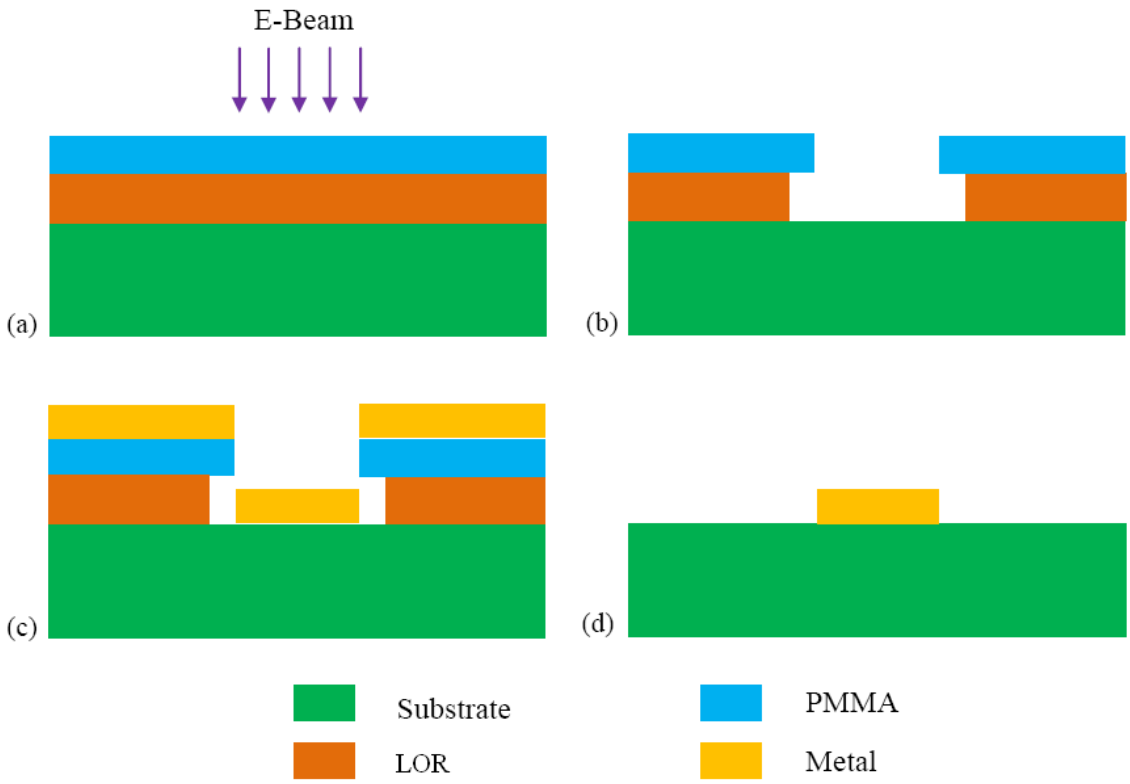

Fig. 3.4 Schematics of alignment mark fabrication by standard lithography, evaporation and lift-off process: (a) LOR (brown) and PMMA (blue) resists are deposited on the substrate and exposed to electron beam. (b) Exposed parts of the resists are developed in MIBK and MF319 solutions, respectively. The LOR undercut is controlled by the developing time in MF319. (c) Metal film (yellow) is deposited by E-beam evaporation at ultrahigh vacuum ($<10^{-5}$ Torr). (d) Undeveloped resists are lifted off in PG remover at 55°C for 2~5 hours, leaving the designed metal marks remain on substrate.

To shorten the overall process, we sometimes omit the evaporation and lift-off steps, and directly utilize the developed windows of alignment marks for alignment purposes. The

distance between nearest coarse alignment marks is 300 micrometers and that for fine alignment is 60 micrometers. Sometimes an extra alignment mark grid is added around the flake to maximize accuracy. Finally, the optical image of graphene with alignment marks are imported to Design CAD & NPGS (Nanometer Pattern Generation System) software, and electrodes are designed accordingly. Note that we typically write the pattern on a blank chip for a dosage test, before writing on the wafer with graphene sheet.

III-2.2. Multilevel lithography

The protocol of fabricating dual-gated graphene field effect transistor is based on a multilevel lithography invented and developed by our group members Dr. Gang Liu and Dr. Jairo Velasco Jr. [14,15]. The crucial step is the fabrication of suspended top gates, which is depicted in Fig. 3.5.

With the help of alignment masks defined in previous section, we firstly write the top gate lead and bonding pad via EBL. These exposed features are developed by MIBK and MF319 consequently, as illustrated in Fig. 3.5(a) and (b). To generate a temporary support (that only consists of LOR) for the suspended air-bridge, the upper PMMA resist is removed by hot acetone solution for 10 minutes. The output of the first EBL step is a LOR layer with windows for electrical contacts for the air-bridge (Fig. 3.5(c)).

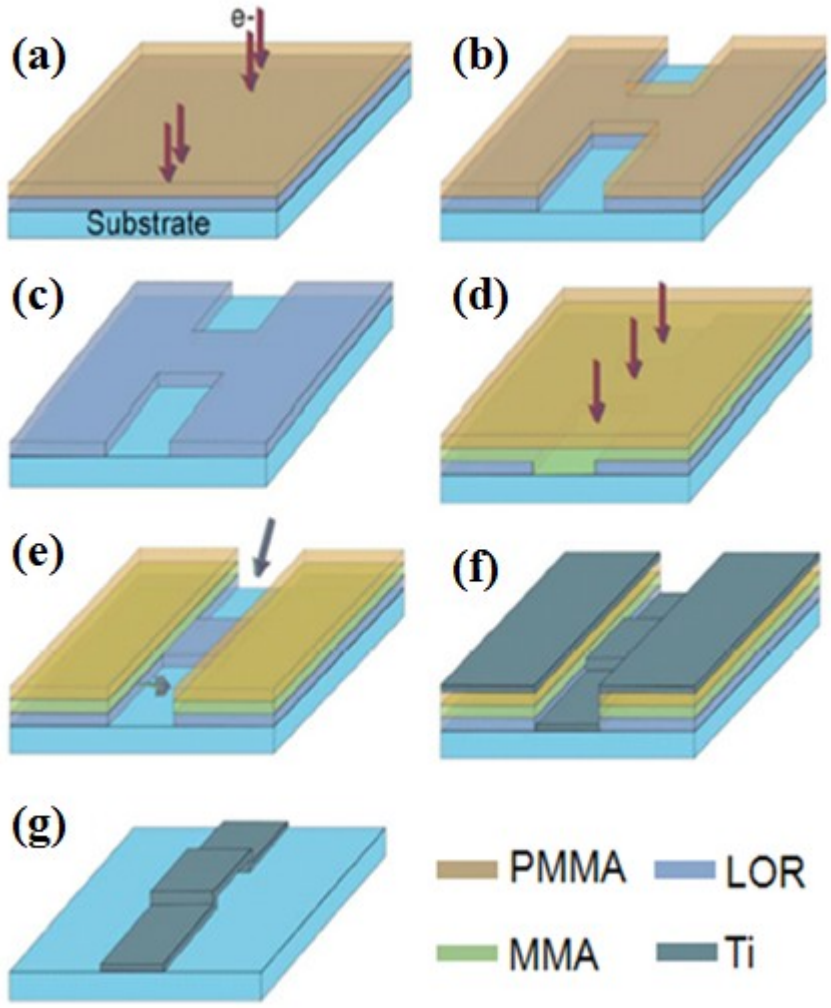

Fig. 3.5 Schematics of multi-lithography process for suspended structure[14]. (a) LOR (light blue) and PMMA (brown) resists are coated on the substrate and exposed to electron beam for the designed gate electrode and bonding pad. (b) Exposed parts are developed in MIBK and MF319 solution respectively. (c) Top PMMA resist is washed away in acetone bath (55 °C, 10 minutes). (d) MMA (green) and PMMA are spun on the top of LOR resist and exposed to electron beam for the designed gate bridge, electrode and bonding pad. (e) Exposed PMMA and MMA are developed in the MIBK solution. (f) Titanium layer (dark blue) is deposited by E-beam evaporation through different incident angles (45 degree, -45 degree indicated by the arrows). (g) All the resists and metal films are lifted off in PG remover solution at 55 °C for 5~8 hours and the air-bridge-like structure with its contacting electrodes and bonding pad is remained. **Reprint with**

permission from G. Liu, J. Velasco, W. Z. Bao, C. N. Lau, Applied Physics Letters 92, 203103 (2008). Copyright (2008) © American Institute of Physics

PMMA/MMA bilayer resists are spun and baked on the top of LOR layer to prepare for the second lithography step, which exposes the whole suspended structure, including air-bridge, electrode and bonding pad. The exposed portions of the resists are removed by developing PMMA and MMA resists in MIBK solution. Therefore, the air-bridge window by MMA/PMMA bilayer and the electrical-contact window by LOR/MMA/PMMA trilayer resists are left on the substrate as shown in Fig. 3.5(e).

The device is completed by a triple-angle evaporation of titanium at 45 degree, -45 degree and 0 degree, with deposition thickness of 100 nm, 100 nm and 150 nm, respectively. These multiple evaporations strengthen the connections between the air-bridge and the electrical leads. Titanium is used as the top gate material due to its excellent mechanical and structural properties: the longest Ti suspended structure we can achieve is 12 μm[15]. Finally, the resists are lifted off in PG remover bath at 55 °C for 5~8 hours, and repeatedly rinsed in IPA solution, leaving a suspended air-bridge (Fig. 3.5(g)). The drying process is carried out in a critical point drier (CPD), so as to minimize the surface tension of the liquids that may damage the suspended structures. Our group also investigates other metal combinations for suspended structure, such as aluminum (Al), chromium (Cr) and gold (Au). The combination of Cr and Au is stable under BOE etch for the fabrication of suspended graphene devices with dual gates[16].

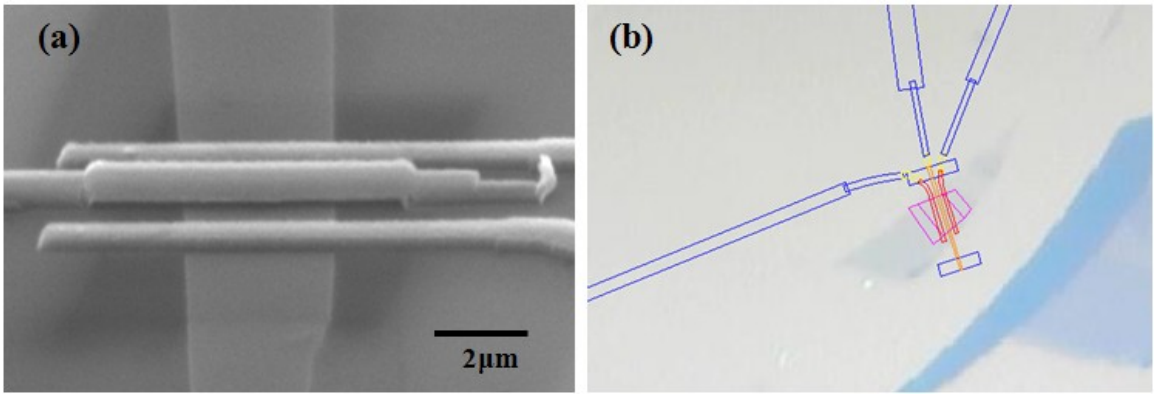

Fig. 3.6 Images of completed device and designed file: (a) SEM image of a typical completed graphene *pnp* device with suspended top gate. Scale bar is 2 μm. (b) Designed pattern for two terminal graphene *pnp* device with suspended top gate. Different colors denote different circuit function and writing dose/order during EBL process.

Fig. 3.6(a) and (b) show the scanning electron microscopy (SEM) image and the design file (.DC2 file by Design CAD) of dual-gated graphene field effect transistor. Lastly, the *pnp* device is completed by another standard EBL process to fabricate source and drain electrodes, which is the last step so as to avoid oxidization of the leads during the lithography processes.

III-3. Device characterization in the probe station

After fabrication, we probe the device's quality at room temperature in our home-built probe station (as shown in Fig. 3.7(a) and (c)). Preliminary characterization includes contact resistance, conductance between different terminals and gate response. The wafer is mounted on a 20 or 16 pin chip carrier (from Spectrum Semiconductor Materials, Fig. 3.7(b)) using silver paint. This electrically conductive glue connects the chip carrier's

ground with device back gate through highly doped silicon body. Then we bond all the electrodes and chip carrier pins with West Bond wire bonder.

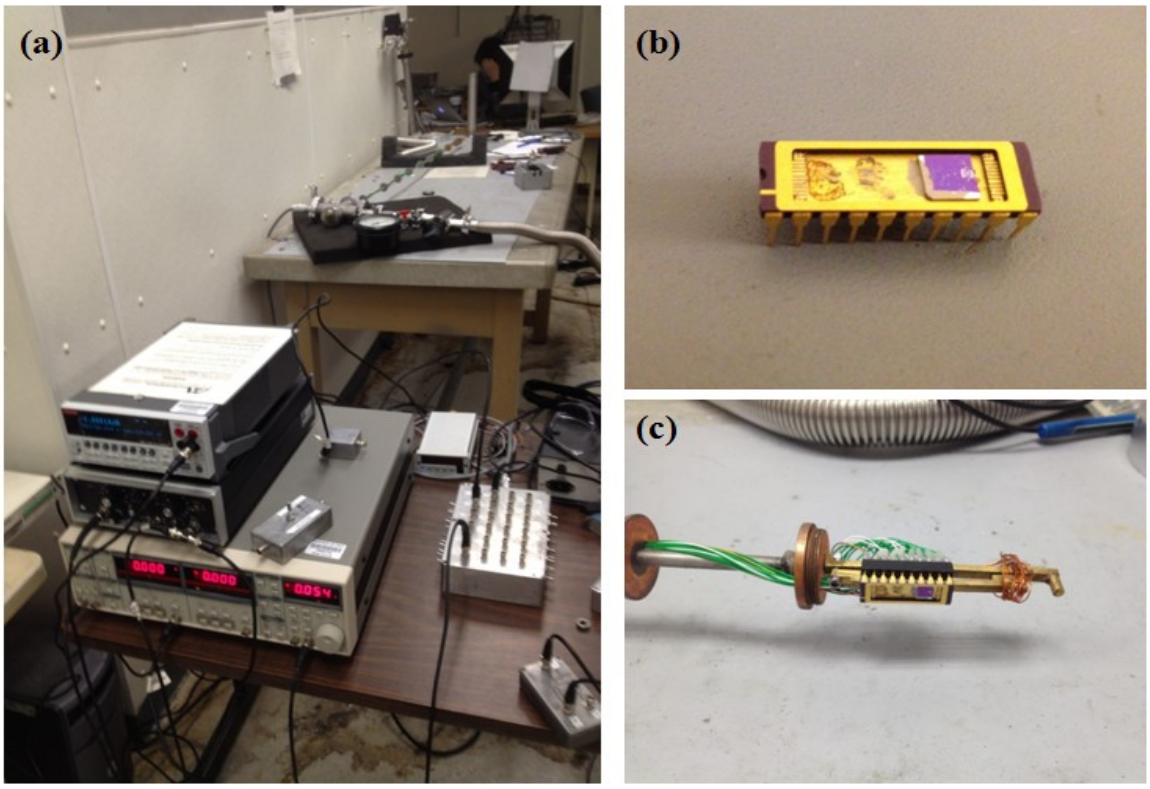

Fig. 3.7. Photos of experiment setup. (a) Home-built probe station. (b) Wire-bonded device on the chip carrier. (c) The loaded socket with the device.

Now the device is ready for characterization in the probe station at room temperature $T \approx 300$ K. We insert the chip carrier into the socket (Fig. 3.7(c)) and pump down the sealed tube to 100 mTorr. The circuit connection is shown in Fig. 3.7(a). Two terminal differentiated conductance ($G=dI/dV$) is measured using standard lock-in techniques, and we use Keithley 2400 voltage source to monitor leakage current through top gate and/or back gate.

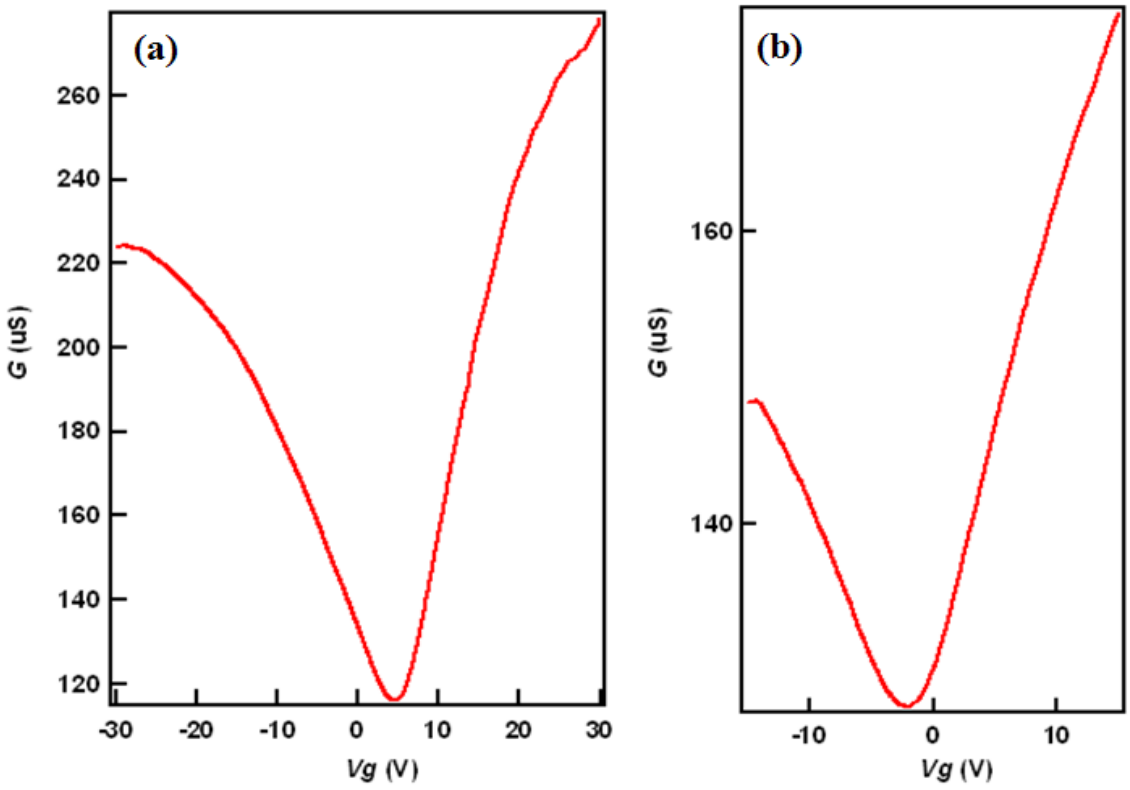

Fig. 3.8 Two terminal conductance as a function of (a) back gate voltage and (b) top gate voltage. The Dirac points are at 4 V and -3 V, respectively.

Fig. 3.8 displays the room temperature back gate response (Fig. 3.8(a)) and top gate response (Fig. 3.8(b)) of a bilayer graphene device with a suspended top gate. The Dirac point or charge neutrality point is around 0 volt gate voltage, demonstrating that this multi-level lithography technique can produce clean and high-quality devices. Although post-annealing by local heater[9] or furnace H_2/Ar[17] gas may improve device quality, my experience indicates that these extra procedures result in 20% lower yield. Hence the post-annealing procedures are not required if the Dirac point is within -30 V~30 V.

References:

1) A. H. Castro Neto, F. Guinea, N.M.R. Peres, K.S. Novoselov, A.K. Geim, *Rev. Mod. Phys*. **81**, 109 (2009)

2) K.S. Novoselov, E. McCann, S.V. Morozov, V.I. Fal'ko, M.I. Katsnelson, U. Zeitler, D. Jiang, F. Schedin, A.K. Geim, *Nature Physics* **2**, 177 (2006)

3) E. McCann, *Phys. Rev. B* **74**, 161403 (2006)

4) E. V. Castro, K. S. Novoselov, S. V. Morozov, N. M. R. Peres, J. Dos Santos, J. Nilsson, F. Guinea, A. K. Geim and A. H. Castro Neto, *Phys. Rev. Lett.* **99**, 216802 (2007)

5) Y. Barlas, R. Cote, J. Lambert, A.H. MacDonald, *Phys. Rev. Lett.* **104**, 096802 (2010)

6) L. Jing, J. Velasco Jr., P. Kratz, G. Liu, W. Bao, M. Bockrath, C. N. Lau, *Nano Lett.***10**, 4000 (2010)

7) W. Bao, Z. Zhao, H. Zhang, G. Liu, P. Kratz, Lei Jing, J. Velasco, Jr., D. Smirnov, C.N. Lau, *Phys. Rev. Lett.* 105, 246601 (2010)

8) K. S. Novoselov, A. K. Geim, S. V. Morozov, D. Jiang, Y. Zhang, S. V. Dubonos, I. V. Grigorieva, A. A. Firsov, *Science* **306**, 666 (2004)

9) J. Velasco, G. Liu, L. Jing, P. Kratz, H. Zhang, W. Bao, M. Bockrath, and C.N. Lau, *Phys. Rev. B*. **81**, 121407(R) (2010)

10) Wenzhong Bao Ph.D thesis, UC Riverside, 2011

11) Adopted from Youtube: http://www.youtube.com/watch?v=rphiCdR68TE, provided by Dr. Ozyilmaz's Group

12) J. B. Oostinga, H.B. Heersche, X. Liu, A.F. Morpurgo, L.M. K. Vandersypen, *Nature Materials* **7**, 151 (2007)

13) A. C. Ferrari, J. C. Meyer, V. Scardaci, C. Casiraghi, M. Lazzeri, F. Mauri, S. Piscanec, D. Jiang, K. S. Novoselov, S. Roth, A. K. Geim, *Phys. Rev. Lett.* **97**, 187401 (2006)

14) G. Liu, J. Velasco, W. Z. Bao, C. N. Lau, *Applied Physics Letters* **92**, 203103 (2008)

15) J. Velasco, G. Liu, W. Z. Bao, C. N. Lau, *New Journal of Physics* **11**, 095008 (2009)

16) J. Velasco, L. Jing, W. Bao, Y. Lee, P. Kratz, V. Aji, M. Bockrath, C. N. Lau, C. Varma, R. Stillwell, D. Smirnov, F. Zhang, J. Jung and A. H. MacDonald, *Nature Nanotechnology* **7**, 156 (2012).

17) W. Bao, G. Liu, Z. Zhao, H. Zhang, D. Yan, A. Deshpande, B.J. LeRoy and C.N. Lau, *Nano Research* **3**, 98 (2010)

Chapter IV. Electrical and magneto-transport of bilayer graphene *pnp* junction with suspended top gate

In this chapter, we perform transport measurements in high quality bilayer graphene *pnp* junctions with suspended top gates. At a magnetic field B=0, we demonstrate band gap opening by an applied perpendicular electric field, with an on/off ratio up to 20,000 at 260 mK. Within the band gap, the conductance decreases exponentially by 3 orders of magnitude with increasing electric field, and can be accounted for by variable range hopping with a gate-tunable density of states, effective mass, and localization length. At large B, we observe quantum Hall conductance with fractional values, which arise from equilibration of edge states between differentially-doped regions, and the presence of an insulating state at filling factor υ=0. Our work underscores the importance of bilayer graphene for both fundamental interest and technological applications

IV-1. Electrical transport at low temperature (T=260 mK)

Bilayer graphene (BLG) is a unique two-dimensional (2D) system with an unusual band structure -- parabolic bands with the conduction and valence bands touching at a point[1-3]. Consequently, its charge carriers behave as massive Dirac fermions, and are described by a combination of the Schrödinger and Dirac equations. This unique band structure gives rise to a number of novel properties, such as a gate tunable band gap[2], excitonic condensation[4, 5], and potentially novel integer and fractional quantum Hall (QH) states[6, 7,

[8]. On the technological front, band gap opening in bilayer graphene[2, 9, 10, 11-14] in an applied electric field has generated significant interest as a promising route to band gap engineering and control in graphene electronics.

Here we discuss the experimental investigation of dual-gated bilayer graphene junctions, which have mobility up to 10,000 cm^2/Vs, in zero and high magnetic fields. Using a combination of a Si back gate and a suspended top gate, these dual-gated structures offer *in situ* control of the dopant density n and type of different regions, as well as independent tuning of n_2 and applied electric field E_2 for the region under the top gate. As E_2 is increased from 0 to 0.93 V/nm, the device conductance at charge neutrality point decreases exponentially by over 3 orders of magnitude, reaching an on/off ratio of 20,000, that is more than 10 times higher than the previously reported values[12, 13]. The data can be satisfactorily accounted for by variable range hopping (VRH) in 2D, suggesting the opening of an electric field induced band gap which enables the localization length, effective mass, and density of states to be tuned. In a high magnetic field B, we observe fractional-valued QH plateaus, which arise from edge state equilibration at the interface of differentially doped regions, in agreement with theoretical predictions[15, 16]. Notably, an insulating state develops at filling factor $\upsilon=0$, whose conductance are exponentially dependent on applied B. Thus, our work suggests that competing symmetries and insulating states in bilayer graphene can be tuned by electric and magnetic fields, which are of significant interest for both technological applications and fundamental understanding of 2D systems.

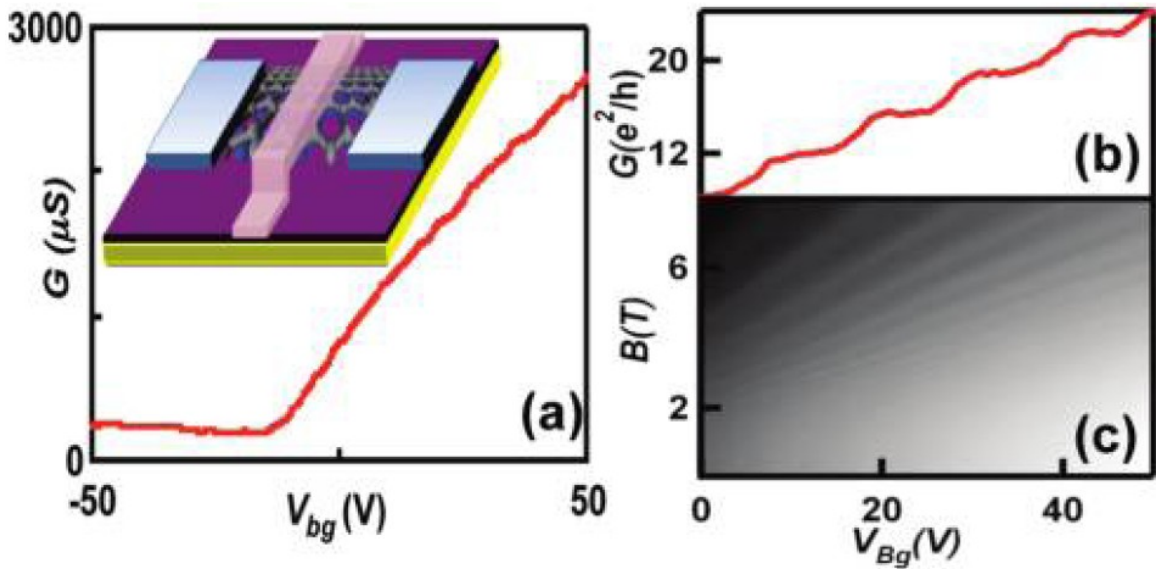

Fig. 4.1 Device schematics and characterization: (a) $G(V_{bg})$ for a bilayer graphene device at T=260 mK and B=0. Inset: Device schematic. (b) $G(V_{bg})$ of the device at B=8 T. (c) LL fan diagram $G(V_{bg}, B)$ of the device.

BLG sheets are exfoliated from bulk graphene onto Si/SiO_2 wafers cleaned with a H_2SO_4/H_2O_2 solution mixture. The Ti/Al electrodes and Ti suspended top gates[17, 18] are fabricated by electron beam lithography, as described in chapter III. A device schematic is shown in Fig. 4.1(a) inset. Unless specified otherwise, the devices are measured at 260 mK in a He^3 refrigerator using standard lock in techniques. Here we focus on data from a single device with width W=1.2 μm, and source-drain separation L= 2.3 μm. The top gate, straddling the center of the device, is 550 nm long and suspended at d~50 nm above the substrate.

We first examine the device behavior as a function of back gate voltage V_{bg}. Fig. 4.1(a) plots the differential conductance G of the device versus V_{bg} at B=0, with the Fermi level turned to the Dirac point at $V_{bg}^0 \approx$-18 V. The electron mobility is ~10,000 cm^2/Vs, while the hole mobility is significantly lower. Thus in the rest of this chapter we will focus on the electron-doped regime. The device conductance in units of e^2/h at B=8 T is shown in Fig. 4.1(b). Theoretically, in a high magnetic field B, we expect the device's Hall conductance to be quantized at[1, 3, 10]

$$\sigma_{xy} = 4\upsilon\frac{e^2}{h}, \upsilon = -3, -2, -1, 1, 2, 3 \qquad (4.1)$$

, where $\upsilon=(nh)/(Be)$ is the filling factor, e is the electron charge, h is Planck's constant, n is the charge density, and $v_F \sim 10^6$ m/s is the Fermi velocity of the charges. The omission of the υ=0 state arises from the degeneracy of the zeroth and first Landau levels (LL) and the resultant eight-fold degeneracy at zero energy. In Fig. 4.1(b), clear plateaus that are quantized at G=8, 12, 16… e^2/h are observed, in agreement with equation (4.1). Fig. 4.1(c) shows the standard LL "fan diagram", *i.e.* the evolution of the conductance plateaus with B and V_{bg}. Impressively, a total of 15 plateaus are visible for B>2 T, demonstrating the high quality of this device. Furthermore, since the trajectory of the center of a plateau has a slope $\upsilon e/h\alpha_{bg}$ in the V_{bg}-B plane, where $\alpha_{bg}=n/V_{bg}$ is the back gate coupling efficiency, we extract $\alpha_{bg} \approx 7.4\text{x}10^{10}$ cm^{-2}V^{-1} from Fig. 4.1(b).

By applying voltages to both top and back gates, we can create *pnp* junctions with *in situ* modulation of junction polarity and dopant levels. Fig. 4.2(a) shows the conductance plot of G (color) *vs.* V_{bg} (vertical axis) and V_{tg} (horizontal axis) at B=0. The plot can be

partitioned into 4 regions with different combinations of dopant types, with the Dirac points occurring at (V_{tg}^0, V_{bg}^0)=(-2.6 V, -18 V). In particular, the blue diagonal features correspond to the conductance of the region that is controlled by both V_{tg} and V_{bg}, *i.e.*, the area under the top gate. From the slope of the diagonal features near the Dirac points, which corresponds to the ratio of the coupling efficiencies between the top gate and the back gate, we extract the top gate coupling efficiency $\alpha_{tg}\approx 1.2\text{x}10^{11}$ $\text{cm}^{-2}\text{V}^{-1}$. At high V_{tg} and V_{bg} values, the dark blue regions exhibit noticeable curvature, which arises from the deflection of the top gate under the electrostatic pressure.

This *in situ* creation of *pnp* or *npn* junctions in double gated junctions has been extensively studied in single layer graphene (SLG) devices[16, 17, 19-23], and enabled the observation of phenomena such as Klein tunneling[24-26], equilibration of counter-propagating edge modes[16, 17, 20, 21], and conductance fluctuations induced by charge localization in the quantum Hall regime[21]. For BLG, a unique aspect is the possibility for independent control of the charge density n_2 and the electric field E_2 applied across the bilayer[2, 9 11-14, 27]. Here the subscript 2 denotes the top-gated region. Quantitatively, V_{bg} induces an electric field below graphene $E_b=\varepsilon_{SiO}(V_{bg}- V_{tg}^0)/t$, where $\varepsilon_{SiO}\approx 3.9$ and t=300 nm are the dielectric constant and thickness of the SiO_2 layer, respectively. Similarly, V_{tg} induces $E_t=-(V_{tg}-V_{tg}^0)/d$ above graphene. The difference of the fields yields the total charge density under the top gate, $n_2=(E_b-E_t)e$, whereas their average $E_2=(E_b+E_t)/2$ breaks the inversion symmetry and yields a potential difference $V_2= E_2$ (3.3 Å) across the bilayer. For the data shown in Fig. 4.2(a), E_2 ranges from 0 to 0.96 V/nm.

To better explore this unique aspect of BLG, we replot part of the data shown in Fig. 4.2(a) in terms of n_2 (horizontal axis) and E_2 (vertical axis), as shown in Fig. 4.2(b) (note the logarithmic color scale that spans 6 orders of magnitude). To account for the deflection of the top gate under applied voltages, we self-consistently solve for the deflection and E_t by considering the electrostatically induced bending of a beam, which adopts a parabolic profile and in turn modifies the electrostatic pressure. As demonstrated by Fig. 4.2(b), this procedure successfully accounts for much of the curvature in Fig. 4.2(a).

A striking feature in Fig. 4.2(b) is the vertical dark brown band at n_2~0, which, with increasing E_2, develops into a triangular green region. This indicates a very low conductance state at high electric field and charge neutrality point. Fig. 4.2(c) plots several line traces $G(n_2)$ at different E_2 values ranging from 0.21 to 0.73 V/nm. Each curve displays a minimum at $n_2 \approx 0$. For small values of E_2, the minimum is rather shallow, and the device's on/off ratio η, defined as the ratio between the maximum and minimum conductance values at a given E_2, is about 10. As E_2 increases, the device conductance at $n_2 \approx 0$ decreases dramatically, while that for large n_2 remains almost constant, resulting in a rapidly increasing η. For E_2=0.73 V/nm, η>20,000.

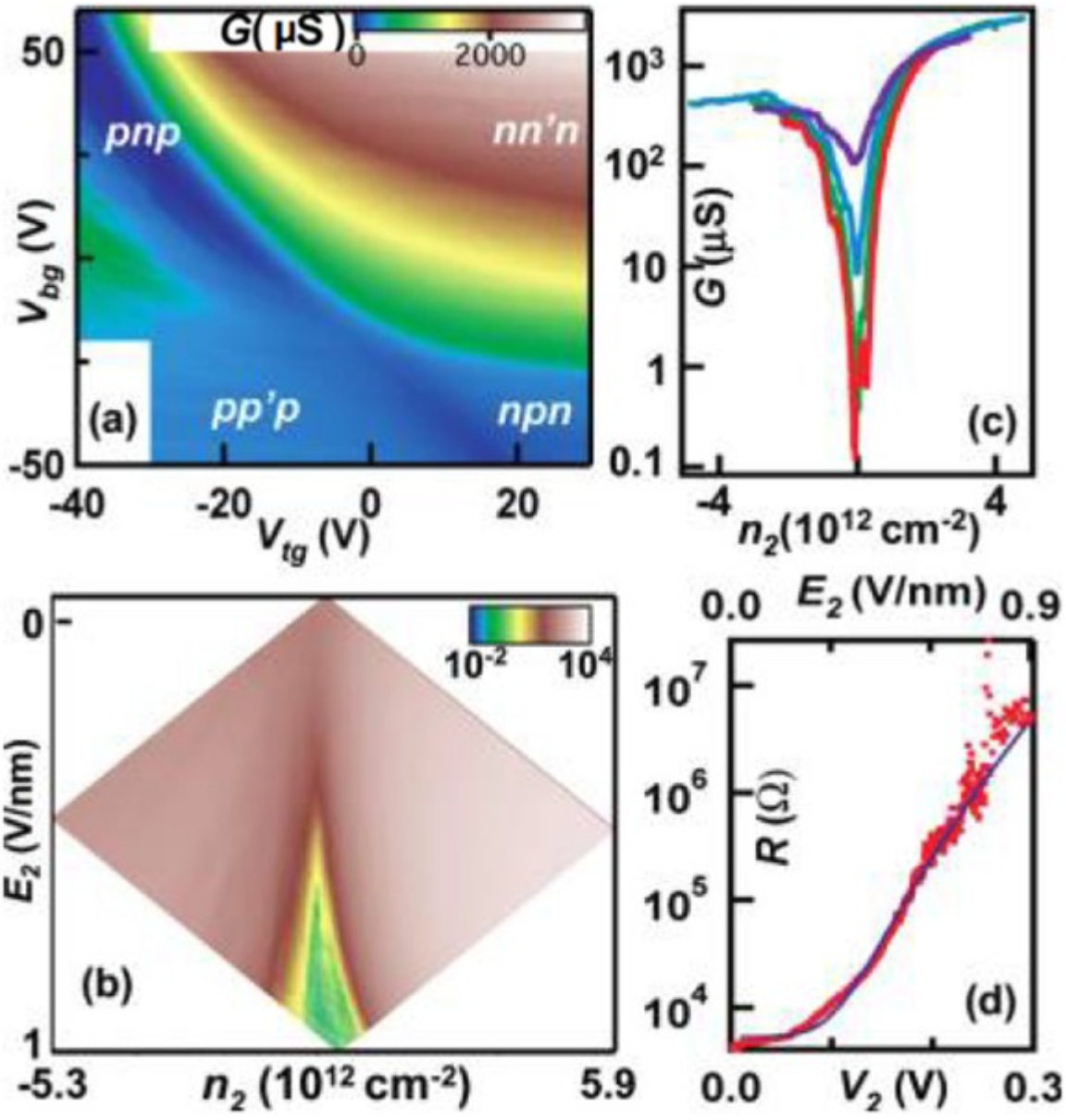

Fig. 4.2 BLG *pnp* electrical transport at *B*=0 T. (a) $G(V_{bg}, V_{tg})$ of the device at B=0. The junction polarities are indicated on the graph. (b) Data in (a) plotted in terms of E_2 and n_2. Note the logarithmic color scale. (c) (Top to bottom) Line traces $G(n_2)$ at E_2=0.21, 0.49, 0.65 and 0.73 V/nm. (d) $R(E_2)$ at n_2=0. The line is a fit of the data to the VRH model,

$$R = R_0 + A\exp\left[-\left(\frac{4\pi e}{k_B} a V_2\right)^{1/3}\right]$$, where R_0, a and A are fitting parameters.

Fig. 4.2(d) plots the device resistance $R=1/G$ at n_2=0 *vs.* E_2 (top axis) and V_2 (bottom axis); the exponential increase in R with increasing V_2 over nearly 3 decade suggests a field-induced opening of a band gap in the top gated region. In the simplest picture, transport could occur via thermally activated carriers. From tight binding calculations[2, 3, 9, 10], BLG's band structure adopts a "Mexican-hat" shape under an applied potential V_2, with a dispersion relation

$$E^{\pm-} \approx \pm\frac{eV_2}{2} \mp \frac{eV v_F^{2} k}{t_\perp} - \frac{v_F \hbar k}{t_\perp^{2} eV_2} \qquad (4.2)$$

, which is valid for $v_F \hbar k = V = t_\perp$, and a band gap

$$\Delta = \frac{t_\perp eV_2}{\sqrt{t_\perp^{2} + eV_2^{2}}} \qquad (4.3)$$

Here $t_\perp$ ~ 0.2-0.4 eV is the inter-layer hopping energy, and k is the electron wave vector. From equation (4. 3), Δ scales almost linearly with V_2 until it saturates at $t_\perp$; if screening is taken into account, it can be reduced by a factor of 2. In our devices, Δ ~ 0-0.1 eV[14]. If electrons are thermally activated to traverse the gapped region, we expect $R \sim exp(-eV_2/k_BT)$, with an exponent $b \sim e/2k_BT \sim 19000$, where k_B is Boltzmann's constant and T=0.3 K. However, from Fig. 4.2, the slope of the semi-log plot is ~36, or 2-3 orders of magnitude smaller than expected. This suggests that transport is across the top gated region is not thermally activated. Indeed, we observe little temperature dependence of conductance for T<1 K.

Another transport mechanism is variable range hopping (VRH)[28], in which charge carriers are thermally activated to hop between localized states. For VRH in 2D, one expects $G \sim exp\ [-(T_0/T)^{1/3}]$ where $k_B T_0 = 4a\kappa^2/\rho_0$, a is a dimensionless constant of order unity, κ the coefficient of the exponential decay of the localized state, and ρ_0 is the density of states at the Fermi level[28]. Using the WKB approximation, we expect $\kappa \sim \sqrt{2m^* V_2}/\hbar$, where m^* is the effective mass of charge carriers. From equation (4.2), $\rho_0 = \frac{2k}{\pi}\frac{\partial k}{\partial E}$ and $m^* = \hbar^2 / \frac{\partial^2 E}{\partial k^2}$, and ignoring the quadratic term in $v_F \hbar$, we obtain $k_B T_0 \approx 4\pi a e V_2$.

To see if VRH can quantitatively account for the data, we fit the data in Fig. 4.2(d) to the expression $R = R_0 + A \exp\left[-\left(\frac{4\pi e}{k_B} a V_2\right)^{1/3}\right]$, where R_0 is the series resistance to account for the resistance of the non-top-gated region. Here we use $T_0/T = T_0$ because of our data's temperature independence below 1K. Satisfactory fit can be obtained by using the parameters R_0=5.3 kΩ, A=1.85x10^{-4} Ω, and a=0.32, in agreement with the expectation that a is a constant of order unity. This excellent agreement between VRH model and our data strongly suggests a successful band gap opening in BLG, and transport via variable range hopping between localized states that either lie within the gap[29-32] or are formed from disorder-induced charge puddles[33, 34].

IV-2. Magneto transport at low temperature (*T*=260 mK)

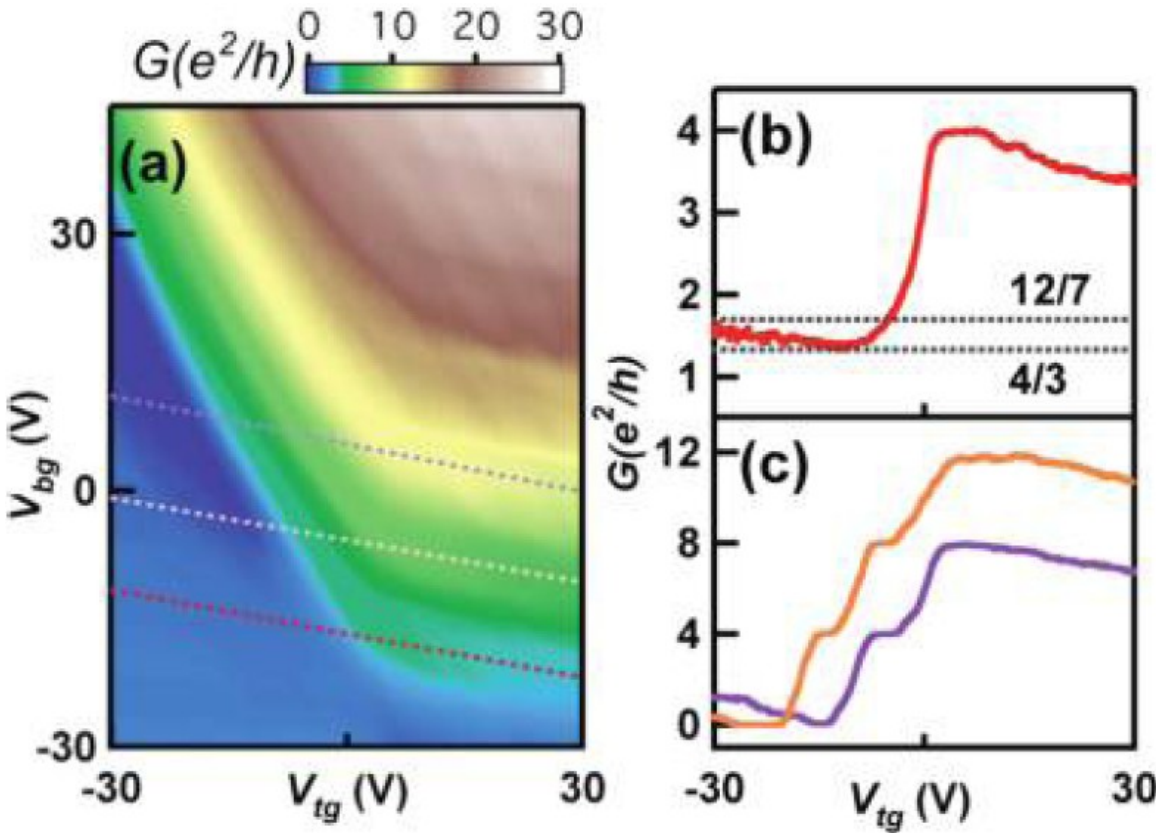

Fig. 4.3 BLG pnp map at high magnetic field *B*=8 T. (a) $G(V_{bg}, V_{tg})$ of the device at B=8 T. (b) Line trace at ν_i=4, *i.e.,* along the red dotted line in (a). (c) Line traces $G(V_{tg})$ at ν_i=8 (yellow) and ν_i=12 (purple).

We now focus on the device behavior in high magnetic fields. In the QH regime, the non-uniform charge density gives rise to regions of different filling factors, and, for bi-polar (i.e. *pnp* or *npn*) junctions, counter-propagating edge states. Consequently, the device conductance exhibits plateaus at fractional values of e^2/h that arise from the mixing of edge states at the interfaces. For SLG, assuming full edge stage equilibration, the device

conductance has been theoretically[16] and experimentally[16-18, 21] shown to obey the following formula,

$$G=e^2/h|\nu_2| \qquad \text{if } \nu_1\nu_2>0 \text{ and } |\nu_1|\geq|\nu_2| \qquad (4.4a)$$

$$G=\frac{e^2}{h}\left(\frac{1}{|\nu_1|}\mp\frac{1}{|\nu_2|}\right)^{-1} \quad \begin{cases}-: \text{ if } \nu_1\nu_2>0 \text{ and } |\nu_2|>|\nu_1| \\ +: \text{if } \nu_1\nu_2<0\end{cases} \qquad (4.4b)$$

where ν_1, ν_2=..-6, -2, 2, 6, … are the filling factors in the areas outside and within the top-gated regions, respectively. For BLG, one expects these simple relations continue to hold, with ν_1, ν_2=…-8, -4, 4, 8… instead, yet they have never been experimentally verified.

Fig. 4.3(a) displays a typical data set $G(V_{tg}, V_{bg})$ measured at B=8 T. The conductance map appears as a plaque of adjoined parallelograms, corresponding to different ν_1 and ν_2 combinations, similar to that observed in SLG devices. Fig. 4.3(b) plots a line trace $G(V_{tg})$ in units of e^2/h at constant ν_1=4. As V_{tg} increases from -30 or ν_2=~-15, G decreases from 1.6, reaching a minimum of 1.35 at ν_2=-4, then increases to a maximum plateau of 4 at ν_2=4, before decreasing again. From equation (4.1), the conductance values are predicted to be 12/7, 8/5, 4/3 and 4, for ν_2=-12, -8, -4 and 4, respectively, in good agreement with the data. Similarly, line traces at ν_1=*8* and 12 are shown in Fig. 4.2(c), with conductance values reasonably accounted for by equation (4.4). We emphasize that this is the first time that the edge state equilibration is observed in bilayer *pnp* junctions, again underscoring the high quality of our junctions.

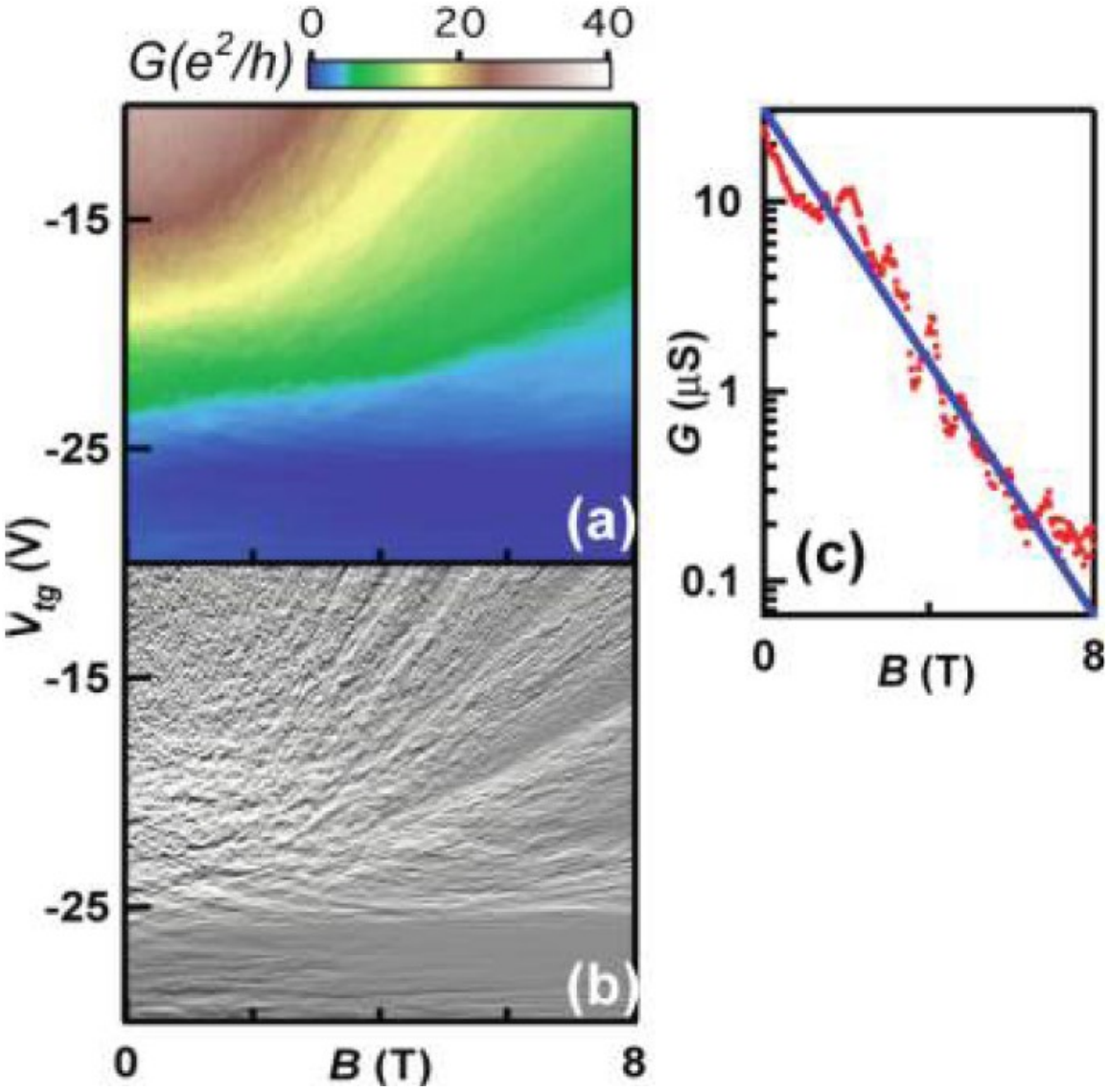

Fig. 4.4 *B*-field induced insulating state. (a) $G(V_{tg}, B)$ at V_{bg}=19 V. (b) Data in (a) differentiated with respect to V_{tg}. (c) Line trace $G(B)$ taken at V_{bg}=19 V and V_{tg}=-27 V. The blue line is a fit to an exponential function.

There is, however, one important discrepancy between equation (4.4) and our data. In Fig. 4.4(c), G reaches a minimum of $<10^{-7}$ S, or an insulating state, which cannot be obtained from (4) using ν_1, ν_2=…-8, -4, 4, 8…. This zero conductance state corresponds to ν_2=0,

indicating opening of a band gap in the top gated region and lifting of the orbital LL degeneracy. To investigate this insulating state further, we measure the device conductance as a function of V_{tg} and B, at fixed V_{bg}=19 V, as shown in Fig. 4.4(a). Significant fluctuations are visible, with same slopes in the V_{tg} –B plane as those of the adjacent plateaus (Fig. 4.4(d)). These fluctuations arise from charging and localization from quantum dots in the bulk of the device, which consist of compressible regions that are surrounded by incompressible regions[21, 35]. Notably, fluctuations with zero slope have been observed, again indicating the presence of the ν_2=0 state, which is not observed for monolayer graphene devices on substrate. These fluctuations also suggest significant spatial variations in density (up to $\pm\nu$) in the BLG sheet, hence confirming the presence of electron and hole puddles near the charge neutrality point, which could give rise to localized states, as discussed above.

We now focus on the insulating ν_2=0 state. Fig. 4.4(b) plots *R(B)* at V_{tg}=-27 V and V_{bg}=19 V, or equivalently, n_2=10^{11} cm^{-2} and E=0.24 V/nm. At B=0, G~25 μS; with increasing *B, G* decreases exponentially with an exponent $c\approx$0.70, reaching 0.12 μS at B=8 T. Such exponential dependence of G on B has been observed in suspended bilayer devices[36], though with a much larger exponent, presumably because of the very low disorder of suspended devices.

IV-3. Discussion

Thus far we have observed two different insulating states in BLG. The first is induced by an external electric field at B=0, and the conductance decreases exponentially with E_2. The second insulating state occurs at finite electric *and* magnetic fields, and the conductance decreases exponentially with B. These two insulating states arise from the competition between the E and B, which has been a topic of recent theoretical interest[6]. In principle, a transition between a layer polarized insulator and a QH ferromagnet insulator is expected to be observable in low-disorder devices, with a slope $E/B \sim 10^7$ V/m/T. In our current device, any such transition is smeared by the relatively large number of disorder-induced impurity states.

Recently, our group had successfully fabricated suspended BLG devices with dual gates[37]. We resolve an intrinsic energy gap of BLG at the charge neutrality point (CNP) using source-drain bias as a spectroscopic tool[37]. It was one of the first experiments[38~41] to contribute towards understanding the rich interaction-driven physics in bilayer graphene.

In conclusion, using bilayer graphene *pnp* junctions, we have demonstrated equilibration of QH edge states, insulating states induced by electric and/or magnetic fields, and transport via VRH in the gapped regime. In the future, experimental investigations of BLG with double gates promise to yield a wealth of novel phenomena.

References:

1) A. H. Castro Neto, F. Guinea, N.M.R. Peres, K.S. Novoselov, A.K. Geim, *Rev. Mod. Phys.* **81**, 109 (2009)

2) E. McCann, *Phys. Rev. B* **74**, 161403R (2006)

3) K. S. Novoselov, E. McCann, S. V. Morozov, V. I. Fal'ko, M. I. Katsnelson, U. Zeitler, D. Jiang, F. Schedin, A. K. Geim, *Nature Phys.* **2 (3)**, 177-180 (2006)

4) C. H. Park, S. G. Louie, *Nano Lett.* **10 (2)**, 426-431 (2010)

5) Y. Barlas, R. Cote, J. Lambert, A. H. MacDonald, *Phys. Rev. Lett.* **104 (9)**, 096802 (2010)

6) R. Nandkishore, L. Levitov, *preprint* **2010**, arXiv:1002.1966v1.

7) N. Shibata, K. Nomura, *J. of the Physical Society of Japan* **78 (10)**, 104708 (2009)

8) W. Bao, Z. Zhao, H. Zhang, G. Liu, P. Kratz, L. Jing, J. Velasco Jr., D. Smirnov, C. N. Lau, *Phys. Rev. Lett.* **105**, 246601 (2010)

9) E. V. Castro, K. S. Novoselov, S. V. Morozov, N. M. R. Peres, J. Dos Santos, J. Nilsson, F. Guinea, A. K. Geim and A. H. Castro Neto, *Phys. Rev. Lett.* **99**, 216802 (2007)

10) E. McCann, V. I. Fal'ko, *Phys. Rev. Lett.* **96 (8)**, 086805 (2006)

11) J. B. Oostinga, H.B. Heersche, X. Liu, A.F. Morpurgo, L.M. K. Vandersypen, *Nature Materials* **7**, 151 (2007)

12) F. N. Xia, D. B. Farmer, Y. M. Lin, P. Avouris, *Nano Lett.* **10 (2)**, 715-718 (2010)

13) B. N. Szafranek, D. Schall, M. Otto, D. Neumaier, H. Kurz, *Appl. Phys. Lett.* **96 (11)**, 112103 (2007)

14) Y. B. Zhang, T. T. Tang, C. Girit, Z. Hao, M. C. Martin, A. Zettl, M. F. Crommie, Y. R. Shen, F. Wang, *Nature* **459**, 820 (2009)

15) D. A. Abanin, L. S. Levitov, L. S. *Science* **317**, 641-643 (2007)

16) B. Ozyilmaz, P. Jarillo-Herrero, D. Efetov, D. A. Abanin, L. S. Levitov, P. Kim, *Phys. Rev. Lett.* **99**, 166804 (2007)

17) G. Liu, J. Velasco, W. Z. Bao, C. N. Lau, *Applied Physics Letters* **92**, 203103 (2008)

18) J. Velasco, G. Liu, W. Z. Bao, C. N. Lau, *New Journal of Physics* **11**, 095008 (2009)

19) V. V. Cheianov, V. I. Fal'ko, V. I. *Phys. Rev. B* **74**, 041403 (2006)

20) J. R. Williams, L. DiCarlo, C. M. Marcus, *Science* **317**, 638 (2007)

21) J. Velasco, G. Liu, L. Jing, P. Kratz, H. Zhang, W. Z. Bao, M. Bockrath, C. N. Lau, *Phys. Rev. B* **81**, R121407 (2010)

22) B. Huard, J. A. Sulpizio, N. Stander, K. Todd, B. Yang, D. Goldhaber-Gordon, *Phys. Rev. Lett.* **98**, 236803 (2007)

23) R. V. Gorbachev, A. S. Mayorov, A. K. Savchenko, D. W. Horsell, F. Guinea, *Nano Letters* **8 (7)**, 1995 (2008)

24) M. I. Katsnelson, K. S. Novoselov and A. K. Geim, *Nature Physics* **2 (9)**, 620-625 (2006)

25) N. Stander, B. Huard, D. Goldhaber- Gordon, *Phys. Rev. Lett.* **102**, 026807 (2009)

26) A. F. Young, P. Kim, *Nature Phys.* **2009,** 5, (3), 222-226.

27) Kim, S.; Tutuc, E. *preprint* **2009,** arXiv:0909.2288v1.

28) V. Ambegaokar, B. I. Halperin, J. S. Langer, *Physical Review B* **4 (8)**, 2612 (1971)

29) T.O. Wehling, A.V. Balatsky, A.M. Tsvelik, M.I. Katnelson, A.I. Lichtenstein, *Europhys. Lett.* **84**, 17003 (2008)

30) M.I. Katsnelson, M.F. Prokhorova, *Phys. Rev. B* **77**, 205424 (2008)

31) F. Guinea, M.I. Katsnelson, M.A.H. Vozmediano, *Phys. Rev. B* **77**, 075422 (2008)

32) Nilsson, J.; Castro, A. H. *Phys. Rev. Lett.* **98**, 126801 (2007)

33) J. Martin, N. Akerman, G. Ulbricht, T. Lohmann, J.H. Smet, K.v. Klitzing, A. Yacoby, *Nature Phys.***4**, 144 (2008)

34) A. Deshpande, W. Bao, F. Miao, C.N. Lau, B.J. LeRoy, *Phys. Rev. B* **79**, 205411 (2009)

35) S. Branchaud, A. Kam, P. Zawadzki, F.M. Peeters, A.S. Sachrajda, *Phys. Rev. B*, **81**, R121406 (2010)

36) B. E. Feldman, J. Martin, A. Yacoby, *Nature Physics* **5 (12)**, 889 (2009)

37) J. Velasco, L. Jing, W. Bao, Y. Lee, P. Kratz, V. Aji, M. Bockrath, C. N. Lau, C. Varma, R. Stillwell, D. Smirnov, F. Zhang, J. Jung and A. H. MacDonald, *Nature Nanotechnology* **7**, 156 (2012)

38) J. Martin, B.E. Feldman, R.T. Weitz, M.T. Allen, A. Yacoby, *Phys. Rev. Lett.* **105**, 256806 (2010)

39) R.T. Weitz, M. T. Allen, B.E. Feldman, J. Martin, A. Yacoby, *Science* **330**, 812–816 (2010)

40) W. Bao, L. Jing, J. Velasco Jr., Y. Lee, G. Liu, D. Tran, B. Standley, M. Aykol, S. B. Cronin, D. Smirnov, M. Koshino, E. McCann, M. Bockrath, and C.N. Lau, *Nature Phys.* **7**, 948–952 (2011)

41) A. S. Mayorov, D. C. Elias, M. Mucha-Kruczynski, R. V. Gorbachev, T. Tudorovskiy, A. Zhukov, S. V. Morozov, M. I. Katsnelson, V. I. Fal'ko, A. K. Geim, K. S. Novoselov, *Science* **333**, 860–863 (2011)

Chapter V. Detection of supercurrent in Topological Insulator Josephson Junctions

Recently, topological insulators have become a popular material in the field of experimental condensed matter physics[1, 2]. The thin film samples are prepared using the similar exfoliation method as the one for graphene[3, 4, 5]. In this chapter, I will focus on our characterization of the transport of Bi_2Se_3 with calcium doping material. We investigate the electronic transport in topological insulator thin films coupled with superconducting leads. In these novel Josephson transistors, we observe different characteristic features and strong reduction of the critical current I_c from the theoretical value.

V-1. Introduction

Topological insulators (TIs) are a distinctive class of materials that have metallic surface states but insulating bulk states. Examples of TIs include 2-dimensional (2D) HgTe/CdTe quantum wells[6] and 3D crystals such as Bi_2Se_3 and Bi_2Te_3[7~12]. In these materials, large spin-orbit coupling results in inverted band structures (*i.e. p*-like character in the conduction band and *s*-like character in the valence band). The crossing of these inverted bands at an interface with a topologically trivial insulator results in surface carriers that are massless Dirac particles, similar to those in graphene. Unlike graphene that has 4 Dirac cones arising from the spin and sub-lattice degeneracies, TIs only have 1 Dirac cone. Surface conduction in TIs is characterized by chiral, spin-polarized counter-

propagating states. Backscattering between these channels is forbidden, resulting in topologically protected ballistic transport.

3D TIs have become a fascinating platform for realizing many phenomena that previously only exist in theoretical predictions, such as magnetic monopoles, magneto-electric effect[13], Majorana particles[14, 15], fractional charges above magnetic domain walls[16], *etc*. In particular, one intriguing prediction is that the interface between a topological insulator and superconductor can support Majorana fermions[9, 10]. A Majorana fermion is a fermion that is its own antiparticle. It was predicted by Majorana in 1937, but never conclusively observed in particle physics. In condensed matter systems, it was speculated to be related to the Moore-Read state in the n=5/2 quantum Hall state[28]. Since a pair of spatially-separated Majorana fermions constitutes a degenerate 2-level quantum system, *i.e.* a qubit, they are considered promising candidates for fault-tolerant quantum computing.

Majorana fermion states are predicted to exist at a superconductor/TIs interface, due to the superconducting proximity effect. The peculiarities of Cooper pairs in TIs lie in the broken spin symmetry and the Berry phase of π on the TIs surface. Thus the first step to observe Majorana fermions is to couple TIs to superconducting electrodes, so as to form a Josephson junction. To this end, we couple superconducting electrodes to Bi_2Se_3 thin films that are characterized by Raman and EDS spectroscopy, and observe small

supercurrent in these Josephson junction. Our results represent a step towards the realization of Majorana fermions in solid state systems.

V-2. Materials preparation and characterization

Bi_2Se_3 single crystals are synthesized by multistep heating processes, and doped by Ca to reduce the Se vacancies[17, 18]. The growing procedure starts from sealing high purity of raw materials (99.999% Bi_2Se_3 and 99.98% Ca from Alfa Aesar) in a vacuum quartz tube. Then the tube is heated at 800 ˚C in Fisher Scientific thermal furnace for 24 hours to melt all the materials uniformly. During the cooling process, the sealed quartz tube is first cooled to 500 ˚C and maintained at this temperature for 72 hours, then allowed to cool to room temperature naturally.

Bi_2Se_3 and similar 3D TIs materials (Bi_2Te_3, Sb_2Te_3, *etc*) are binary chalcogenide compound crystal with rhombohedral structure[1] at ambient environment, which is $D_{3d}^5(R\bar{3}m)$ with five atoms in the trigonal unit cell. Fig. 5.1 inset displays the schematics of its structure, which consists of 5-layer stacks known as quintuples, and a calcium atom substitutes for a bismuth vacancy. Each quintuple layer consists of five atomic planes vertically arranged in the sequence of …Se-Bi-Se-Bi-Se…, and its crystal parameters of the hexagonal unit cell are a=0.413 nm and c=2.864 nm[19]. Calcium atoms work as p-type dopant, as they replace Bi atoms (as shown in Fig. 5.1 inset) and introduce more holes. Since adjacent quintuple layers are bounded by weak van der Waal's forces, mechanical

exfoliation can be used to obtain thin films down to multiple quintuple layer (~10 nm in thickness)[20].

Using Ca-doped bulk Bi_2Se_3 crystals, we exfoliate thin films with thickness ranging from 50 to 120 nm onto Si/SiO_2 substrates, and perform energy-dispersive x-ray spectroscopy (EDS, Joel SEM) to determine their chemical stoichiometry[21], as shown in Fig. 5.1 and table 5.1. Fig. 5.1 displays the emitted excitation spectrum of atoms in the sample interacting with X-ray as a function of incident X-ray energy.

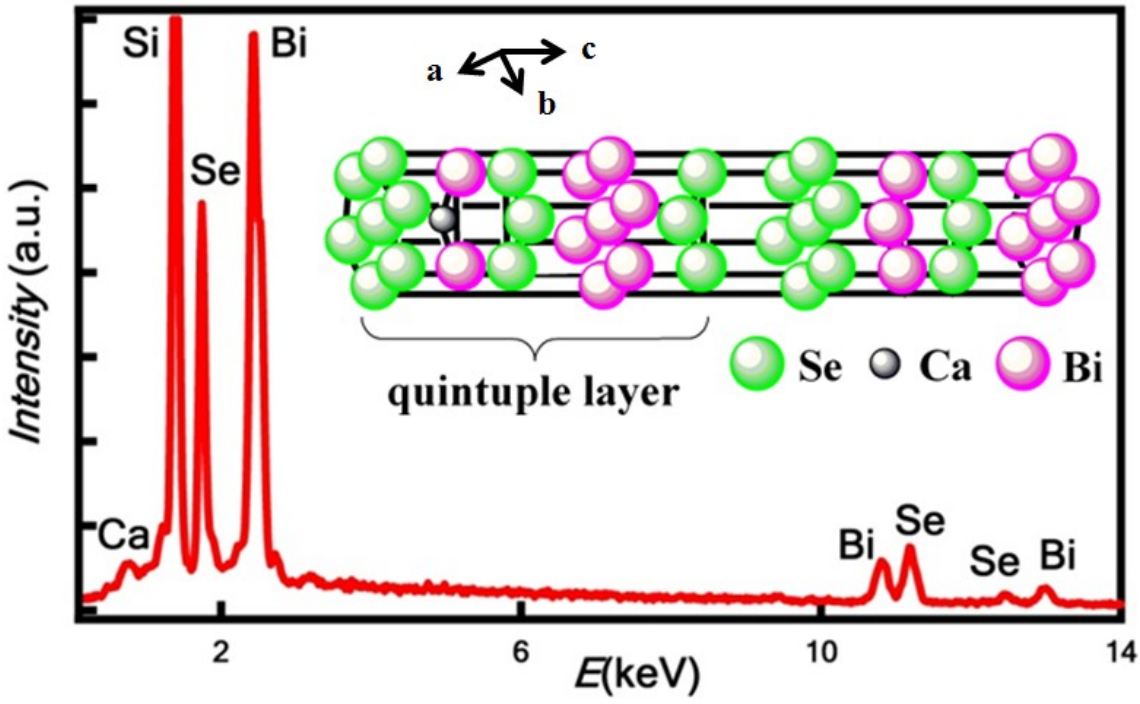

Fig. 5.1 Energy-dispersive x-ray spectroscopy (EDS) characterization of $Ca_xBi_{2-x}Se_3$. Inset Lattice structure schematics.

The small calcium peak in Fig. 5.1 is representative of its small concentration in the sample. A strong silicon peak in the energy spectrum arises from the substrate's contribution, meaning that the electron beam can penetrate through the TI material.

Table 5.1 Elemental analysis of Bi_2Se_3 with calcium doping

Element	Measured weight% (W%)	Measured chemical composition ($CC_{measure}$)
Bi	54.92	1.985
Se	31.37	3
Ca	.08	.015
Si	13.63	
Total	100	

Table 5.1 summarizes element analysis of $Ca_xBi_{2-x}Se_3$ material, where x is the calcium doping level. The second column is the measured weight of each element by its intensity integration. The measured weight percentage (W%) of each element is its relative atomic weight in the compound, *e.g.* calcium's weight percentage is calculated as

$$W_{Ca}\% = x * \text{calcium atomic weight/entire weight of } Ca_xBi_{2-x}Se_3 \qquad (5.1)$$

Calcium atoms only substitute bismuth atoms, hence the empirical number of selenium in is constant (=3). Therefore, the measured chemical composition ($CC_{measure}$) for each element is calculated using selenium as reference (Eq. 5.2). The accurate doping level is important to tune the Fermi level into the bulk band gap of Bi_2Se_3[27].

$$CC_{measure} = \frac{W\%}{\text{atomic weight}} \frac{\text{Selenium atomic weight}}{\text{Selenium weight\%}} * 3 \qquad (5.2)$$

Because the optical contrast of microscopy is not very effective for selecting TI films with thickness more than 20 nm, atomic force microscopy is widely used to measure their thicknesses, which are on average ~ 80 nm. The films are selected for their size (no smaller than 4 μm*2 μm for four terminal geometry) and the uniformity for convenient nano-fabrication. Fig. 5.2 inset shows an SEM image of a typical flake with scale bar 2 μm.

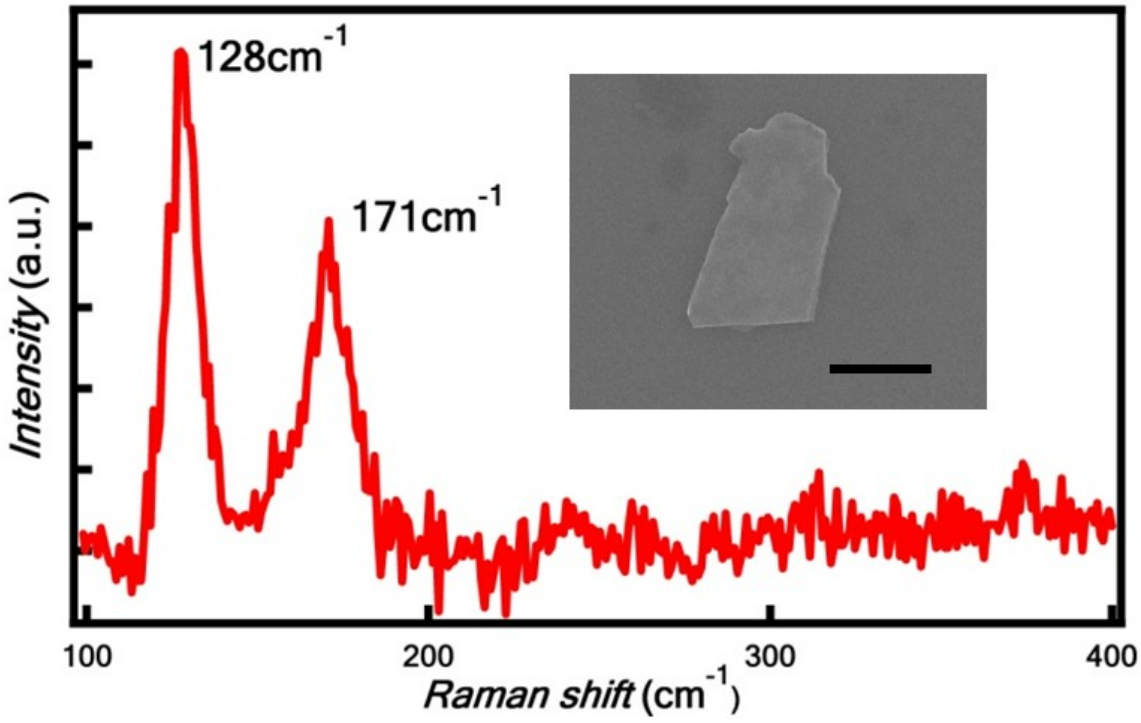

Fig. 5.2 Materials characterization: Raman Spectroscopy and SEM image of a Bi_2Se_3 flake. Scale bar: 2 μm

Fig. 5.2 shows the Raman spectroscopy using the 532 nm laser for a typical flake at room temperature (300 K). Since this material is sensitive to heating via laser point, we only use the lowest power to avoid burning the sample. Two prominent peaks are located at

128 cm^{-1} and 171 cm^{-1}, slightly shifted from those found in pure Bi_2Se_3 single crystal[22,23]. They correspond to two high frequency modes E_g^2 and A_{1g}^2, respectively. These peaks describe two different phonon vibrational modes at the Brillouin zone center (q=0) [22]: E_g^2 explains the in-plane vibration and A_{1g}^2 demonstrates the transverse mode. The broad flat response from Raman shift 200 cm^{-1} to 400 cm^{-1} is related to the two-phonon excitation process and similar features observed in far-infrared and midinfrared (IR) reflectance and transmission measurements[17] confirmed its excitation mechanism.

V-2. Device fabrication and measurement

To create Josephson junctions based on Bi_2Se_3 thin films, we use standard lithography as discussed in chapter III to fabricate 4-terminal devices with superconducting electrodes that consist of 10 nm Ti and 120 nm Al. An SEM image of the device is shown in Fig. 5.3(c). The source-drain spacing is ~ 200 nm. Electrical measurements are performed in our He^3-pumped cryostat that was fitted with 3-stage filters to reduce high frequency noise and ensure low electron temperature[24]. Al is a superconductor with a transition temperature T_c~1.2 K and superconducting gap Δ~180 meV.

At 4 K, the device's normal state resistance is R_n~100 Ω, with very weak gate dependence, suggesting large bulk contribution. After cooling the device to a base temperature of 260 mK, we current-bias the device from the outer electrodes and monitor the voltage drop V across the two inner electrodes. A typical current-voltage (*I-V)*

characteristic is shown in Fig. 5.3(a). For small current, V is zero, indicating the presence of supercurrent, which indicates that the device yields a Josephson Junction with the topological insulator as the weak link. For large I, V scales linearly with I, recovering the normal state resistance of the device. The critical current I_c, *i.e.* the largest supercurrent value sustained by the device, is ~5 nA, with only slight gate dependence. No hysteresis is observed, suggesting an over-damped junction or under-damped junction with prominent premature switching.

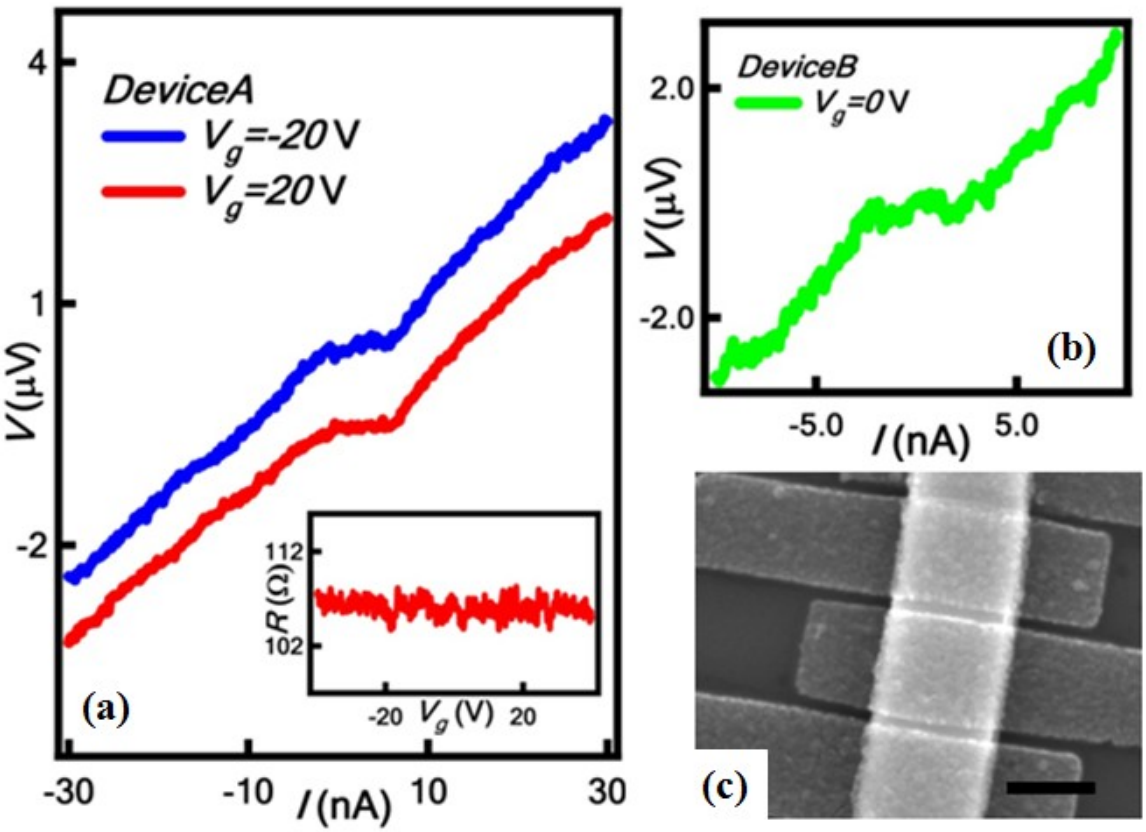

Fig. 5.3 Device transport measurement and SEM image

For a diffusive SNS junction[25], the I_cR_n product at $T=0$ is given by

$$I_c \sim 2\Delta / eR_n \qquad (1)$$

For Δ~180 meV and R_n=100 Ω, we estimate a theoretical value of I_c ~3 μA, which is three orders of magnitude larger than the experimental value. This large variation could be due to material defects and thermal fluctuations in the S-TI-S Josephson junctions. Further studies should focus on even thinner films and the Schottky barrier between the TI material and electrodes[26].

Conclusions

In summary, we characterize the stoichiometry of calcium doped Bi_2Se_3 and observe a critical current ~ 5 nA with weak gate dependence in S-TIs-S Josephson Junctions, but a more extensive study is necessary to investigate its gate dependence and relation to Majorana fermions.

References:

1) M. Z. Hasan and C. L. Kane, *Rev. Mod. Phys.* **82**, 3045 (2010).

2) J. Moore, *Nature Physics* **5**, 378-380 (2009).

3) A. H. Castro Neto, F. Guinea, N.M.R. Peres, K.S. Novoselov, A.K. Geim, *Rev. Mod. Phys.* **81**, 109 (2009)

4) K. S. Novoselov, A. K. Geim, S. V. Morozov, D. Jiang, Y. Zhang, S. V. Dubonos, I. V. Grigorieva, A. A. Firsov, *Science* **306**, 666 (2004)

5) K. S. Novoselov, D. Jiang, F. Schedin, T. J. Booth, V. V. Khotkevich, S. V. Morozov, A. K. Geim, *PNAS* **102**, 10451 (2005).

6) B. A. Bernevig, T. L. Hughes, and S. C. Zhang, *Science* **314**, 1757-1761 (2006).

7) M. Konig, S. Wiedmann, C. Brune, A. Roth, H. Buhmann, L. W. Molenkamp, X.-L. Qi, and S.-C. Zhang, *Science* **318**, 766-770 (2007).

8) X. L. Qi and S. C. Zhang, *Physics Today* **63** (1), 33-38 (2010).

9) L. Fu and C. L. Kane, *Phys. Rev. Lett.* **100**, 096407 (2008)

10) F. Wilczek, *Nature Physics* **5** (9), 614-618 (2009).

11) S. Urazhdin, D. Bilc, S. D. Mahanti, S. H. Tessmer, Theodora Kyratsi and M. G. Kanatzidis, *Phys. Rev. B* **69**, 085313 (2004)

12) James G. Analytis, Jiun-Haw Chu, Yulin Chen, Felipe Corredor, Ross D. McDonald, Z. X. Shen, and Ian R. Fisher, *Phys. Rev. B* **81**, 205407 (2010)

13) Guanhua Zhang, Huajun Qin, Jing Teng, Jiandong Guo, Qinlin Guo, Xi Dai, Zhong Fang, and Kehui Wu, *Appl. Phys. Lett.* **95**, 053114 (2009)

14) Yi Zhang, Ke He, Cui-Zu Chang, Can-Li Song, Li-Li Wang, Xi Chen, Jin-Feng Jia,

Zhong Fang, Xi Dai, Wen-Yu Shan, Shun-Qing Shen, Qian Niu, Xiao-Liang Qi, Shou-Cheng Zhang, Xu-Cun Ma and Qi-Kun Xue, *Nature Physics* **6** (8), 584-588 (2010)

15) Y. S. Hor, A. Richardella, P. Roushan, Y. Xia, J. G. Checkelsky, A. Yazdani, M. Z. Hasan, N. P. Ong, and R. J. Cava, *Phys. Rev. B* **79**, 195208 (2009)

16) L. Andrew Wray, Su-Yang Xu, Yuqi Xia, Yew San Hor, Dong Qian, Alexei V. Fedorov, Hsin Lin, Arun Bansil, Robert J. Cava and M. Zahid Hasan, *Nature Physics* **6** (11), 855-859 (2010)

17) A. D. LaForge, A. Frenzel, B. C. Pursley, Tao Lin, Xinfei Liu, Jing Shi, and D. N. Basov, *Phys Rev B* **81**, 125120 (2010)

18) Zhiyong Wang, Tao Lin, Peng Wei, Xinfei Liu, Randy Dumas, Kai Liu, and Jing Shi, *Applied Physics Letter* **97**, 042112 (2010)

19) R. W. G. Wyckoff, *Crystal Structure*, **Vol. 2**, Malabar, Florida: Krieger (1986)

20) Sungjae Cho , Nicholas P. Butch , Johnpierre Paglione , and Michael S. Fuhrer, *Nano Lett* **11** (5), 1925-1927 (2011)

21) D. Teweldebrhan, V. Goyal, and A. A. Balandin, *Nano Lett* **10** (4), 1209-1218 (2010)

22) W. Richter, H. Kohler, and C. R. Becker, *Phys Status Solidi B* **84** (2), 619-628 (1977)

23) S. Y. F. Zhao, C. Beekman, L. J. Sandilands, J. E. J. Bashucky, D. Kwok, N. Lee, A. D. LaForge, S. W. Cheong, and K. S. Burch, *Applied Physics Letter* **98** (14), 141911 (2011)

24) F. Miao, W. Bao, H. Zhang, and C.N. Lau, *Solid State Communications* **149**, 1046 (2009)

25) J. R. Schrieffer and M. Tinkham, *Review Modern Physics* **71** (2), S313-S317 (1999)

26) N. P. Butch, K. Kirshenbaum, P. Syers, A. B. Sushkov, G. S. Jenkins, H. D. Drew, and J. Paglione, *Phys. Rev. B* **81**, 241301 (2010)

27) Z. Wang, P. Wei, J. Shi, *Front. Phys.* **7(2)**, 160 (2012)

28) G. Moore and N. Read, *Nucl. Phys. B* **360**, 362 (1991)

Chapter VI. Thermal expansion coefficient of graphene and its thickness dependence

Graphene[1, 2] is an astonishing material with exceptional thermal[3, 4] and mechanical[5, 6, 7] properties. In this chapter, we examine thermal expansion effect of suspended graphene. Firstly, we discuss the fabrication procedures of suspended graphene with different boundary conditions. Secondly, we present the thermal expansion measurement setups: scanning electron microscopy equipped with a local heater and a thermometer that allow *in situ* tuning of temperature while monitoring the morphological change of the sample. The average thermal expansion coefficient (TEC) of graphene is extracted from SEM images at different temperatures. Curiously, we observe a non-monotonic dependence of TEC on the thickness of graphene sheets, *i.e.* TEC firstly decreases with increasing film thickness up to ~10 nm, then increases with the thickness. We speculate that this unexpected behavior is due to the competition between graphene's intrinsic TEC and a thickness-dependent friction between the graphene sheets and the substrate.

VI-1. Preparation of suspended graphene

We suspend graphene thin films by depositing them over the pre-defined trench wafer[7]. Unlike the buffered oxide etchant (BOE) wet etch technique[8, 9] or attaching graphene sheets to the bridge-like electrodes[10] via a multi-level lithography technique, our protocol, developed by Dr. Wenzhong Bao[7, 11], does not involve the use of chemicals. Therefore,

the materials prepared with this protocol are free from contamination and of high quality. The fabrication process is described below.

VI-1.1. Trench wafer preparation

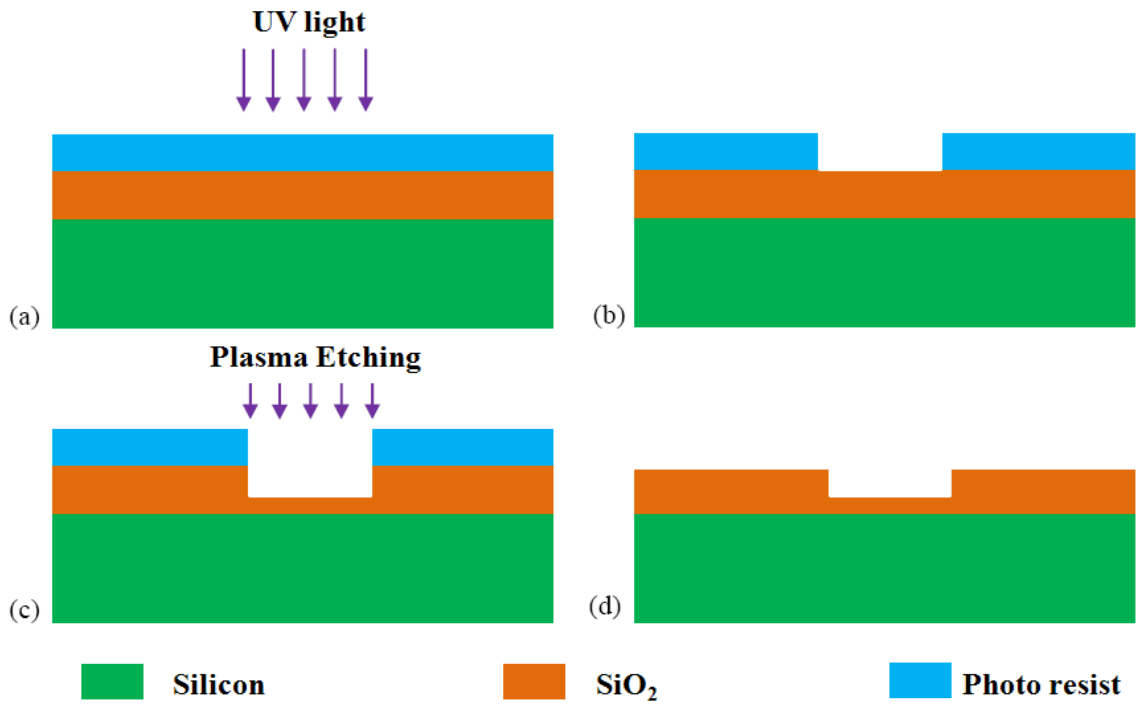

Fig. 6.1 Schematic illustrating the process of trench wafer fabrication: (a) Si/SiO_2 wafer covered by photo resist is exposed to UV light. (b) The exposed resist is removed via developing in the resist-developer (MF J-321). (c) ICP plasma etches the exposed SiO_2 layer while the rest of wafer is protected by photo resist mask, and the etched depth is 200 nm. (d) The final structure of the Si/SiO2 trench wafer; the residual photo resist is cleaned by oxygen plasma.

Our four-inch silicon wafers from University Wafer are highly *p* doped (0.001~0.005 ohm-cm) and capped with a 300 nm thick of SiO_2 layer on top. These wafers are

fabricated and diced at UCSB nanofabrication facility. Fig. 6.1 shows the trench fabrication process on the Si/SiO_2 wafer. The whole 4-inch wafer is coated with photo resist, baked on the hot plate at 180 °C to harden the resist layer, and exposed to UV light. The wafer is then developed in the resist-developer to generate an array of 3 μm-wide lines at 200 μm pitch.

Next, the wafer is transferred into inductively coupled plasma (ICP) chamber for dry etching. ICP has several advantages as plasma dry etching, including the anisotropic feature (etch depth D_{etch}/ etch pattern width W_{etch}) and fast etching rate. A good plasma etch chemistry requires high selectivity, *i.e.* the reactant only etches the target material (SiO_2 in our case), but not the protective layer (photo resist). We use the ICP plasma to trim the SiO_2 layer down to 100 nm as the final thickness, which can still serve as the dielectric layer for the gate electrode without leakage. Lastly, the resist residue is removed by oxygen plasma, and the wafer is coated with a new layer of resist for protection during dicing.

VI-1.2. Graphene exfoliation by Blade-scratch

Before graphene exfoliation, the diced 4.8 mm*4.8 mm trench wafers are ultrasonically cleaned in acetone for 20 minutes, rinsed with isopropyl alcohol (IPA) and dried by compressed nitrogen gas. Fig. 6.2(a)~(c) show the process of graphene exfoliation by a razor blade, including graphite deposition, blade "scratching" to graphene identification.

We deposit a piece of freshly peeled graphite to cover the trench wafer, then use a razor blade to gently scratch the surface of graphite across the trench.

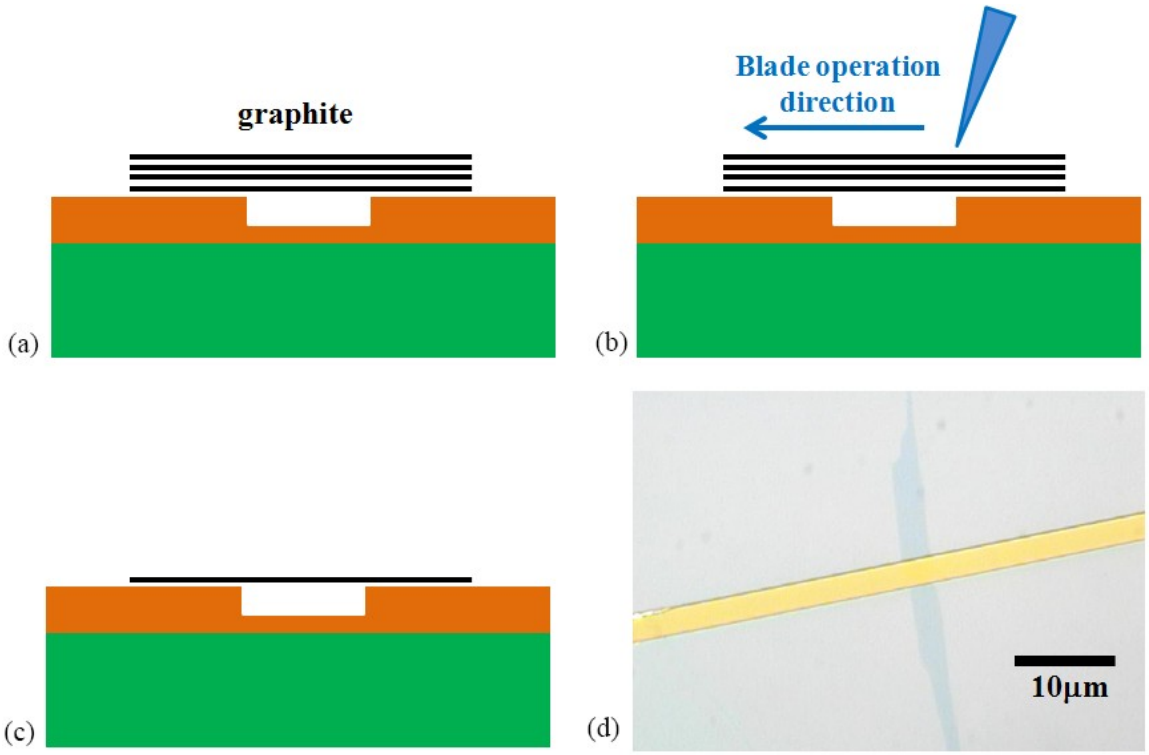

Fig. 6.2 Schematics illustrating the process for graphene exfoliation over the trench wafer and optical image: (a) Deposit large graphite pieces on the Si/SiO_2 trench wafer. (b) A razor blade is used to scratch the area covered by graphite from one direction only. (c) Monolayer or few-layer graphene can suspend over the trench. (d) Optical image of a typical piece of graphene. Scale bar: 10 μm.

A large piece of bulk graphite is in silvery color under optical microscope, while flake thinner than 20 nm is greenish. After scratching for ~5 times, we search the wafer for the graphene flakes under optical microscope. If no desirable graphene thin film is found, the blade-scratch process is repeated. Fig. 6.2(d) shows a nice sheet of suspended graphene

over a trench. Note that the suspended portion of graphene is hard to be discerned, and we can only infer its suspension from the ends that rest on substrates or image it under SEM with a tilted angle. We also use Raman spectroscopy to identify the number of layers for graphene flakes that are thinner than 4 layers, and AFM for thicker samples.

VI-2. *In situ* thermal expansion measurement setup

Selected wafers with suspended graphene are mounted on a heater stage with a thermocouple built by Dr. Wanyoung Jang (Fig. 6.3)[7]. The thermally conductive cement (thermal conductivity 1.6 W/m·K) limits the temperature differences across the graphene, the substrate and the cement junction within to 4 K at 725 K[7], therefore allowing accurate measurement of temperature. In our study, the entire assembly is placed into an SEM (XL30 FEG) chamber for *in situ* imaging, and tilted to 75° to capture the side view of the graphene suspending over the trench. The power input of the heater and thermocouple are controlled via electrical feedthroughs. The heater has an upper temperate limit T_{max} of ~480 K to avoid overheating of wires.

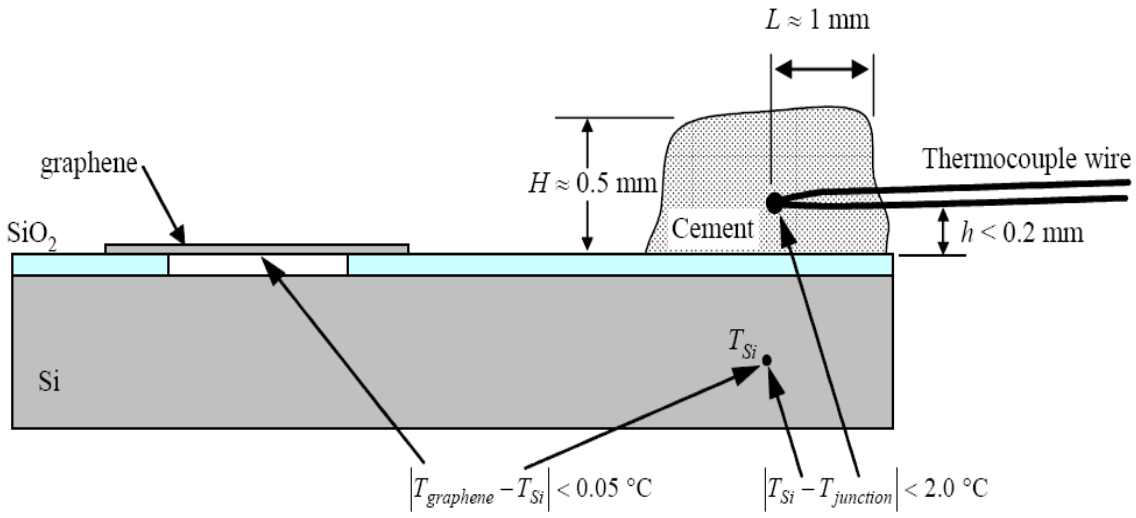

Fig. 6.3 Schematic of the heater stage for in situ SEM imaging. Reprint with permission from W. Bao, F. Miao, Z. Chen, H. Zhang, W. Jang, C. Dames, and C. N. Lau, Nature Nanotechnology 4, 562 (2009). Copyright (2009) © Nature Publishing Group

VI-3. Thermal expansion coefficient (TEC) of graphene with free boundaries

In the previous experiment[7], TEC for single layer graphene were measured for the temperature range between 300 K and 400 K. Here we extend the measurement for graphene or thin graphite with different thickness. Before SEM imaging, all suspended graphene sheets are annealed in a programmable furnace (thermal fisher) at 520 K for 45 minutes in H_2/Ar mixture with flow rates 0.1 slm and 0.5 slm, respectively, then cooled naturally to room temperature. The purpose of gas annealing is to ensure that the suspended portion of graphene is sagged, so that the device's morphological change upon subsequent thermal cycling to 470 K is reversible. The device is then placed in the SEM chamber, and heated to T_H~470 K. We then turn off the heater to allow the suspended

sheet cool down to T_L~300 K over 2 hours, while capturing the morphological changes of the suspended by SEM.

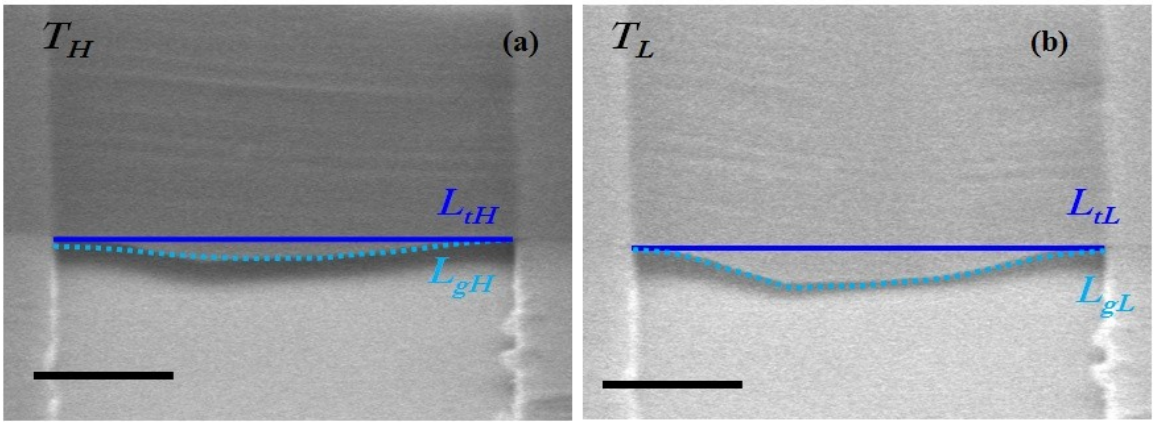

Fig. 6.4 Titled-angle SEM images of suspended graphene at different temperatures. (a) High-temperature T_H~470 K SEM image. (b) Graphene membrane clearly sags at T_L~300 K. Both scale bars are 1 μm, L_t and L_g denote trench width and graphene arc length, respectively.

To measure the TEC, we compare the graphene sheet's profile across the trench at high and room temperatures. Invariably, the graphene sheet sags more at room temperature (Fig. 6.4(b)) than high temperature (Fig. 6.4(a)), suggesting that it contracts (expands) upon heating (cooling). We import these SEM images into Design CAD software to measure the graphene arc length L_g and the trench width L_t, which are outlined by blue solid curve and light blue dotted curve, respectively. The ratio of these two lengths at different temperatures $l(T)= L_g(T)/ L_t(T)$ allows us to calculate the thermal expansion coefficient (TEC) of graphene. All the measurement and calculations are carried out independently for three times to obtain reliable average value and standard deviation. For the first order approximation of graphene TEC[7],

$$\alpha_{eff} = \frac{dl(T)}{dT} \approx \alpha_g - \alpha_{trench} \qquad (1)$$

where α_g is TEC of graphene, α_{trench} is TEC of the Si/SiO_2 trench and $\frac{dl(T)}{dT}$ is the derivative of *l(T)* with respect to temperature *T*. Given the fact that the Si layer is 1700 times thicker than the SiO_2 layer, α_{trench} is dominated by Si. Thus, graphene average TEC $\overline{\alpha_g}$ of two temperatures T_1 and T_2 can be obtained by

$$\overline{\alpha_g} = \frac{L_g(T_1)/L_t(T_1) - L_g(T_2)/L_t(T_2)}{T_1 - T_2} + \alpha_{trench} \qquad (2)$$

, where T_1 and T_2 denote different temperature points, $L_g(T_1)/L_t(T_1)$ and $L_g(T_2)/L_t(T_2)$ are the corresponding length ratio *l(T)* at specific temperature T_1 and T_2.

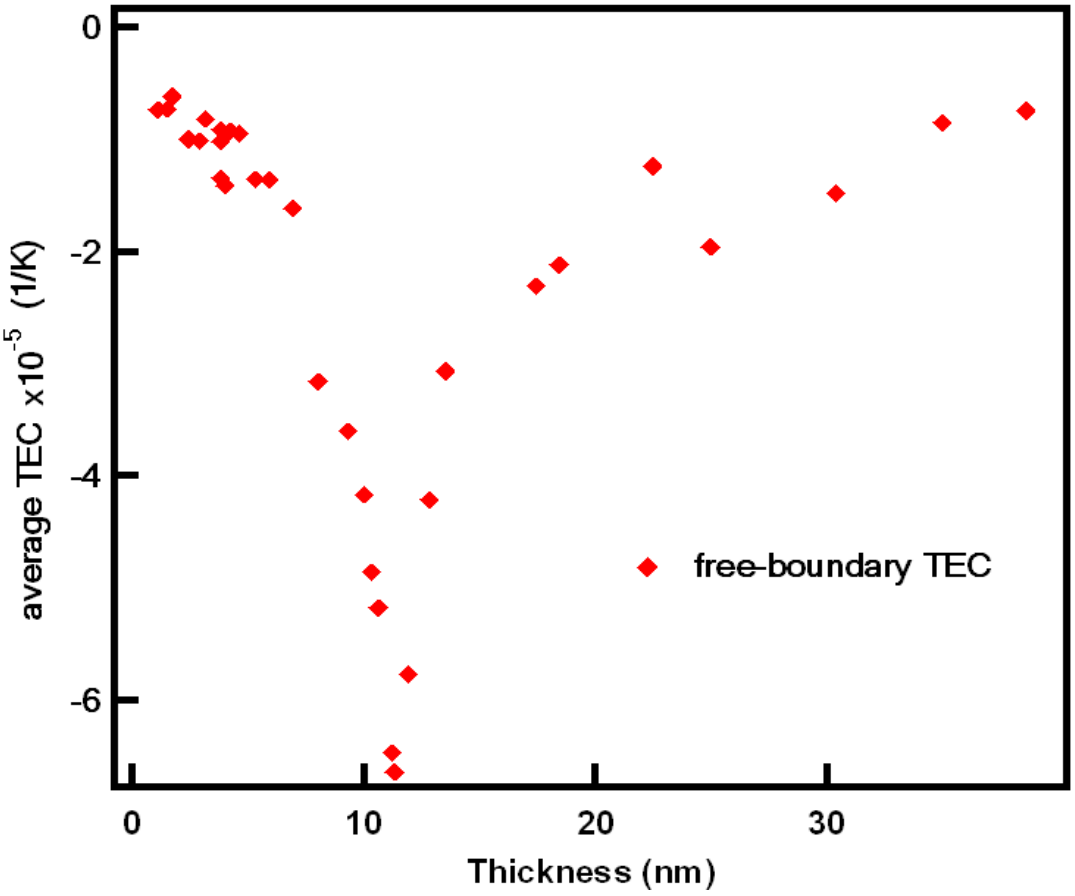

Fig. 6.5 Thickness dependence of graphene TEC with free boundaries

We measure the TEC of the suspended graphene membranes with different thicknesses as plotted in Fig. 6.5. The membrane's thickness is determined by atomic force microscope (AFM, Veeco) after *in situ* SEM imaging. All of the average TEC values are obtained at two temperature points: T_H~470 K and T_L~300 K under the same experimental condition. We note that all thin graphite pieces have negative TEC, which matches mode-dependent Gruneisen theory[14, 15]. This theory describes the relation among the anharmonicity of the interactomic potential, related phonon modes and bond length. Comparing with other high-frequency phonon modes, the transverse acoustic (ZA) modes in graphene films have lower excitation energy[16]. Therefore, ZA phonons are excited with increasing temperatures, and these out-of-plane atomic movements cause the contraction tension[17]of 2D thin film. However, one expects that TEC of few-layer graphene would monotonically increase with increasing thickness, and approach that of graphite for sufficiently thick samples. This intuitive expectation is confirmed by theoretical calculations[22 - 25]. However, our data in Fig. 6.7(a) contradict this expectation – the measured TEC is non-monotonic in thickness, with a minimum dip at around 10 nm.

To explain this unexpected behavior, we speculate that there exists a thickness-dependent friction between graphene sheets and SiO_2 substrate. The friction decreases with the increasing graphene thickness, because the thicker graphene films have larger bending rigidity and conforms less to the corrugations on the substrate. This external force competes with few-layer graphene's intrinsic thermal contract, thus giving rise to the

non-monotonic dependence of TEC on thickness. To verify this hypothesis, we attempt to vary the friction by clamping the graphene sheets with electrodes.

VI-4. Shadow mask technique

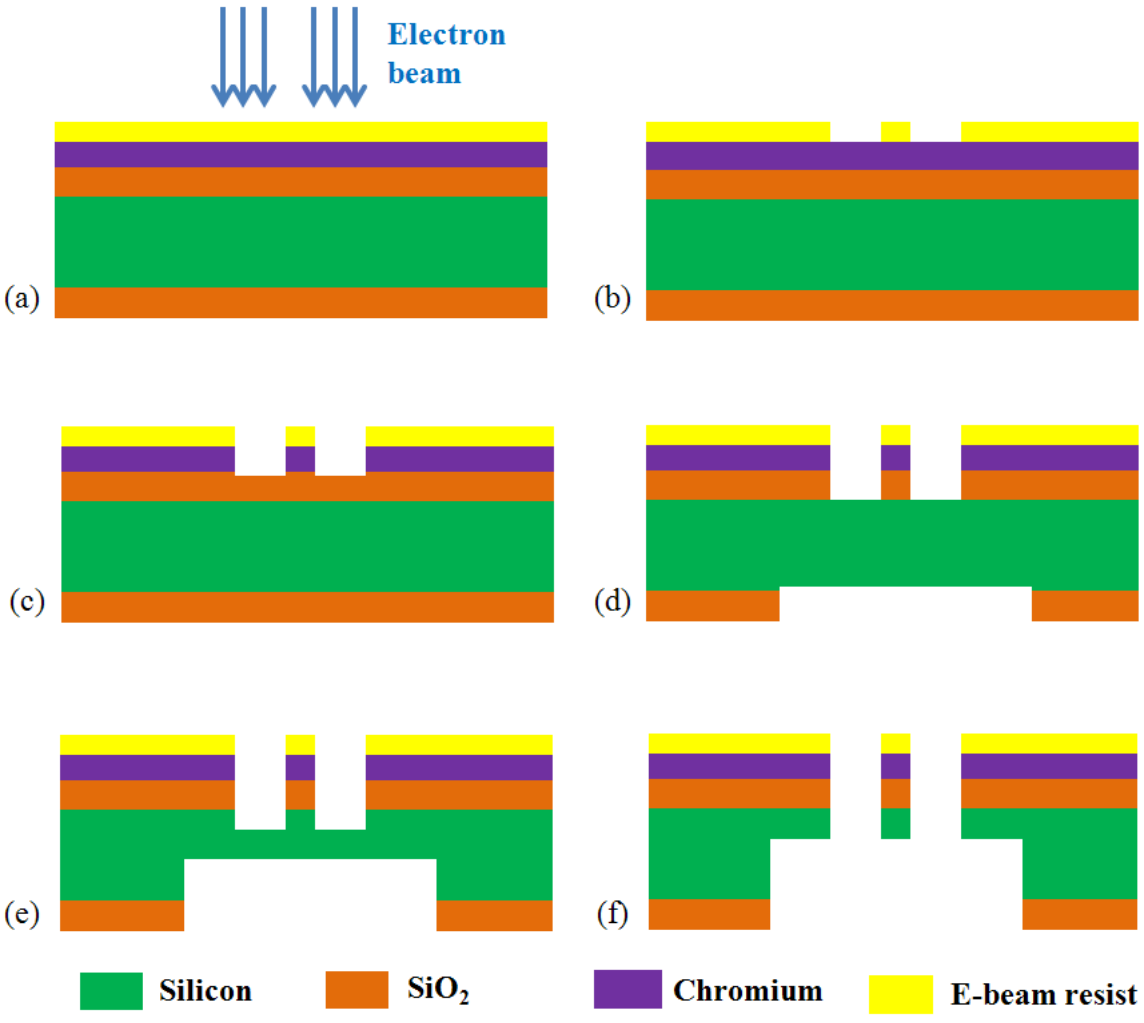

Fig. 6.6 Schematic illustration of the shadow mask fabrication process

We deposit electrodes on graphene sheets that are suspended over trenches by evaporating metals through shadow masks, a lithography-free technique that is originally developed by Dr. Wenzhong Bao[12]. We can then compare the TEC difference between clamped and free-boundary (unclamped) devices.

The {100} oriented silicon wafers for shadow mask fabrication are 2 inch in diameter and 200 μm in thickness, with 300 nm of thermally grown SiO_2 on both sides. The SiO_2 layer reduces the mechanical tension between the silicon wafer and the metal layer during nano-fabrication, and acts as the mask during back-side silicon etching. The shadow mask fabrication process is depicted in Fig. 6.6(a)~(f). After cleaning in acetone and IPA, one side of the mask wafer is coated with 300 nm chromium by e-beam evaporation, followed by a layer of PMMA resist, as shown in Fig. 6.6(a). During e-beam evaporation, we keep the internal temperature of the chamber below 30 °C to ensure uniform thickness of the chromium layer. We denote the PMMA side as front side, and the side without PMMA as the back. The chromium layer serves as the etching mask for SiO_2 and Si. PMMA acts as the protective layer of the chromium during wet etching. Then the entire 2-inch mask wafer is cut into centimeter-sized pieces for mask fabrication. Standard e-beam lithography completes the designed shadow mask pattern as shown in Fig. 6.6(a) and (b). The exposed chromium layer is removed by immersing in chromium etchant solution (1020AC) for 2~5 minutes. The etched part loses the shiny metallic color and is dark as viewed on the Si/SiO2 substrate. Next, the SiO_2 layers on both sides are removed by reactive ion etching (RIE) using CF_4 diluted with O_2 (flow ratio, 50:1). The silicon

layer, which is 200 μm thick, is etched through by ICP dry etching to complete the shadow mask with windows as designed. The crucial and primary parameters of plasma dry etch, including RIE and ICP, are the source gas and the flow rate, which determine the basic plasma chemistry. Other significant factors for the plasma reaction include: bias power, pressure, temperature, gas ratio (if compound) and etching time. (Please see Appendix for ICP and RIE protocol).

During the etching process, the wafer's edges are fixed on the sample holder of plasma chamber with scotch tape. The cross section of the ICP processed wafer is shown in Fig. 6.6(e) and (f). To open windows in the Si wafer, we etch 30~40 μm from the front side of the wafer, and the rest of the silicon layer is removed from the back side. The finest structure of the shadow mask is 2 μm and the etch aspect ratio (etch depth/etch width) is larger than 10 that is achieved by the Bosch method[13]. The principle of Bosch method is the alternative plasmas strike on the target materials in turns. In our case, SF_6 is the effective etchant for silicon and C_4F_8 acts as the passive gas that deposits adhesive material (for example, C/H polymer) onto the sidewall to maintain the anisotropic etching profile. The forward bias enables the vertical injection of the plasma onto shadow mask wafer and reduces isotropic effect.

Fig. 6.7(a) and (b) illustrate SEM images of completed shadow masks with different geometries. It is noteworthy that the finest structure in Fig. 6.7(a) is about 2 μm. The mask presented in Fig. 6.7(b) contains two windows (indicated by red arrows) for

alignment. After suspending a graphene sheet over a trench, we mount the shadow mask onto micromanipulators with *XYZ* translation stage, and locate and align with the graphene sheet via the alignment windows. The whole assembly is then transferred into the evaporator chamber for metal deposition.

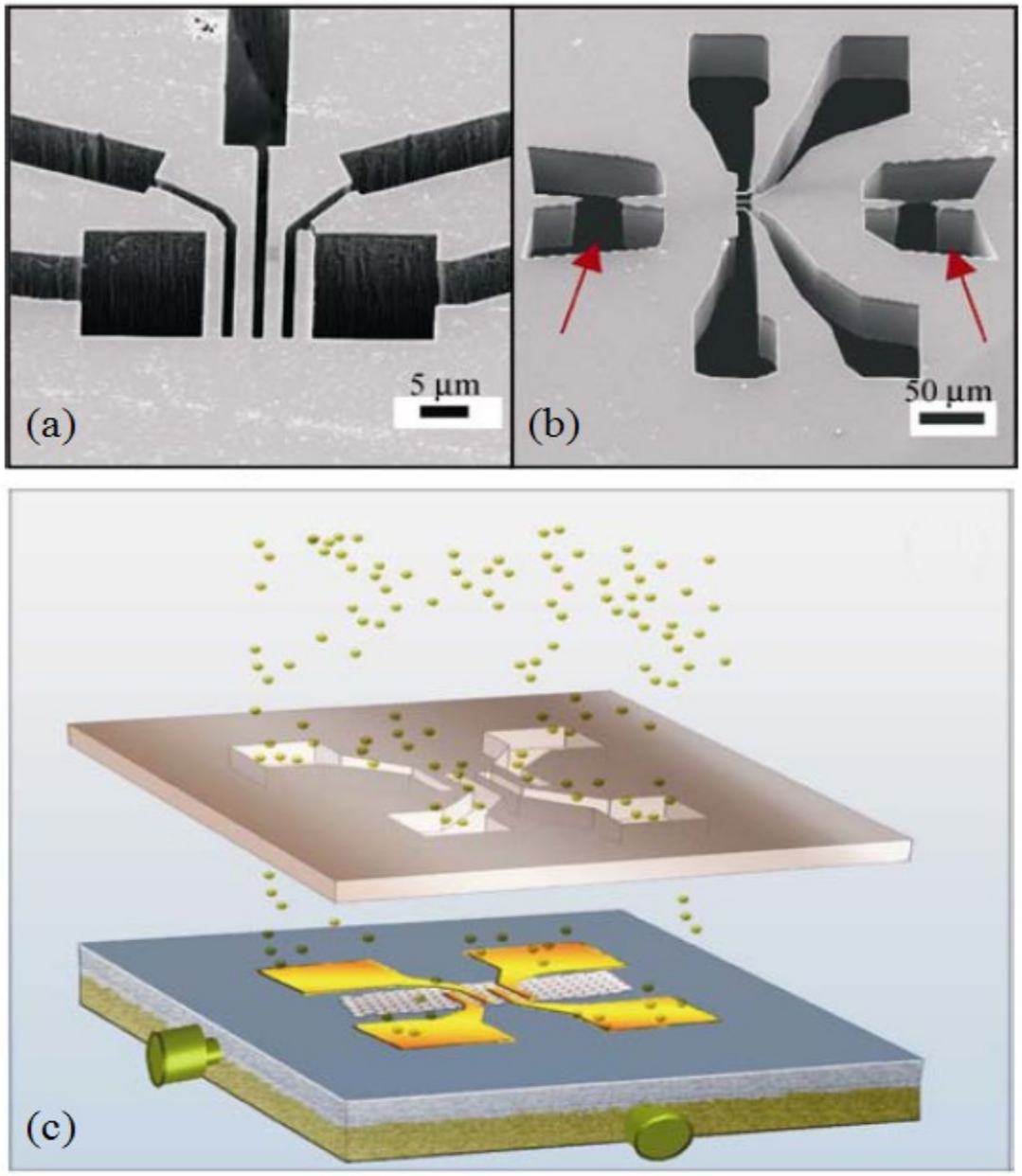

Fig. 6.7 SEM images of shadow masks with different geometries, and schematics for mask alignment and evaporation: (a) SEM image of a five-terminal shadow mask. Scale bar: 5 μm. (b) SEM image of a four-terminal shadow mask with scale bar of 50 μm, red arrows indicate alignment window. (c) Schematic image for device alignment and evaporation. **Reprint with permission from W. Bao, G. Liu, Z. Zhao, H. Zhang, D. Yan, A. Deshpande, B.J. LeRoy and C.N. Lau, Nano Research, 3, 98 (2010). Copyright (2010) © Tsinghua University Press and Springer-Verlag Berlin Heidelberg**

VI-5. TEC of graphene with fixed boundaries

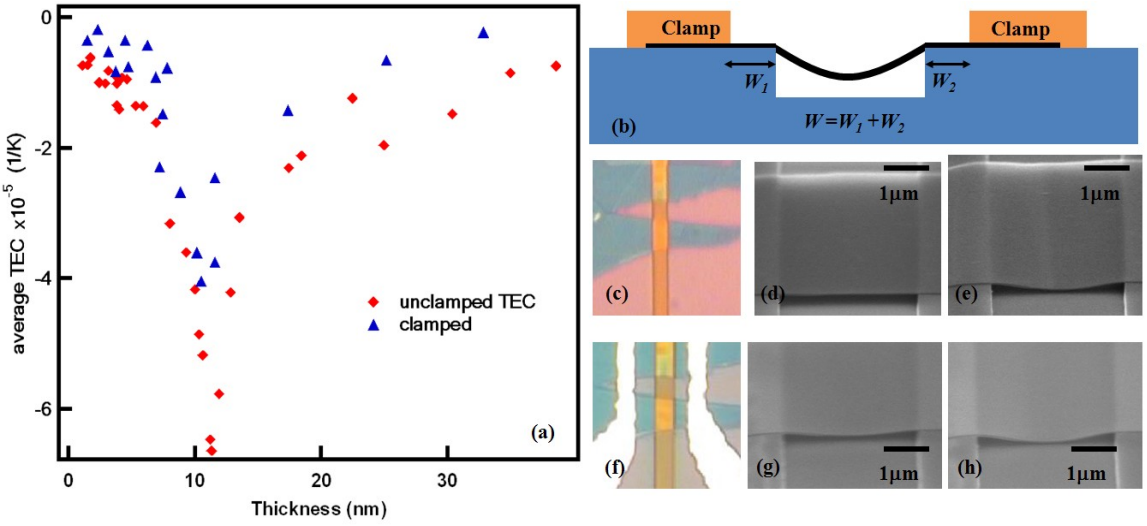

Fig. 6.8 Thermal expansion of suspended graphene membranes (a) Plot of measured average TEC as a function of graphene thickness. Red diamonds: unclamped devices, same as Fig. 6.5. Blue triangles: devices with electrodes. (b) Schematic of clamped suspending graphene device. (c) – (f) Optical and SEM images of the same suspended graphene stripe before ((c) –(e)) and after ((f) –(h)) metal deposition, respectively. (d) and (g) are taken at high temperature T_H~470 K, and (e) and (h) are taken at room temperature T_L~300 K. All scale bars indicate 1 μm.

Fig. 6.8(a) compares the clamped graphene TEC $\overline{\alpha_{clamped}}$ with the unclamped TEC $\overline{\alpha_{unclamped}}$ as shown in Fig 6.5. The points of clamped TEC are obtained from the

clamped membranes with the total clamping distance W smaller than 1 μm. The SEM images of Fig. 6.8(d) and (e) are taken before electrode deposition at T_H~470 K and T_L~300 K, respectively, while Fig. 6.8(g) and (h) are taken after electrode deposition for the same suspended graphene. Addition of electrodes has little effect on the device's morphology at room temperature (as shown in Fig. 6.8(e) and (h)). In contrast, at 470K, the clamped graphene in Fig. 6.8(d) sags noticeably more that of clamped device (Fig. 6.8(h)), indicating $\overline{\alpha_{unclamped}}$ is algebraically smaller (larger in magnitude) than $\overline{\alpha_{clamped}}$ as shown in Fig 6.8(a). These data suggest that upon heating, the substrate-supported portions of unclamped graphene contract and moves away from the trench, thus yielding apparently larger TEC; in contrast, the clamping by electrodes effectively prevents the free movement of graphene on the substrate, thus likely providing a more accurate measurements of graphene's intrinsic TEC.

On the other hand, despite the relatively smaller TEC, $\overline{\alpha_{clamped}}$ has similar non-monotonic dependence on thickness as $\overline{\alpha_{unclamped}}$. Our hypothesis is that the electrodes do not provide perfect clamping, particularly since they are not deposited precisely along the trench, but at distance W_1 and W_2 from the trench edges (as shown in Fig. 6.8(b)); thus the portions of graphene that are supported on the substrate between the trench and the electrodes are still free to move under thermally induced tension.

To investigate the clamping effect, we deposit electrodes on the same graphene sheet repeatedly and successively reduce the total clamping distance $W=W_1+W_2$ of the device;

after each metal deposition, we image the sheet at 470K and room temperature, and measure its TEC. Fig. 6.9(a) displays the TEC ratio $R=\overline{\alpha_g(unclamped)}/\overline{\alpha_g(clamped)}$ at different clamping distances for three samples. They exhibit the same trend: with increasing W, R decreases and approaches ~1. We tentatively fit the data to an exponential function $R\sim Aexp(-W/W_0)$, where A is a dimensionless fitting parameter and W_0 is the effective clamping distance. Another parameter we extract from the fitting curve is the TEC $\overline{\alpha_g(W=0)}$ for a fully clamped device,

$$\overline{\alpha_g(W=0)}=\overline{\alpha_g(unclamped)}/A \qquad (3)$$

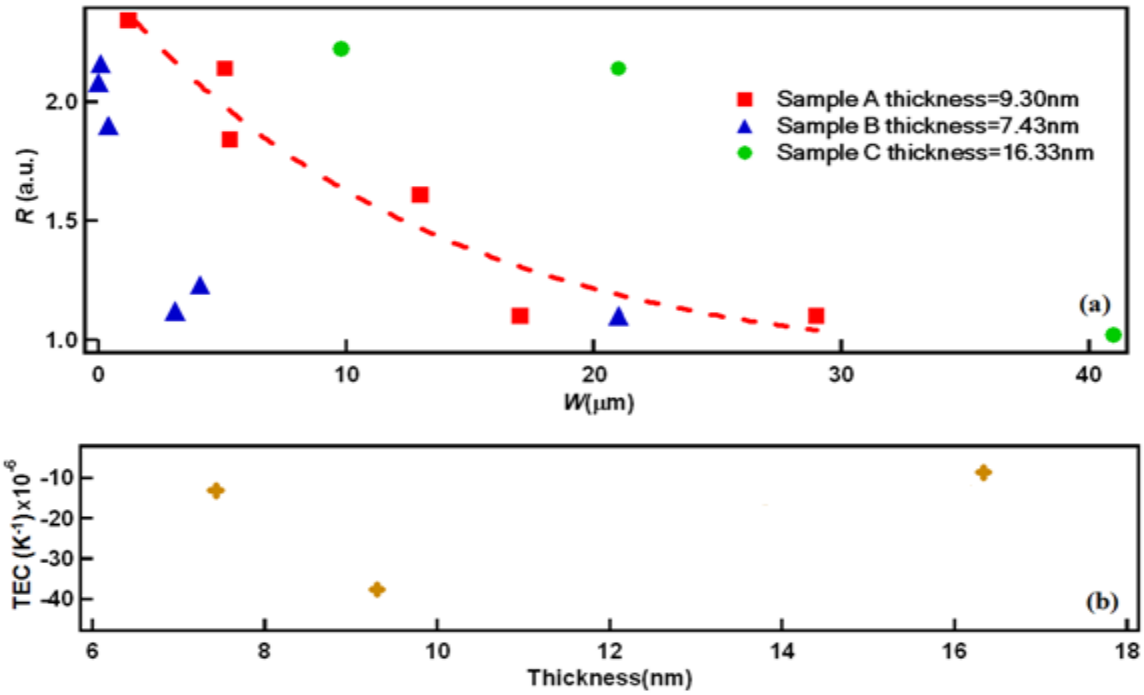

Fig. 6.9 Clamping effect of the TEC behavior and the extracted data. (a) TEC ratio $R=\overline{\alpha_g(unclamped)}/\overline{\alpha_g(clamped)}$ as a function of clamping distance W for three samples. Sample A (red square) is fitted into an exponential function (red dotted line in Fig. 6.9(a)). (b) The extracted $\overline{\alpha_g(W=0)}$ from Eq. 3 as a function of sample's thickness.

Table 6.1 lists the variables that we extract from Fig. 6.9. There is much scatter among the extracted values of W_0. Fig. 6.9(b) plots $\overline{\alpha_g(W=0)}$ *vs.* thickness of different samples. The data points can in principle be fitted to a straight line, but preclude a definite conclusion due to the limited number. In order to address this non-monotonic dependence of TEC on film thickness, we would need to examine a larger number of samples to determine the nature of this behavior.

Table 6.1 Fitting information of Fig. 6.9(a)

	Film thickness(nm)	W_0 (μm)	TEC(K^{-1}) at W=0
Sample A	9.30	12.84	-3.76×10^{-5}
Sample B	7.43	1.33	-1.313×10^{-5}
Sample C	16.33	38.64	-8.64×10^{-6}

Conclusion:

This chapter describes the measurements for thermal expansion coefficient of suspended graphene. Our data presents an unusual non-monotonic dependence of TEC on film thickness, which is hypothesized to result from a competition between graphene's intrinsic thermal expansion and a thickness-dependent friction between the graphene and the substrate. Our future work includes preparing more fully-clamped graphene samples to better understand our observation and extending our measurements to other 2D materials, such as topological insulators and MoS_2.

References:

1) A. H. Castro Neto, F. Guinea, N.M.R. Peres, K.S. Novoselov, A.K. Geim, *Rev. Mod. Phys*. **81**, 109 (2009)

2) K.S. Novoselov, E. McCann, S.V. Morozov, V.I. Fal'ko, M.I. Katsnelson, U. Zeitler, D. Jiang, F. Schedin, A.K. Geim, *Nature Physics* **2**, 177 (2006)

3) A. A. Balandin, S. Ghosh, W. Bao, I. Calizo, D. Teweldebrhan, F. Miao, and C. N. Lau, *Nano Lett.* **8**, 902-907 (2008)

4) S. Ghosh, W. Bao, D. L. Nika, S. Subrina, E. P. Pokatilov, C. N. Lau, and A. A. Balandin, *Nature Mater.* **9**, 555-558 (2010)

5) J. Scott Bunch, A. M. Zande, S.S. Verbridge, I.W. Frank, D. M. Tanenbaum, J. M. Parpia, H. G. Craighead, P. L. McEuen, *Science* **315**, 490–493 (2007)

6) C. Lee, X. D. Wei, J.W. Kysar, J. Hone, *Science* **321**, 385–388 (2008)

7) W. Bao, F. Miao, Z. Chen, H. Zhang, W. Jang, C. Dames, and C. N. Lau, *Nature Nanotechnology* **4**, 562 (2009)

8) K. I. Bolotin, K. J. Sikes, Z. Jiang, G. Fundenberg, J. Hone, P. Kim and H. L. Stormer, *Solid State Comm.* **146**, 351-355 (2008)

9) J. Velasco, L. Jing, W. Bao, Y. Lee, P. Kratz, V. Aji, M. Bockrath, C. N. Lau, C. Varma, R. Stillwell, D. Smirnov, F. Zhang, J. Jung and A. H. MacDonald, *Nature Nanotechnology* **7**, 156 (2012)

10) J. Velasco Jr. , Z. Zhao, H. Zhang, F. Wang, Z. Wang, P. Kratz, L. Jing, W. Bao, J. Shi and C.N. Lau, *Nanotechnology* **22**, 285305 (2011)

11) Wenzhong Bao Ph.D thesis, UC Riverside, 2011

12) W. Bao, G. Liu, Z. Zhao, H. Zhang, D. Yan, A. Deshpande, B.J. LeRoy and C.N. Lau, *Nano Research* **3**, 98 (2010)

13) F. Laermer and A. Schilp, "Method of anisotropically etching silicon," U.S. Patent No. 5501893 3, 26, 1996

14) N. W. Ashcroft and N. D. Mermin, Solid State Physics (Holt, Reinhart, and Winston, New York, 1976)

15) C. Kittel, Introduction to Solid State Physics (Wiley, New York, 1976)

16) M. Lazzeri, C. Attaccalite, L. Wirtz, Francesco Mauri, *Phys. Rev. B* **78**, 081406 (2008)

17) T. H. K. Barron, *Ann. Phys. (N.Y.)* **1**, 77 (1957)

18) Pierre Le Doussal and Leo Radzihovsky, *Phys. Rev. Lett.* **69**, 1209–1212 (1992)

19) P. L. de Andres, F. Guinea, M. I. Katsnelson, *Phys. Rev. B* **86**, 144103 (2012)

20) M. I. Katsnelson, *Mater. Today* **10**, 20-27 (2007)

21) C. Lee, Q. Li, W. Kalb, X.Z. Liu, H. Berger, R. W. Carpick, J. Hone, *Science* **328**, 76–80 (2010)

22) N. Mounet, N. Marzari, *Phys. Rev. B* **71**, 205214 (2005)

23) J. Jiang, J. Wang, preprint, arXiv:1108.5820v1

24) P. K. Schelling, R. Keblinski, *Phys. Rev. B* **68**, 035425 (2003)

25) Y. K. Kwon, S. Berber, D. Tomanek, *Phys. Rev. Lett.* **92**, 015901 (2004)

Chapter VII. Graphene-based quantum Hall effect infrared photodetector

In this chapter, we demonstrate a quantum Hall effect (QHE) graphene-based infrared photodetector that functions at 70 K - a temperature achievable using liquid nitrogen in vapor evacuation regime. This result opens up the possibility of wider uses of QHE photodetectors if graphene, instead of the "classical" materials with two-dimensional electron gas, is utilized. The potential advantages of this approach are the increased operating temperature, reduced magnetic field and wider range of operating frequency comparing to the previous implementations of QHE detectors. The graphene-based photodetector was fabricated at UC Riverside, while Dr. Nikolai Kalugin and his group at New Mexico Institute of Mining and Technology led this project and performed the QHE and photoresponse measurements.

VII-1. Introduction

In addition to its exceptional material properties[1], graphene is a promising material for optoelectronic applications[2,3], where it may be used for fabrication of high-speed and broad spectrum photodetectors. Recent experiments demonstrated that graphene photodetectors, based on the absorption via interband transitions[4,5], can operate over mid-infrared, near-infrared, and visible parts of the electromagnetic spectrum.

A much sought-after goal for the photodetector performance is the extension of the

spectral range to longer wavelengths, including the THz regime. This, however, entails alternative photoresponse mechanisms. One such mechanism is the optically-induced breakdown of quantum Hall effect (QHE) in a two-dimensional electron gas (2DEG)[6]. The sensitivity of QHE in GaAs 2DEG to radiation has been exploited to engineer ultrasensitive, tunable, frequency agile far-IR/THz photodetectors with nanosecond response time[6-9]. However, the wide use of GaAs QHE photodetectors is limited by the need of cooling detectors down to liquid helium temperatures, and no "classical" semiconductor-based QHE photodetectors operate above 12 K[9].

Here we demonstrate the successful operation of infrared QHE graphene-based detectors at 70 K, a temperature achievable using simple pumped liquid nitrogen cryostats, in magnetic field of 7.35 T. Due to graphene's unique band structure, the first few Landau levels are well-separated energetically, thus allowing observation and manipulation of QHE at unprecedentedly high temperatures[10]. Our results overcome the obstacle of low operating temperature in traditional semiconductor systems and open the door for wide arrays of applications.

VII-2. Experimental setup and magnetotransport measurement

The photodetectors in our experiments are two-pole nonsuspended monolayer graphene field effect transistor (FET) devices (see Fig. 7.1 inset). Mechanical cleavage-fabricated graphene flakes are deposited on 300 nm SiO_2/heavily doped *n*-Si substrates, allowing

optical identification of the flakes. Electrical contacts of 5 nm of Ti and 80 nm of Au are deposited using standard electron beam lithography. The magnetotransport and photoresponse characterization measurements are performed using a variable temperature insert (VTI) that allows measurements ranging from 1.6 to 300 K, with an American Magnetics 8 T superconducting magnet. Irradiation of samples is achieved using the chopper-modulated beam of a Synrad 48-2 CO_2 laser with wavelength $\lambda \sim 10.6$ μm, which is attenuated and delivered to samples via ZnSe beamsplitters and a copper hollow waveguide with IR-transparent KBr windows as a gasket. In transport measurements, we use Keithley 2000 and 2400 meters and source-meters. The photoresponse signal, *i.e.* the longitudinal voltage of the device in the QH regime, is amplified by Ametek /Signal Recovery model 5113 preamplifier, and then collected using Tektronix TDS380 oscilloscope.

Fig. 7.1 displays the two-terminal resistance R_{SD} of the device as a function of back gate voltage V_g at T=7 K and source-drain current I_{sd}=10 nA. The field effect mobility of the device is estimated to be ~15,000 cm^2/Vs, which is quite high for substrate-supported samples and is indicative of high sample purity. In magnetic fields, graphene's Dirac spectrum gives rise to Hall conductivity that is quantized at $(N+1/2)4e^2/h$, where N=...-1,0,1,2.. is an integer, e is electron charge and h Planck constant[11].

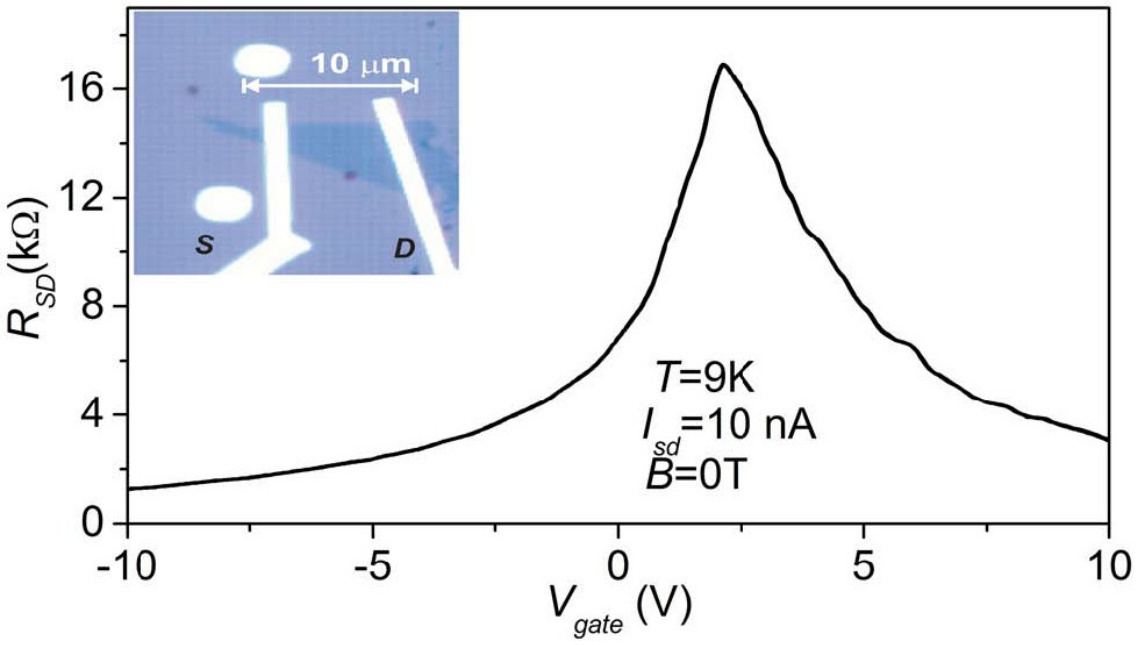

Fig. 7.1 Transport data and optical image of a monolayer graphene device: two-terminal transport data, showing source-drain resistance R_{SD} vs. gate voltage V_{gate}. The data are taken at source-drain current I_{sd}=10 nA and T=9 K. Inset: optical microscope photo of this device.

For a two-terminal device, its conductance is complicated by the mixture of longitudinal and transverse signals; nevertheless, for sufficiently narrow Landau levels, the two-terminal measurements yield properly quantized conductance[12]. Plateaus with filling factors ν=2 and ν=6 where ν=±4 (N+1/2), are observed (Fig. 7.2(a)) in our devices. Remarkably, the QH plateaus are observable at T=130 K and B=4.3 T, where the operating temperature is sufficiently high (above liquid Nitrogen) and the field strength sufficiently low that realistic applications are feasible. These plateaus are very robust, as they persist up to a source drain current I_{sd}~ 4 – 7 μA at temperatures T~ 5 – 10 K and magnetic field B~4 – 5 T (Fig. 7.2(b)).

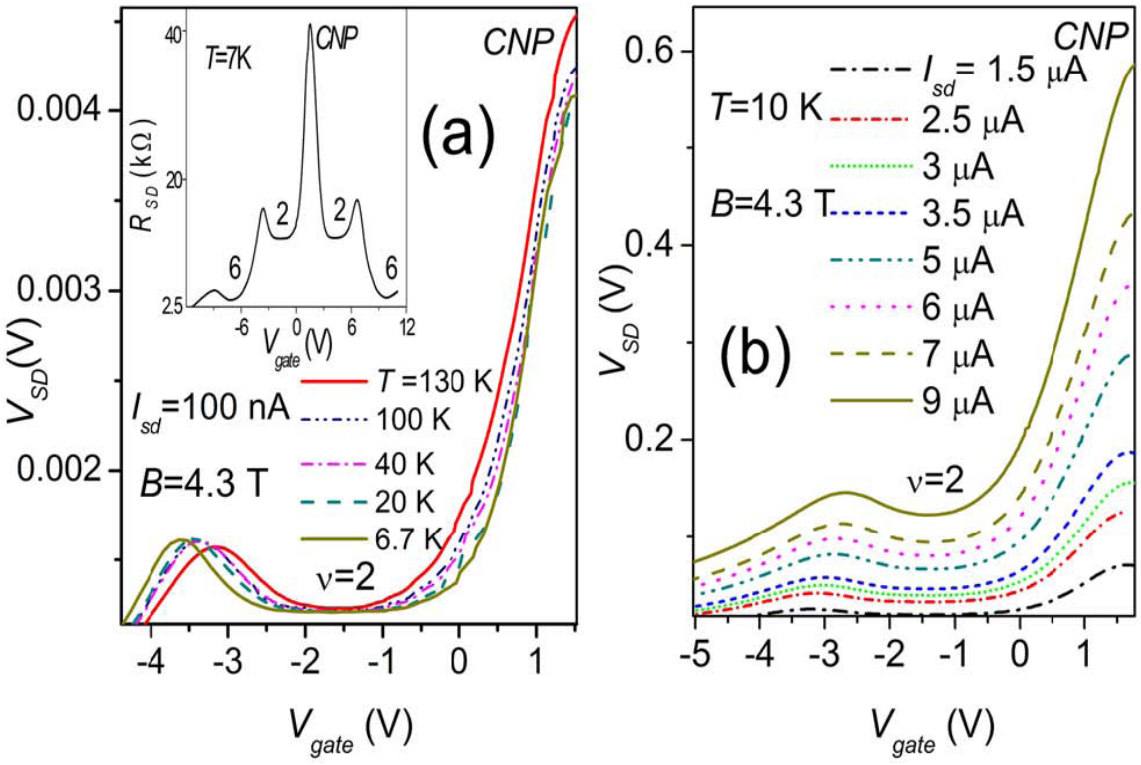

Fig. 7.2 QH probe characterization: (a) Source-drain resistance R_{SD} vs. gate voltage V_{gate} at different temperatures, showing the quantum Hall plateau at and near ν=2. The data are taken at I_{sd}=100 nA and B=4.3 T. Inset: $V_{SD}(V_{gate})$ for large V_{gate} ranges at T= 7K. (b) $V_{SD}(V_{gate})$ at different V_{gate} values. The data are taken at T=10 K, B=4.3 T. Here the QHE breaks down at I_{sd} ≈6.5 μA.

Encouraged by the robustness of the QHE, we perform photoresponse measurements of our graphene FET devices by registering the photoinduced change of source-drain voltage ΔV_{SD}. A schematic of the experimental setup is shown in Fig. 7.3.

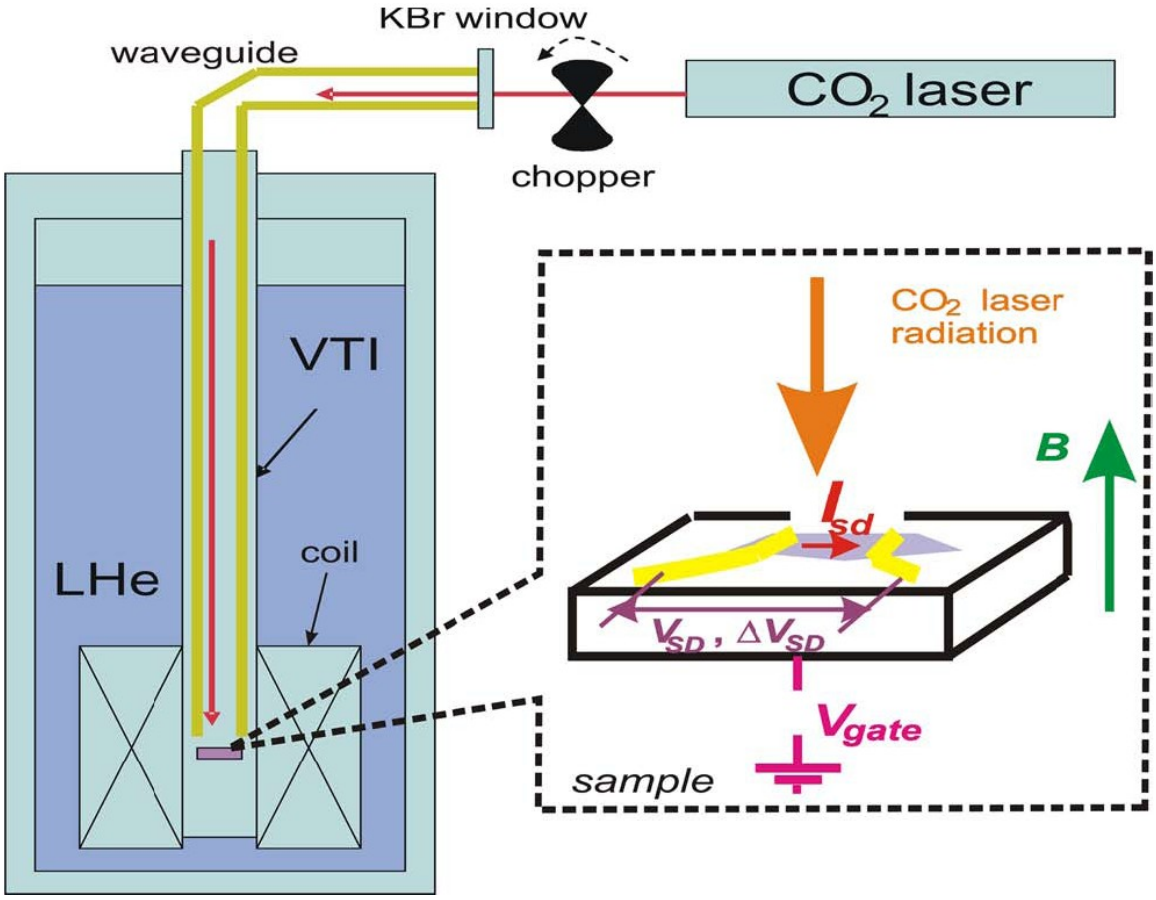

Fig. 7.3 Schematics of the photodetection experiment.

VII-3. Photoresponse measurement and data analysis

The results of photoresponse measurements for our monolayer graphene devices are demonstrated in Fig. 7.4 and 7.5. Fig. 7.4 shows the gate dependence of the photoresponse magnitude for one of our samples around ν=2 QHE plateau at T= 20 K, B= 7.35 T, I_{sd}= 3 μA (red curve), as well as $\Delta R_{SD}/\Delta T$ (purple curve), which is calculated by using $V_{SD}(T$=30 K)-$V_{SD}(T$=6 K))/(I_{sd}•(30 K-6 K)) at I_{sd}= 100 nA. For reference, the measured R_{SD} (V_g) between the Dirac point and the ν=2 plateau is shown as the blue

curve. Clearly, the photoresponse signal follows the same trend as gate dependence of $\Delta R_{SD}/\Delta T$, indicating that the operating mechanism of our graphene photodetectors is bolometric. The observed photoresponse exists at the flanks of QHE plateau, and may have different polarities depending on the sign of change of R_{SD} due to radiation-induced increase of detector temperature at given gate voltage. On the other hand, within the plateau the radiation heating in our experiment is not enough to break down QHE, thus yielding zero photoresponse (see Fig. 7.4). The purely bolometric behavior of photoresponse is not surprising: in magnetic fields below 7.5 T, we are away of cyclotron resonance position[13], which is located at ~8.41 T for the 10.6 μm line of CO_2 laser.

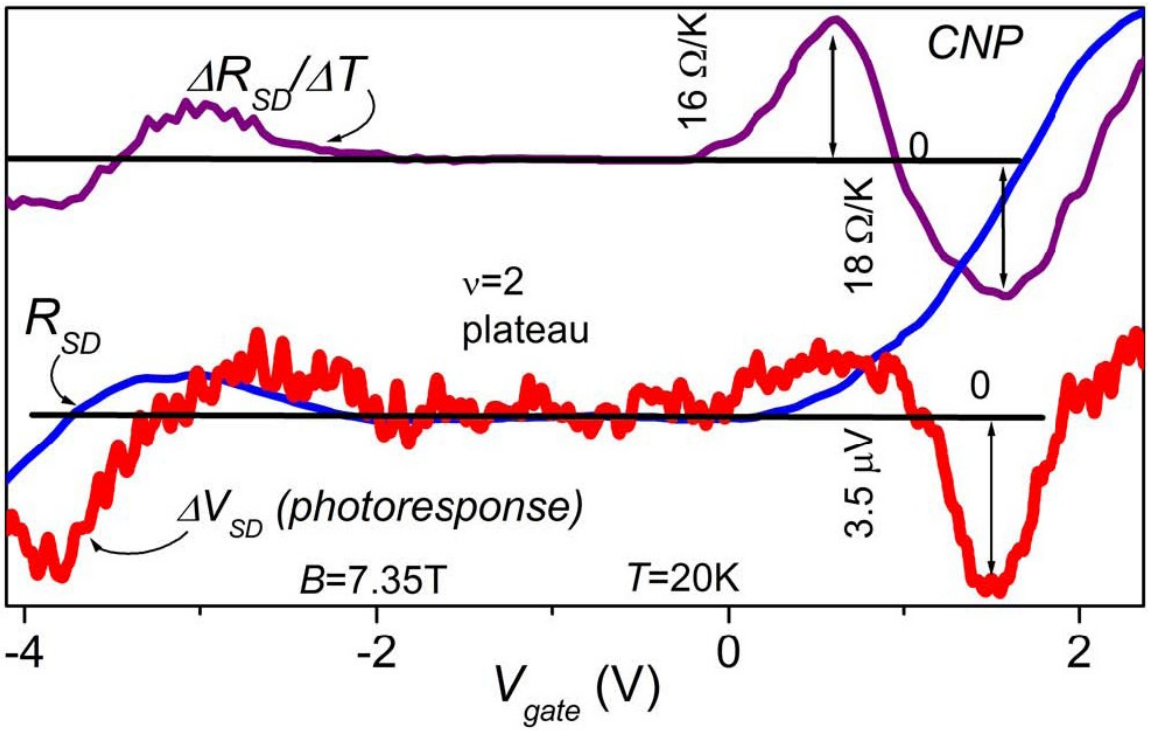

Fig. 7.4 Gate dependence of photoresponse and resistance. Bottom curve (red): ΔV_{SD} at T= 20 K, B= 7.35 T, I_{sd}= 3 μA. Modulated CW output, 40 mW, 200 Hz modulation frequency, AC

coupling of oscilloscope. Upper curve (purple): $\Delta R_{SD}/\Delta T = (V_{SD}(T=30\text{ K}) - V_{SD}(T=6\text{ K}))/(I_{sd} \bullet (30\text{ K} - 6\text{ K}))$ at $I_{sd} = 100$ nA. Gate dependence of R_{SD} is shown for reference (blue curve).

Fig. 7.5(a) shows the temporal behavior of photoresponse of one of our QHE devices at B=7.35 T, I_{sd}=3 μA and T=4.77 K. We apply gate voltage that corresponds to the edge of ν=2 quantum Hall plateau, as marked by the red arrow in Fig. 7.5(a), and measure the photoinduced change of the two-terminal voltage. The inset of Fig. 7.5(a) shows the temporal trace of the photoresponse (after 10^4 times amplification) to the chopper-modulated CO_2 laser excitation with 40 mW power. One can clearly see the oscillations of photoinduced voltage (red curve) correlating with the reference signal from the chopper optoelectronic control circuit (green curve), and the absence of photoinduced voltage change when laser radiation was blocked (blue curve).

The observed photoresponse is rather slow, with a visible ~1 ms delay between moments of on/off switching of laser radiation and corresponding changes of V_{SD}. The magnitude of the response decays rapidly with increase of chopper modulation frequency in the region above 300-400 Hz. The slow ~ms response time of our device is also typical for bolometric detectors, whose response speed is determined by many thermodynamical factors such as heat conductance, heat capacitances, and geometrical parameters of detector parts[14]. Finally, the bolometric photoresponse regime of QHE-based detectors is well-known for "classical" 2DEGs[6-8] and may also be important in interpreting data from previous CR experiments in graphene[13,15,16].

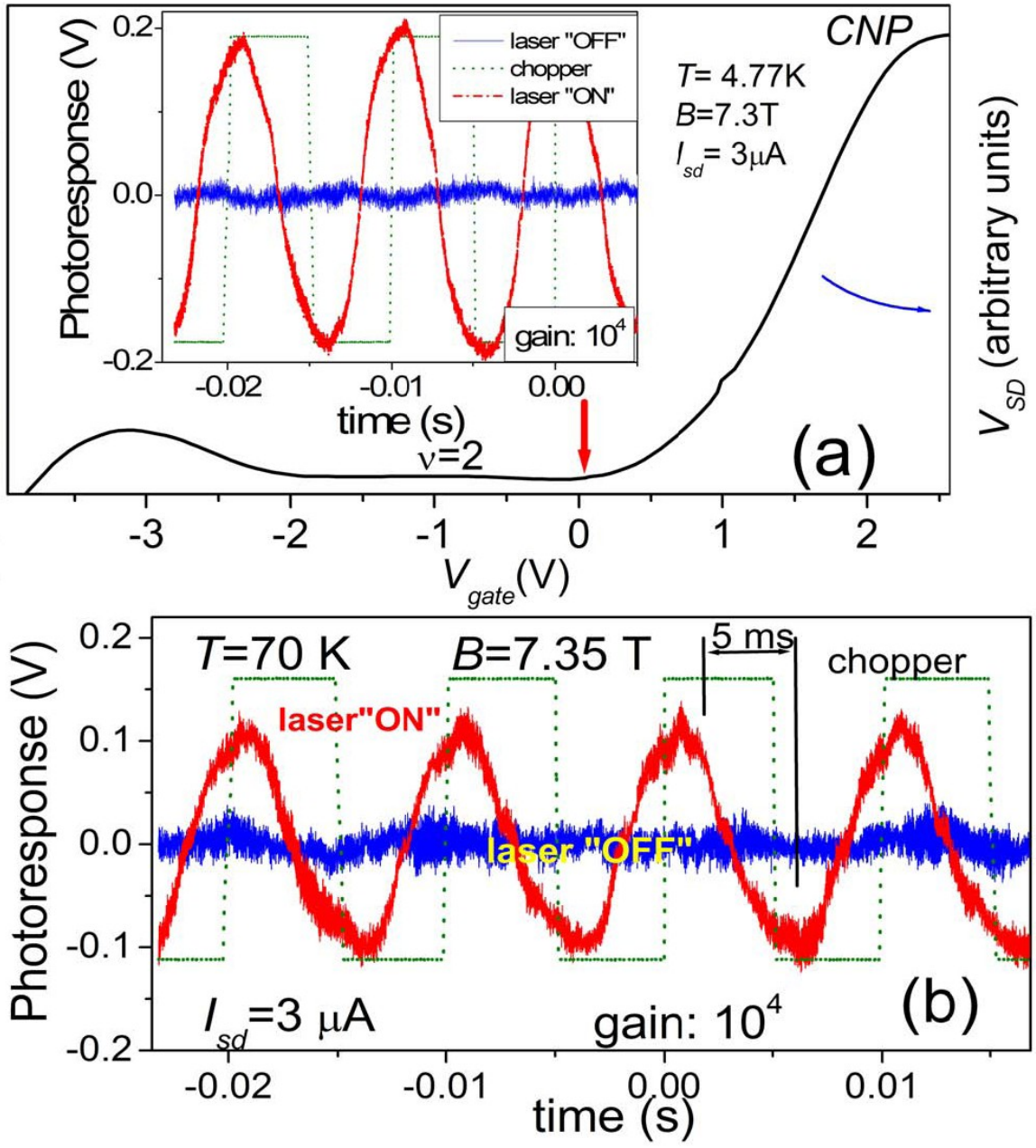

Fig. 7.5 Graphene detector's photoresponse at different temperatures. (a) The data are taken at V_g=0 V, as indicated by the arrow in the main panel, and B=7.35 T, I_{sd}=3 μA, using choppermodulated CO_2 laser excitation with 40 mW power. AC coupling of oscilloscope. Inset: photoresponse (ΔV_{SD}) after 10^4-times amplification at T=4.77 K. (b) ΔV_{SD} at T=70 K.

We repeat the same measurement at T=70 K. The photoresponse for the laser-irradiated (red curve) and "dark" (blue curve) device are shown in Fig. 7.5(b). At this elevated temperature, the QHE plateaus persist, though with reduced width. The magnitude of the photoresponse is significantly reduced comparing to that for 4.77 K, but is still clearly visible, with a response time on the order of several milliseconds. We note that this is the first demonstration of QHE photodetectors at such high temperatures, which can be achieved using a pumped liquid Nitrogen dewar.

We now discuss the sensitivity of the graphene QHE detector. Typically, we have several μV-amplitude of photoresponse for mille-watts in applied power, which is mostly absorbed by the SiO_2/Si substrate. The resulting responsivity of detection we achieve is of the order of ~10^{-2}-10^{-3} V/W. The noise in our photoresponse measurements is ~ 0.5 μV, which is attributed to the two-terminal device geometry that mixes in the large R_{xy}-component of resistance into the noise voltage. Therefore, the noise level can be dramatically reduced if devices with Hall bar geometries are employed.

Further improvement in graphene-based QHE photodetectors can be achieved by operating in the resonant regime of detection, instead of the bolometric regime[13]. For Far-IR and microwave applications, using of antenna systems or other radiation coupling/enhancing solutions will boost sensitivity by orders of magnitude.

References:

1) A.K. Geim, K.S. Novoselov, *Nature Materials* **6**, 183 (2007)

2) F. Bonaccorso, Z. Sun, T. Hasan, A.C. Ferrari, *Nature Photonics* **4**, 611 (2010)

3) K. F. Mak, C. H. Lui, J. Shan, and T. F. Heinz, *Phys. Rev. Lett.* **102**, 256405 (2009)

4) F. Xia, T. Mueller, Y. Lin, A. Valdes-Garcia, P. Avouris, *Nature Nanotech.* **4**, 839 (2009)

5) T.Mueller, F.Xia, P.Avouris, *Nature Photonics* **4**, 297 (2010)

6) Y. Kawano, Y. Hisanaga, H. Takenouchi, S. Komiyama, *Journ. Appl. Phys.* **89**, 4037 (2001)

7) N.G. Kalugin, Yu.B. Vasilyev, S.D. Suchalkin, G. Nachtwei, B.E. Sagol, K. Eberl, *Phys. Rev. B* **66**, 085308 (2002)

8) G. Nachtwei, F. Gouider, C. Stellmach, G. Vasile, Yu.B. Vasilyev, G. Hein, R. R. Gerhardts, *Phys. Rev. B* **78**, 174305 (2008)

9) J.-C. Chen, J. Zhang, C.C Chi, T. Ueda, S. Komiyama, *Jpn. J. Appl. Phys.* **49**, 031201 (2010)

10) K. S. Novoselov, Z. Jiang, Y. Zhang, S. V. Morozov, H. L. Stormer, U. Zeitler, J. C. Maan, G. S. Boebinger, P. Kim, A. K. Geim, *Science* **315**, 1379 (2007)

11) Y. Zhang, Y. W. Tan, H. L. Stormer, P. Kim, *Nature* **438**, 201 (2005)

12) D. A. Abanin, L. S. Levitov, *Phys. Rev. B* **78**, 035416 (2008)

13) R. S. Deacon, K. C. Chuang, R. J. Nicholas, K. S. Novoselov, A. K. Geim, *Phys. Rev. B* **76**, 081406(R) (2007)

14) P. L. Richards, *J. Appl. Phys.* **7**, 1 (1994)

15) Z. Jiang, E. A. Henriksen, L. C. Tung, Y. J. Wang, M. E. Schwartz, M. Y. Han, P. Kim, H. L. Stormer, *Phys. Rev. Lett.* **98**, 197403 (2007)

16) M. Sadowski, G. Martinez, M. Potemski, C. Berger, W. A. de Heer, *Phys. Rev. Lett.* **97**, 266405 (2006).

Chapter VIII. Conclusions

In this thesis, I present our studies on the electrical and mechanical properties of two different van der Waals materials: graphene and $Ca_xBi_{2-x}Se_3$ (x is the doping level), a member in the 3D TIs family. In the transport study of bilayer graphene *pnp* junctions, we observe a band gap opening with external electric field with an on/off ratio of 20,000, an insulating state induced by applied magnetic fields and equilibrated edge states between regions with different filling factors. It was the first report of the edge state equilibration in the bilayer graphene *pnp* junction and the highest on/off ratio at the time[1]. For our future direction, the recent advance in fabrication of suspended graphene[2] with dual-gates would enable us to investigate more many-body physics in graphene system, such as long range interactions between electrons.

Furthermore, we investigate electronic transport of $Ca_xBi_{2-x}Se_3$ thin films coupled with superconducting electrodes. We characterize the doping level and phonon modes by energy-dispersive x-ray spectroscopy (EDS) and Raman spectroscopy, respectively. Four-probe electrical measurements reveal ~5 nA critical current in these novel Josephson transistors. To explore more physics and potential applications towards topologically protected quantum computing, it would be necessary to apply multi-level lithography process[3] to fabricate suspended TIs devices.

We also measure the thermal expansion of suspended graphene via *in-situ* scanning electron microscope. In contrast to the prediction that thermal expansion coefficient (TEC) of few layer graphite monotonically increases with its thickness, we observe what appears to be a non-monotonic correlation between the 2 parameters: TEC firstly decreases with increasing thickness up to ~10 nm, then increases again. One hypothesis for this surprising observation, somewhat substantiated by devices with electrodes that partially clamps the thin films, is that the friction between the substrate and the graphene decreases with increasing thickness and competes with the intrinsic TEC, resulting in this non-monotonic behavior. To completely understand our observations, fully-clamped devices are necessary. Similar measurements can also be extended to other 2D materials, such as MoS_2[4].

Finally, we collaborate with Dr. Nikolai Kalugin from New Mexico Tech. on the graphene-based QHE infrared photodetector. The detected photoresponse is bolometric and this novel detector can be operated at liquid nitrogen temperature, which is significantly higher than the traditional 2DEGs-based quantum Hall detectors[5-7]. We have made progress in the fabrication of suspended graphene photodetectors coupling with antenna-wings. We expect that the sensitivity and photoresponse can be significantly improved by coupling antenna system and high quality of suspended graphene devices.

References:

1) L. Jing, J. Velasco Jr., P. Kratz, G. Liu, W. Bao, Marc Bockrath, C. N. Lau, *Nano Letters* **10**, 4000 (2010)

2) J. Velasco Jr., L. Jing, W. Bao, Y. Lee, V. Aji, M. Bockrath, C.N. Lau, C. Varma, R. Stillwell , D. Smirnov, Fan Zhang, A. MacDonald, *Nature Nanotechnology* **7**, 156 (2012).

3) J. Velasco Jr. , Z. Zhao, H. Zhang, F. Wang, Z. Wang, P. Kratz, L. Jing, W. Bao, J. Shi and C.N. Lau, *Nanotechnology* **22**, 285305 (2011)

4) B. Radisavljevic, A. Radenovic, J. Brivio, V. Giacometti, A. Kis, A. *Nature Nanotechnology* **6**, 147 (2011)

5) Y. Kawano, Y. Hisanaga, H. Takenouchi, S. Komiyama, *Journ. Appl. Phys.* **89**, 4037 (2001)

6) N.G. Kalugin, Yu.B. Vasilyev, S.D. Suchalkin, G. Nachtwei, B.E. Sagol, K. Eberl, *Phys. Rev. B* **66**, 085308 (2002)

7) G. Nachtwei, F. Gouider, C. Stellmach, G. Vasile, Yu.B. Vasilyev, G. Hein, R. R. Gerhardts, *Phys. Rev. B* **78**, 174305 (2008)

Appendix：Plasma Etching Parameters

Table Appendix.1 Reactive Ion Etch (RIE) parameters

Etching material	SiO_2	Graphene
Etchant	CHF_3/O_2	O_2
Gas flow (sccm)	50/1.9	50
Pressure (mTorr)	5	5
Power (W)	200	15
Etch rate	0.5~1.5 nm/second	5~15 second/layer

Table Appendix.2 Inductively Coupled Plasma (ICP) parameters

Etching material	Silicon	PMMA
Etchant	SF_6/C_4F_8	H_2
Gas flow (sccm)	70/50	50
Pressure (mTorr)	5	5
Plasma Excitation Power (W)	50/20	50
Forward Bias Power (W)	450/400	0
Etch rate	0.2~0.7 μm/cycle	15~30 nm/second